UNIVERSITÀ DI MILANO-BICOCCA

PH.D. SCHOOL IN NANOSTRUCTURES AND NANOTECHNOLOGIES

Nanostructured III-V epilayers on silicon substrate for optoelectronic applications

---

Author:
Sergio BIETTI

Tutor:
Prof. Stefano SANGUINETTI

Dean of the Ph.D. school:
Prof. Leo MIGLIO

Academic Years 2008-2010

La filosofia è scritta in questo grandissimo libro che continuamente ci sta aperto innanzi a gli occhi (io dico l’universo), ma non si può intendere se prima non s’impara a intender la lingua, e conoscer i caratteri, ne’ quali è scritto. Egli è scritto in lingua matematica, e i caratteri son triangoli, cerchi, ed altre figure geometriche, senza i quali mezi è impossibile a intenderne umanamente parola; senza questi è un aggirarsi vanamente per un oscuro laberinto.

Il Saggiatore, G. Galilei

Contents

Introduction

Gallium Arsenide and Silicon are the most widely used materials in modern device fabrication for electronics. Nowadays about 95% of electronic devices are fabricated by silicon. Silicon is the second most abundant element on Earth surface and it's easy to collect, is robust, allows the fabrication of large diameter wafer, has a good thermal conductivity, gives the possibility to integrate silicon dioxide as insulator and has a high mobility for the holes. These properties made possible the development of the Complementary Metal-Oxide-Semiconductor (CMOS) technology and allow the integration on a single chip of billion components. This technology is the base for the fabrication of microprocessors, micro-controllers, memories, image sensors and data converters.

On the other hand, for optoelectronic applications the presence of an indirect gap makes silicon less effective than direct gap material for the fabrication of detector and especially for the fabrication of light emitting and detecting devices. For this reason III/V compounds like GaAs are widely used in optoelectronics. Also for the fabrication of solar cells and for high mobility devices direct gap materials have better performances than silicon.

The possibility to integrate devices for applications in optoelectronics and photonics based on III-V semiconductors, directly on Si substrates would allow the use of the highly refined silicon infrastructure, based on CMOS technology, to be maintained and would offer the option of integrating a few specialized III-V devices within a large number of Si devices.

In this work of thesis we will investigate the possibility to integrate III-V quantum nanostructures directly on Silicon substrate, to combine the advantages of both materials. The growth of semiconductor materials inside a Molecular Beam Epitaxy machine is outlined in the first chapter. The second chapter explain the Droplet Epitaxy technique for the fabrication of GaAs quantum nanostructures highly tunable in density, size and shape using a low thermal budget compatible with CMOS technology. The third chapter is dedicated to introduce the epitaxy of GaAs on Si substrate with the related issues. In the fourth chapter the experimental setup used in this work of thesis for the sample growth and characterization is described. The fifth and the sixth chapter describe the experiments performed and the results obtained in GaAs growth on Si through a Ge layer (chapter 5) and as a local artificial substrate (chapter 6).

Chapter 1

Molecular Beam Epitaxy

The term epitaxy comes from the Greek $\epsilon\pi\iota$, meaning "above", and $\tau\alpha\xi\iota\varsigma$, meaning "in ordered manner". Molecular Beam Epitaxy (MBE), is a technique for the growth of extremely high quality epitaxial thin layers on a substrate. MBE technique allows to control to within a single atomic layer thickness and composition of films. MBE is based on beams of evaporated atoms directed to a single crystal substrate in an ultra-high vacuum environment (generally considered to be vacuum levels below 10^{-9} torr). Under suitable conditions of flux and substrate temperature, high-quality epitaxial layers are grown in a highly reproducible manner. In this chapter an overview of the nucleation and growth processes occurring in thin film formation inside a Molecular Beam Epitaxy (MBE) chamber will be outlined.

1.1 Some history

Before the development of molecular beam epitaxy, there were many attempts to grow compound semiconductors in vacuum. For III-V compounds, Gunther [1] proposed the use of a "three temperature" method where the substrate, Group III and Group V sources had different temperatures to independently control their vapour pressures. Later Davey and Pankey [2] deposited epitaxial GaAs on single crystalline GaAs substrates but the resulting films showed poor crystalline quality. In the late 1960s, as devices were getting smaller, there was a great demand for a crystal growth technology that could prepare single crystalline films as thin as 500-1000 Å. The term molecular beam epitaxy was used for the first time in 1970 [3] after several years of extensive studies of atomic and molecular beams interacting with solid surfaces [4, 5]. A great work for understanding surface physics was carried out by Arthur, Cho, Foxon, Harvey and Joyce on measurements of the adsorption lifetime, sticking coefficient and reaction order, studying the interaction of Ga and As beams on GaAs surfaces. As-stabilized and Ga-stabilized surface reconstructions were investigated by observing high energy electron diffraction (HEED). At that time cells were quartz ampules heated by tungsten wire connected to a variac and with a pinhole aperture of less than 1 mm in diameter. Deposition rate with this configuration was limited to less than 1 monolayer per minute. For this reason the effusion cells were changed to large aperture graphite and alumina construction with heat shielding consisting of layers of corrugated tantalum foil to reduce the heat loss and temperature cross talk with adjacent cells. All cells were surrounded with a liquid nitrogen cooled shroud to reduce the background pressure. The cell temperatures were also regulated by electronic feedback

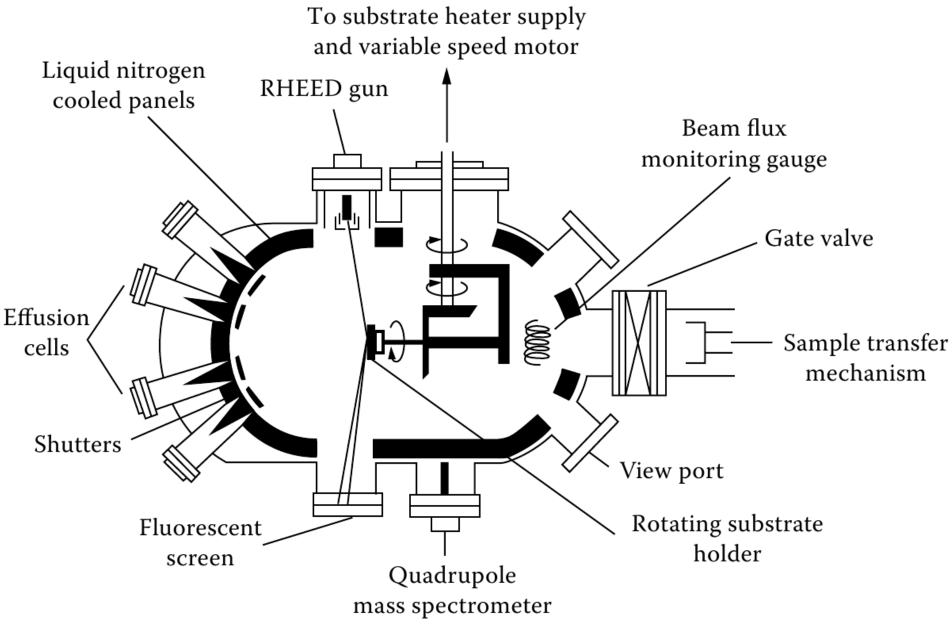

Figure 1.1: a typical setup for a molecular beam epitaxy machine

systems to assure precise effusion fluxes. An arsenic cracker cell was first used in 1971 for the effusion of As to improve the control on As flux and to improve the photoluminescence efficiency [6]. High energy electron diffraction (HEED) became a routine real-time monitoring tool for the initial cleaning and successive growth of epitaxial films. After these improvements was possible to grow high-quality GaAs layers.

1.2 Modern MBE systems

Of the many available epitaxial growth techniques, MBE has emerged as the most flexible tool for heteroepitaxial research on III-V and II-VI semiconductors. This is mainly due to the ability to deposit thin layers and complex multilayered structures with precise control and excellent uniformity. MBE is an ultra-high-vacuum (UHV) technique that involves the impingement of atomic or molecular beams onto a heated single-crystal substrate. The source beams originate from Knudsen evaporation cells or gas-source crackers. These cells can be turned on and off abruptly by shutters and valves, providing atomic layer control. Because MBE takes place in a UHV environment, it is possible to employ a number of in situ characterization tools based on electron or ion beams. These tools provide an immediate feedback to the grower and an improved control over the growth process. As shown in figure 1.1 an MBE reactor involves a number of cells with different source materials in front of a heated substrate holder. The source cells supply all atoms necessary for the growth of a semiconductor layers. The simplest type of source cell is a thermal evaporator (a Knudsen cell). A basic requirement for MBE growth is that the evaporated atoms must have mean free paths greater than the distance between the source and the substrate, which is typically 5-30 cm. This requirement places an upper limit on the operating pressure for an MBE reactor. If it is assumed that an evaporated particle at temperature T has a cross section with diameter σ in an environment with pressure P, the mean free path may be estimated by the formula

$$l = \frac{kT}{\sqrt{2}\pi\sigma^2 P} \tag{1.1}$$

Typical values of the cross section diameter σ are 2-5 Å, so that the mean free path is few meters at a pressure of 10^{-5} torr. This pressure therefore represents an approximate upper limit for the system pressure during growth, if the beam nature of the sources is to be maintained.

In order to obtain high purity films the base pressure should be no more than $10^{-9} - 10^{-10}$ torr. An indicative formula for the impinging rate of molecules hitting a surface of 1 cm^2 in 1 second is

$$J = \frac{p}{\sqrt{2}\pi mkT} \tag{1.2}$$

where p is the pressure, m the mass of the impinging molecules and T the temperature. To understand the importance of having a ultra-high vacuum level in the chamber we can calculate that at room temperature a pressure of 10^{-6} Torr results in an impinging rate of 10^{14} molecules per second per square centimeter. Considering that on a GaAs surface there are about 6×10^{14} atoms cm^{-2}, this means that in few seconds the surface will be covered with atoms and molecules of unknown species. Achievement of a vacuum level of$10^{-9} - 10^{-10}$ torr requires the use of a stainless steel chamber with metal gaskets and the use of oil-free pumping (like cryogenic, titanium sublimation, ion and turbomolecular pumps). It is also required the presence of an introduction chamber to load the substrates and to collect the samples after the growth to break the vacuum in the main growth chamber only for maintenance. Any exposure of the chamber to air must be followed by a long bake-out to remove adsorbed contaminants. In order to further reduce evaporation from internal surface area, during growth the chamber walls should be cooled to cryogenic temperatures by means of liquid nitrogen shrouds.

The most used source cells are thermal evaporators, called effusion or Knudsen cells. One cell with high-purity elemental material for each element is needed. The effusion cells are typically made of pyrolytic boron nitride (PBN) with tantalum heat shields. The source temperatures are maintained precisely to control the flux of evaporating atoms. A shutter for each cell is provided to turn each beam on and off due to the inability to rapidly ramp up or down the cell temperature. Using the kinetic theory of gases it is possible to calculate that the evaporation rate from a surface area A_{eff} is given by

$$\frac{dN_{eff}}{dt} = \frac{A_{eff}P}{\sqrt{2\pi kTM/N_A}} \tag{1.3}$$

where P is the vapour pressure for the source material of molecular weight M at temperature T. Because the equilibrium vapour pressure varies exponentially with temperature (see figure 1.2), the effusion cell temperature must be controlled accurately in order to keep the error on effusion rate within a 1% tolerance. The flux arriving at the substrate surface can be calculated from the evaporation rate at the effusion cell with the cosine law

$$j = \frac{\cos\theta}{\pi d^2}\frac{dN_{eff}}{dt} \tag{1.4}$$

where d is the distance from the effusion cell to the substrate and θ is the angle between the beam axis and the normal to the substrate. In fact a real effusion cell depletes with

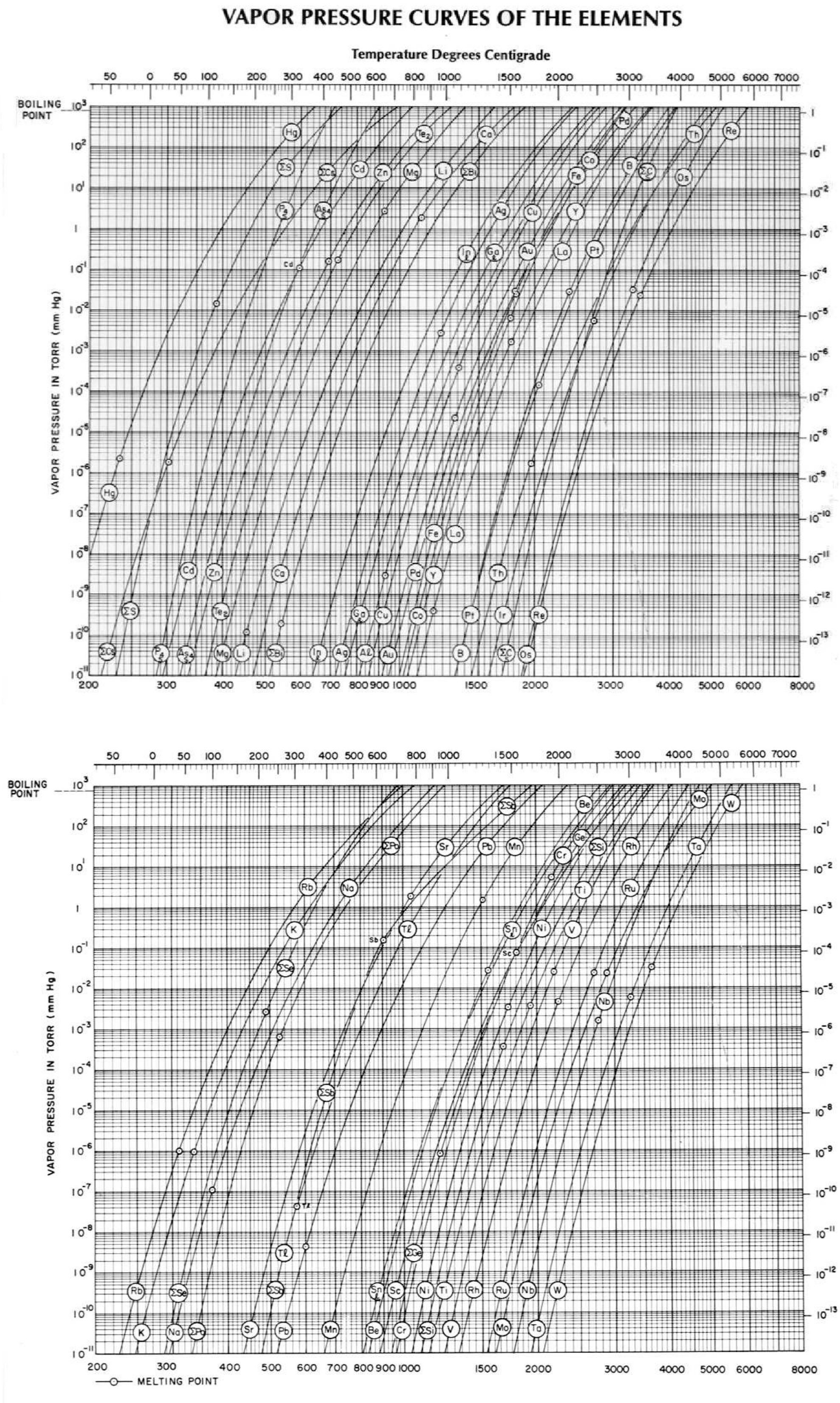

Figure 1.2: vapour pressures of the elements.

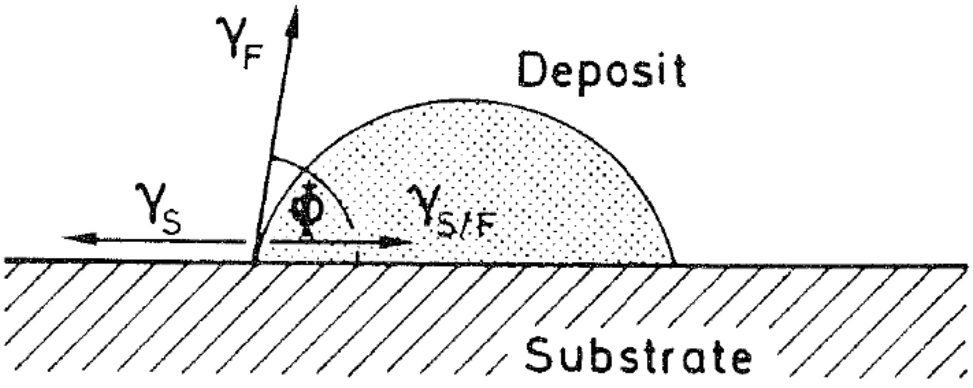

Figure 1.3: balance of surface free energy for a island deposited on a substrate. From ref. [7]

time, and this causes a fall-off of the impingement rate and a change in the beam profile at the substrate. Usually the evaporation crucibles have a 1 cm^2 evaporation surface and are located 5 to 30 cm from the substrate. Typical source pressures are 10^{-3} to 10^{-2} torr, resulting in the delivery of 10^{15} to 10^{16} molecules cm^{-2} s^{-1}. This corresponds to a growth rate of about one monolayer per second, assuming a unity sticking coefficient for the impinging atoms.

1.3 Nucleation on surfaces

Vapour deposition of thin films is a simple case of crystal growth, since it involves the formation of a dense, solid phase from a dilute, gaseous phase. The theoretical formulations are quite simple: thermodynamic and statistical mechanical models can be formulated and tested by experiment. But, in fact, real behaviour is typically more complicated than these simple models.

In the most simplified view, is possible to describe three modes for the crystal growth (layer by layer, island and layer plus island) of material A on a substrate B by using surface tension. The model was originally proposed by Bauer in 1958. In this description the surface tension γ can be interpreted as a force per unit length of boundary, so that force equilibrium at a point where substrate and deposited material touch can be expressed as $\gamma_S = \gamma_{SF} + \gamma_F \cos\phi$ where γ_S is the surface free energy of the substrate-vacuum interface,γ_F that of the film-vacuum interface and γ_{SF} that of surface-film interface (see figure 1.3). When $\phi = 0$ and $\gamma_S \geq \gamma_{SF} + \gamma_F$ the growth proceed layer-by-layer (Frank-van der Merve, or FM), when $\phi > 0$ and $\gamma_S < \gamma_{SF} + \gamma_F$ islands grow leaving part of the substrate exposed (Volmer-Weber, or VW). If a lattice mismatch is present between the substrate and the film it's also possible to have an initial layer-by-layer growth followed by island growth after few monolayers (Stranski-Krastanov, or SK) [7]. The above classification assumes that no interdiffusion or chemical reactions between the atoms of the subtrate and of epilayer take place.

Getting deeper into details, it is necessary to consider the atomic processes responsible for nucleation and growth of thin films. The real fabrication of thin films usually

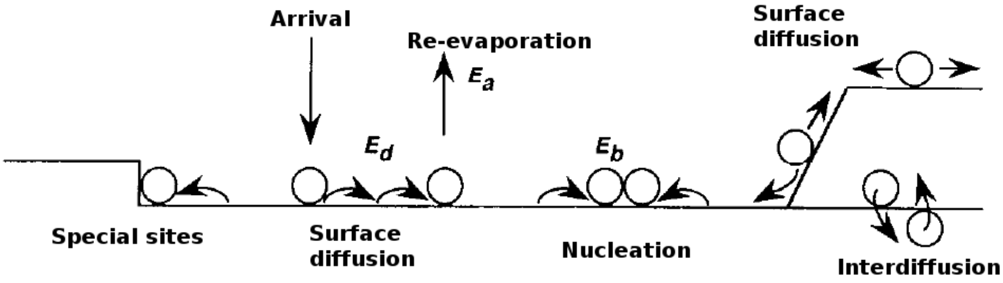

Figure 1.4: typical atomistic processes during epitaxial growth

proceeds through different stages involving adsorption, surface diffusion, binding and re-evaporation.To describe these phenomena different models were developed, stochastic or deterministic, using atomistic or macroscopic variables.

For example, a more detailed description is given in molecular dynamic simulations, where the forces applied to every single atom are considered. A simplification is introduced considering the rates associated with microscopic events such as adatom diffusion and re-evaporation. In the transition state theory [8] rates are expressed with the equation

$$\tau^{-1} = \nu_0 e^{\frac{-\Delta E}{kT}} \tag{1.5}$$

where ΔE is the activation energy barrier, ν_0 is typically of the order of the atomic vibration frequency (10^{-12} – 10^{-13} s^{-1}) and T is the temperature. We can consider the surface processes shown in figure 1.4. Atoms arrive from vapour at a rate R, creating adatoms whose density n_1 is initially described by $n_1 = Rt$. The re-evaporation rate of the adatoms from the surface is described by the equation $\tau_a^{-1} = \nu_a(-E_a/kT)$ where ν_a is an atomic vibration order of 1-10 THz. A simple equation for the diffusion on the surface is $D = (\nu_d a^2/4)exp(-E_d/kT)$ where a is the distance on the surface between sites (0.2-0.5 nm) and ν_d is typically somewhat less than ν_a. The number of substrate sites visited by an adatom in time τ_a is $D\tau_a/N_0$ where N_0 is the areal density of surface sites (the same order as a^{-2}). The mean path of adatoms from the arrival site before evaporation is $x = \sqrt{(D\tau_a)}$ so that it is possible to estimete the diffusion length with $x \simeq a(\nu_d/\nu_a)^{1/2}exp\left[(E_a - E_d)/2kT\right]$. Because E_a is usually greater than E_d, at low substrate temperature the diffusion length can be large, so that during their migration the adatoms will encounter other atoms. Depending on their binding energy E_b and their density, these atoms will form small clusters that eventually will become stable if the size will exceed a critical number of atoms i. The migrating adatoms can encounter special sites, surface and interdiffusion processes may occur. These processes are more difficult to model in detail, because they are highly specific to the system studied.

The processes considered in figure 1.4 can be visualized from an atomistic point of view as follows: atoms arrive from the vapour on the surface, here they may evaporate, or may alternatively start the nucleation of small clusters. The nucleation of some stable clusters opens another channel for the loss of adatoms, i.e. capture by stable clusters. When these clusters cover a fraction Z of the substrate, the direct impingement of clusters from the vapour became possible. These processes can be described by the rate equations

$$\frac{dn_1}{dt} = R(1 - Z) - \frac{n_1}{\tau_a} - \frac{n_1}{\tau_n} - \frac{n_1}{\tau_c} \tag{1.6}$$

where n_j is the density of clusters with j atoms (j=1 means adatoms), τ_a is the residence time of an atom on the surface before re-evaporation, τ_n is the mean time before the adatom nucleates a new cluster meeting another adatom and τ_c the mean time before being captured by a cluster. The equation can also by written as $dn_1/dt = R\tau(1 - Z)$ where $\tau^{-1} = \tau_a^{-1} + \tau_n^{-1} + \tau_c^{-1} + ...$ in which every other competing mechanism add a new channel. The sticking of adatoms to stable clusters can be approximated by $\tau_c^{-1} = \sigma_x D n_x$ where n_x is the density of clusters of any size, D is the diffusion coefficient already discussed and σ_x the capture rate of diffusing adatoms by clusters of any size. Steps and point defects, which can act as traps for diffusing adatoms, must be considered to describe a real surface. It is possible to formulate the step capture problem and to describe the competition between nucleation on the terraces and incorporation at steps by a term $\tau_s^{-1} = 12D/d^2$ where d is the step separation. The so called step-flow growth is thus possible when $\tau_s < \tau_c$ which means that adatoms can nucleate only on the steps. In the discussion we have assumed that clusters with size j>i are stable and that the initial nucleation events on large terraces occurred at random positions. We have also to consider that the film as deposited is often far from equilibrium. For example in the island growth mode the equilibrium state is reached when all the deposited material is in one large island. The driving force to approach this equilibrium is the reduction in surface energy. Thus, for example, coalescence of two islands typically results in one island which re-organizes its shape in attempt to minimize its surface energy.
Several real growth conditions are nicely approximated by the theory outlined. One example is the layer by layer in homo-epitaxy of Si(100). On a surface which is tilted off-axis by about $2-4°$ step-flow growth is promoted, and suppress random nucleation on terraces decreasing the possibility of incorporating defects. In the real Si(100) we have to consider also the (2×1) surface reconstruction, which arises to reduce the density of dangling bonds on the surface, as we will see in chapter 3. This reconstruction reduces the symmetry of the surface, results in diffusion and growth properties which are very anisotropic, and alternate dimers directions across single height steps. On Si(100) surface steps can be single or double height which results in different step energies. For this reason nucleation and growth are intrinsically quite complicated. Only introducing some simplification we can say that the dimer reconstruction has to be broken and reformed for the growth of each layer.

1.4 Equilibrium crystal shape

According to the Wulff construction rule, the final crystal shape is determined through the minimization of total surface free energy at a given volume [9]. Once the surface free energy of each orientation of constituent material is known, then the equilibrium crystal shape of a crystal can be built up by the Wulff construction. The distance of a particular facet having surface free energy per unit area of γ from the center of symmetry is proportional to r determined by

$$r(\mathbf{n}) = \min_{\mathbf{m}} \left[\frac{\gamma(\mathbf{n})}{\mathbf{m} \cdot \mathbf{n}} \right] \tag{1.7}$$

where **m** is a unit vector normal to the given orientation and **n** is a normalized vector directing from the center of symmetry (Wulff point) to any point on a given facet surface. With the constraint of a fixed volume of a crystal, this means that r of each facet for $\max[\mathbf{m}\cdot$

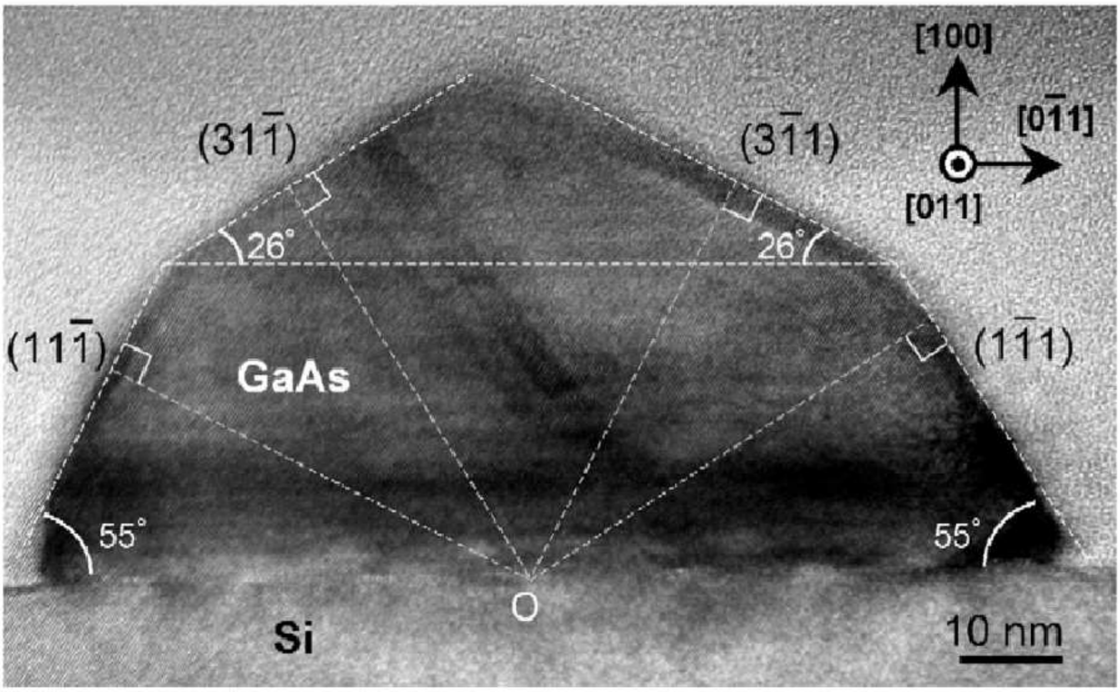

Figure 1.5: cross-sectional image of GaAs grown on Si substrate with the Wulff construction. From [13].

n] is proportional to γ. In other words in the Wulff's theory the ratio of the surface energy of facets to the distance between the Wulff point and the facets is constant when a crystal forms equilibrium crystal shape in order to minimize the total surface energy of the crystal. The exact values of surface energies for different surface planes remain difficult to obtain but in a first approximation is possible to say that the surface energy of a crystal plane with Miller indices hkl is proportional to the number of dangling bonds produced in forming that surface, but γ changes e.g. with growth conditions, deposited material, presence of strain. Studies of equilibrium crystal shape were performed on different systems, such as Ge on Si and GaAs (e.g. [10, 11, 12]). For the nucleation of Ge island on Si(001) substrate the set of $\{111\}$, $\{113\}$, $\{105\}$ and $\{15\ 3\ 23\}$ facets were found to be stable. For GaAs(001) the set of stable surface is $\{111\}$ and $\{110\}$, but experimentally evidence of $\{113\}$, $\{115\}$, $\{105\}$ and $\{103\}$ stable facets is reported [12]. Figure 1.5 shows a cross section image of a GaAs island grown on Si substrate. The nanocrystal has a structure consisting of $\{111\}$ and $\{311\}$ facet planes. The intersectional point O (Wulff point) was determined by drawing perpendicular lines to the facets. The value of γ for each facet is proportional to the distance between the centre of symmetry O and the facet.

1.5 Reflection high energy electron diffraction

The use of reflection high energy electron diffraction inside the main chamber during the deposition allows to monitor the growth process in real-time and to obtain important informations about the surface morphology of the sample. An electron gun generates a beam of electrons (typically between 4-50 keV) which strikes the sample at a very small angle relative to the sample surface (few degrees). Due to the dimension of the beam on the sample, the RHEED informations are averaged over a macroscopic area. Incident electrons are diffracted by atoms at the surface of the sample and interfere constructively at specific angles to form regular patterns on a fluorescent screen. To understand the essential features of RHEED, kinematic theory is sufficient. The condition to obtain a Bragg spot is given by the equation $\mathbf{K}_{\|} = \mathbf{k}'_{\|} - \mathbf{k}_{\|}$ where $\mathbf{k}_{\|}$ is the component of the wave vector of the incident electrons parallel to the surface, $\mathbf{k}'_{\|}$ is the component of the wave vector of the electrons leaving to sample parallel to the surface and $\mathbf{K}_{\|}$ is a vector of the 2D surface reciprocal lattice. No similar condition for the component of the wave vector perpendicular to the surface applies. In the 3D problem we have discrete reciprocal lattice points, while in the 2D problem a rod normal to the surface is attributed to every reciprocal lattice point (h,k) as shown in figure 1.6. The wave vector $\mathbf{k}$ of the primary beam is positioned with its end at the (0,0) reciprocal lattice point and a sphere is constructed around its starting point. The condition for a constructive interference is fullfilled for every point at which the sphere crosses a rod. In fact electrons does not scatter only from the topmost lattice plane, but also from few underlying planes, so that the condition on the perpendicular component could not be completely neglected. For this reason some spots appears brighter.

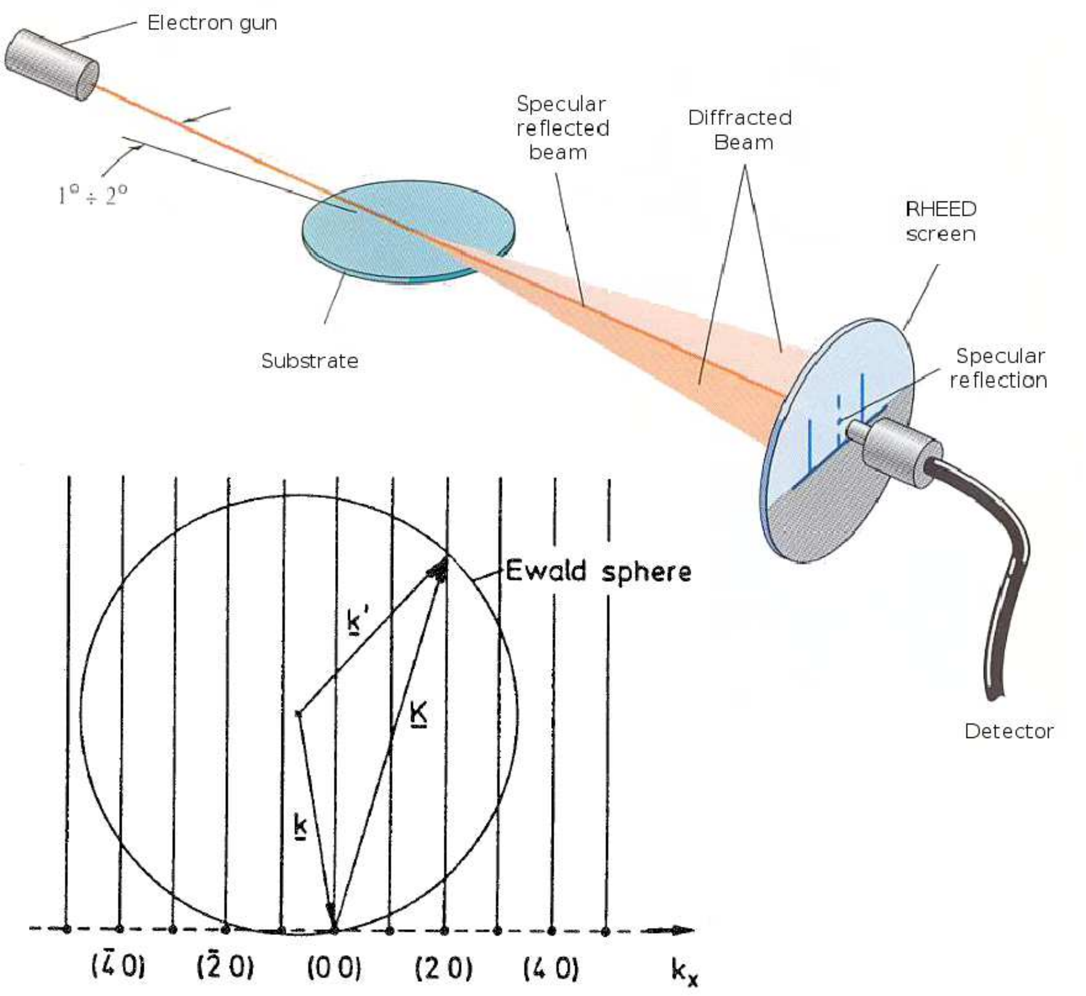

Figure 1.6: a reflection high energy electron diffraction system.

An important application for RHEED during the deposition is the monitoring of the layer-by-layer growth. Neave et al. [14] observed that during the GaAs film growth by molecular beam epitaxy, there were oscillations in the intensity of the RHEED pattern. These oscillations in intensity occurred immediately after the initiation of growth of GaAs over a wide range of substrate temperatures ($500 - 720°$C) and growth rates (Ga flux from 1×10^{13} to 1.5×10^{15} atoms cm^{-2} s^{-1}) for both doped and undoped material and independently from the surface reconstruction. It was shown that the period of the oscillation corresponded exactly to the monolayer growth rate on a (001) oriented substrate, where a monolayer is defined as one complete layer of Ga plus one complete layer of As. The amplitude of the oscillations was strongly damped, but it was not difficult to observe at least ten complete periods. It was thus obvious that the oscillations provided an absolute measurement of the growth rate. The observed behaviour was explained describing the equilibrium surface as quite smooth, and assuming the generation of random clusters during the growth. When growth started most adatoms desorbed before being incorporated in growing clusters, but as stable clusters nucleated and spread the growth rate increased, reaching a maximum at some fraction of a complete layer. When the nucleation of the next layer started, the growth rate decreased. This sequence was repeated, with gradual damping as growth became distributed over several layers. The complete surface therefore became distributed over many levels and the surface become rough. The changes observed in intensity of the specular beam in the RHEED pattern was related with the changes in surface roughness. The equilibrium surface was considered smooth, corresponding to high reflectivity. At the beginning of the growth clusters were formed at random positions on the crystal surface, leading to a decrease in the reflectivity. This can be predicted for purely optical reasons, since the de Broglie wavelength of the electrons is ~ 0.12 Å, while the bilayer step height is ~ 2.8 Å, i.e. the wavelength is at least one order of magnitude less than the size of the scatterer, so diffuse reflectivity results.

RHEED intensity oscillation can be used to finely calibrate the atomic fluxes from the effusion cells. It is possible to calculate the growth rate of the epilayer and the number of atoms sticking every second on the substrate.

The observation of RHEED pattern during the growth allows to monitor the surface reconstruction on the surface, to check the introduction of defects in the lattice and the presence of three-dimensional growth on the surface (see e.g. [15]). In figure 1.7 are reported RHEED pattern took after the nucleation of different amount of GaAs on Si at different substrate temperatures. For example, comparing panel (a1) and (c1) is possible to observe the different brightness of spotty and streaky pattern. The streaks are formed by the 2-dimensional periodicity of the surface reconstruction, and is clearly seen only on fairly flat surface. In flat surface conditions, the observation of the pattern along the main crystallographic directions makes possible to collect information about the surface reconstruction. The spots are due to electron transmission and diffraction inside surface roughness or 3-dimensional crystals on the surface. The streaks along $[111]$ direction in panel (b2) indicate the formation of facets along the $\{111\}$ planes on surface of the GaAs nanocrystals (e.g. [16, 13]). The extra spots positioned on one-third of neighboring points in the $[111]$ reciprocal directions in panel (c3) indicate that twin boundaries of $\{111\}$ types have been formed in the GaAs crystal. The presence of Debye-Scherrer rings in panel (a3) is due to the presence of poly-crystalline GaAs on the surface [13].

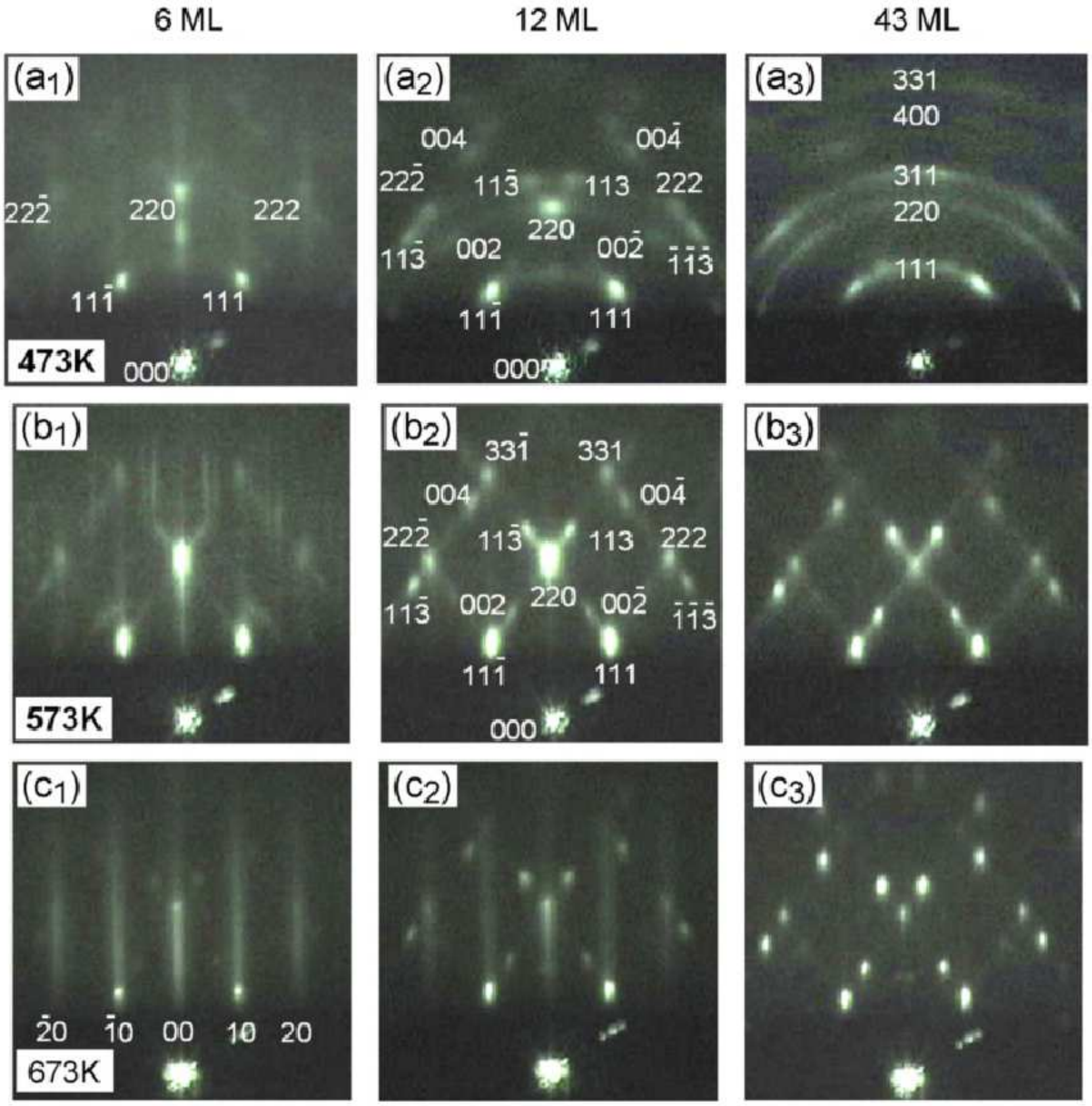

Figure 1.7: RHEED pattern for the growth of GaAs on Si with different conditions. From [13]

1.6 Self-assembled quantum dots

Self-assembled quantum nanostructures based on III-V semiconductors have provided vast opportunities for physical research and technological applications in the last 25 years [17]. These structures limit the carrier motion in one or more directions in regions with dimension similar to the de Broglie wavelength

$$\lambda = \frac{h}{p} = \frac{h}{\sqrt{3m_{eff}kT}} \tag{1.8}$$

where m_{eff} is the effective mass of the carrier and T is the temperature. Three different kind of nanostructures can be fabricated. In a quantum well the carrier is free to move in a plane and confined in only one direction, in a quantum wire the confinement is realized in two directions, in a quantum dot the carrier is confined in the three directions. For heterostructures based on GaAs, typical de Broglie wavelength is few hundreds of Å. The interest for these structures is mainly in the modification they introduce in the density of electronic states. In particular, the energy level structure of quantum dots is discrete, as in atoms. Quantum dots have provided vast opportunities for physical research and technological applications, such as quantum cryptography, quantum computing, optics and optoelectronics.

Several experiments for the fabrication of ultra thin layers for the study of size quantization effects were performed during the 1950s. The simplest case of quantum well is a thin layer between two layers of a different material. The first technique to be developed in the early 1980s for the fabrication of quantum dots was based on the removal by etching of material from a quantum well using a mask (created for example with electron beam lithography) to leave a pattern of islands. Another popular technique was the growth of islands using a patterned substrate. Only few years later the possibility to fabricate quantum dots using self-ordering was explored. Self-ordering is the spontaneous formation of periodically ordered domain structure with a periodicity much larger than the lattice parameter. An example of this behaviour is the heteroepitaxy of InAs/GaAs(001), in which InAs layer remains planar up to a characteristic coverage (critical thickness) above which three-dimensional islands form. Such growth mode, called Stranski-Krastanow, as we have seen in the previous section, was used to fabricate a regular pattern of island on the surface of a strained InAs/GaAs superlattice. The lattice mismatch in InAs/GaAs system is 7.2%. Initially the deposited InAs compresses to fit the lattice parameter of GaAs and layer by layer growth proceeds. However, with each additional layer, the strain energy accumulates until it becomes energetically favorable for islands to form, typically after 1.5 monolayers. A similar effect is obtained also for the growth of Ge on Si.

An example of application of InAs quantum dots is the fabrication of multistack low threshold current and high characteristic temperature laser diodes, as reported by Akahane et al. [18, 19].

Chapter 2

Droplet Epitaxy

A different technique for the fabrication of quantum nanostructrures by self assembly is the droplet epitaxy. Droplet epitaxy was proposed in 1991 by Koguchi et al. [20, 21] and is based on deposition at different times for the group III and group V elements. Group III elements such as Ga and In create a regular pattern of liquid droplet on a substrate kept at a temperature above the melting point of the selected element (e.g. 29.8 for Ga, 156.6°C for In), group V elements such as As and Sb are incorporated inside group III element droplets. With this method is possible to fabricate quantum dots with uniform size distribution in both lattice-matched and lattice-mismatched systems.

2.1 Fabrication of nanostructures by Droplet Epitaxy

To understand the principles of Droplet Epitaxy technique is possible to recall few key articles written in the last 20 years and reported in scientific literature.

2.1.1 Droplet epitaxy on inert substrate

The first article was written by Koguchi and Ishige [21] and showed the possibility to fabricate GaAs microcrystals by droplet epitaxy on substrates prepared to provide an inert surface during group III atom deposition and during group V atom incorporation. The inertness of the surface was provided by filling almost dangling bonds dipping the substrate in a $(NH_4)_2S_x$ solution and terminating the GaAs surface with S atoms.

Droplet epitaxy was performed depositing 2.7 monolayers of Ga on two different GaAs(001) substrates, the first prepared to have a S-terminated surface (inert) and the second with As-terminated surface (reactive). During the deposition the substrates were kept at 200 °C in ultra high vacuum environment (10^{-9}-10^{-10} torr) to maintain the contamination as low as possible. After this step a flux of As_4 with a beam equivalent pressure of 3×10^{-6} torr was supplied. During the growth the RHEED pattern was observed along $[110]$ and $[1\bar{1}0]$ directions. On the S-terminated substrate prepared for the Ga deposition a (2×1) surface reconstruction was observed. After liquid Ga deposition at 200 °C, RHEED pattern showed simultaneously the (2×1) reconstruction and an halo pattern, caused by the diffraction of the liquid Ga droplets deposited on the substrate surface. After the As irradiation the (2×1) surface reconstruction disappeared and RHEED pattern changed to spotty with clear strikes along the $[111]$ azimuth observed along $[110]$ direction. The spotty

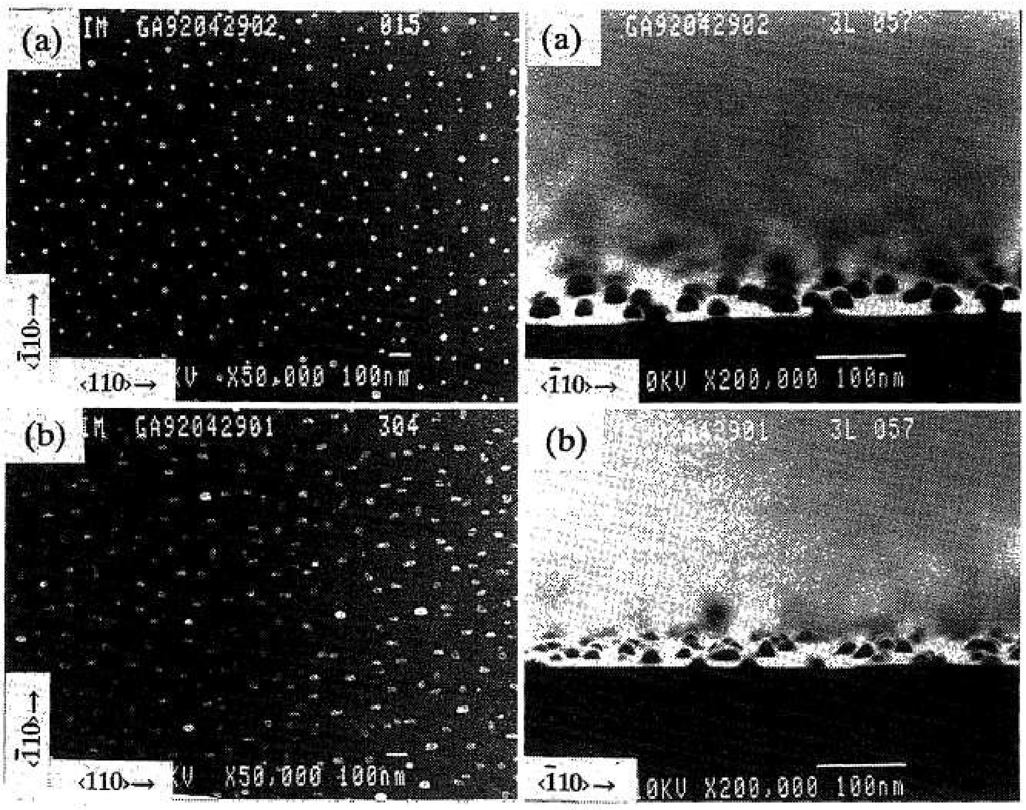

Figure 2.1: SEM images of surface morphology of the samples after Ga deposition (a) and after As irradiation (b) on S-terminated surface in top view (left panels) and side view (right panels).

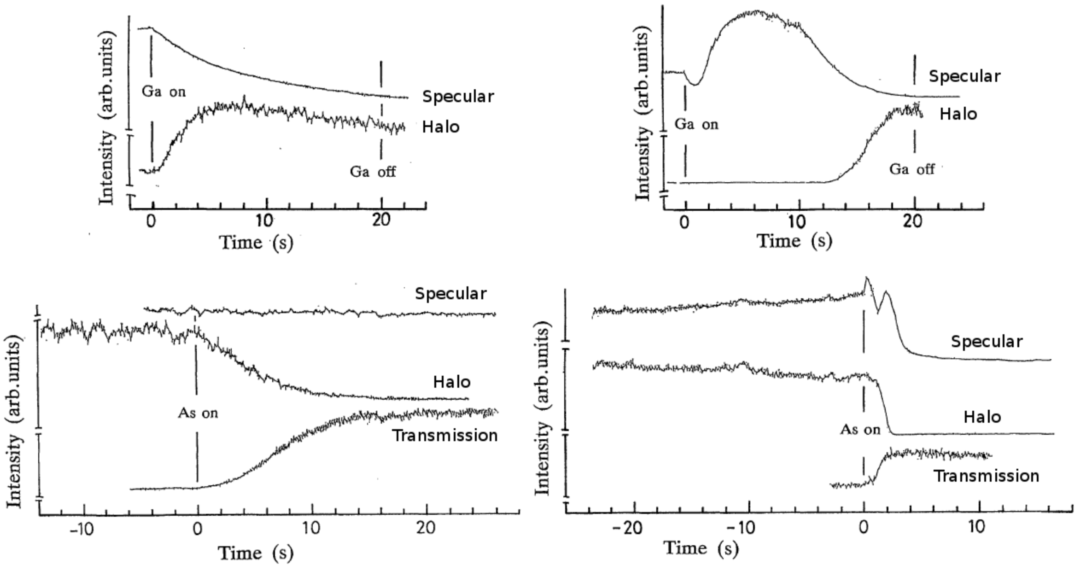

Figure 2.2: RHEED intensity changes during Ga deposition (upper panels) and As irradiation (lower panels) for S-terminated surface (left panels) and As-terminated surface (right panels).

pattern indicated the formation of 3D structures on the surface, the strikes the presence of facets. On the As terminated substrate prepared for the Ga deposition a $c(4 \times 4)$ surface reconstruction was observed. After the Ga deposition at 200 °C the surface reconstruction turned to (1×1) and an halo pattern appeared. After the As irradiation the halo disappeared and a (1×3) surface structure appeared, but no spotty pattern was observed. The surface morphologies were observed with scanning electron microscope (SEM) after Ga deposition and after As irradiation on both samples (figure 2.1). On the S-terminated surface hemispherical droplets with an average diameter of 24 nm with a standard deviation of about 15% were formed after the Ga deposition. The contact angle of the droplets was nearly 90°. The total amount of Ga in the droplets estimated from the hemispherical shape and from the diameter fitted the total amount of supplied Ga. This indicated that Ga atoms did not react with the surface. After As irradiation SEM images showed that the droplets became microcrystals with a rectangular base and $\{111\}$ facets. The mean dimensions of the bases were 25 nm × 43 nm with a standard deviation of about 20%. The height was about 15 nm and the $(\bar{1}11)$ facets better defined than (111) facets. Also on the As-terminated surface Ga droplets appeared, but the average diameter was smaller and the density appeared higher. The total amount of Ga in the droplets estimated from the hemispherical shape and the diameter was about 1 equivalent GaAs layer. The remaining amount of supplied Ga disappeared in the formation of a Ga stabilized surface on the substrate. SEM images took after subsequent As irradiation showed a smooth surface and no formation of microcrystals.

To understand these results is necessary to analyze the RHEED intensity during growth. Figure 2.2 shows the intensity change of specular beam, halo and (004) transmission spot during Ga deposition and As irradiation. During the Ga deposition on S-terminated substrate (upper left panels) the specular beam intensity decreased, while halo intensity increased suddenly when Ga flux was opened and then decreased. This behaviour was

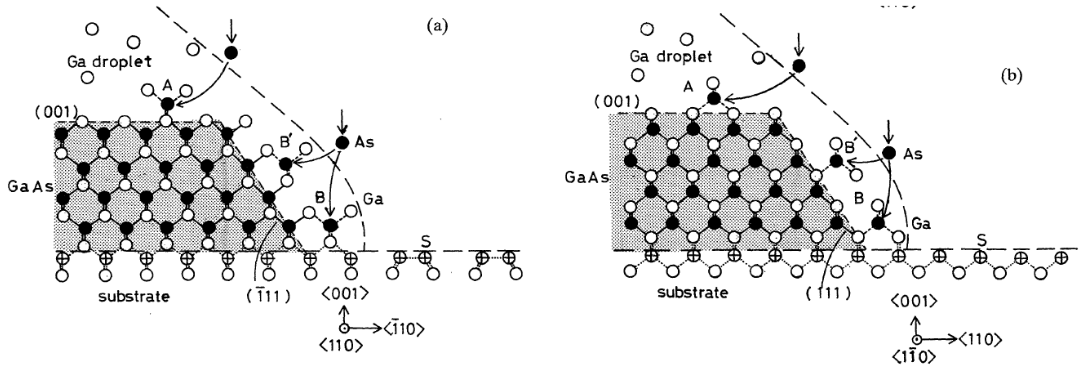

Figure 2.3: Schematic mechanism for the GaAs microcrystal growth on S-terminated surface. Cross sectional view along $\langle 1\bar{1}0 \rangle$ (left panel) and $\langle 110 \rangle$ directions.

caused by the absorption of the electron beam from the Ga droplets which increased in size as deposition time increased. During the As irradiation on S-terminated surface the intensity of the (004) transmission spot increased as the intensity of the halo disappeared (figure 2.2 lower left panel). On the As-terminated substrate the intensity of the specular beam was first reduced, then increased to a maximum value and finally decreased with the appearance of the halo corresponding to an amount of Ga of 1.75 equivalent GaAs monolayers (figure 2.2 upper right panel). During the As irradiation the halo intensity decreased rapidly and few oscillations were observed in the specular intensity, similar to the ones observed during GaAs growth by Deparis and Massies [22] and attributed to surface reconstruction changes between As-stabilized and Ga-stabilized surfaces. This behaviour indicates a layer by layer growth similar to mechanism of droplet formation and annihilation at high temperature described by Osaka et al. [23].

The growth mechanism and the observed anisotropy on base size of GaAs microcrystal is explained in figure 2.3. The microcrystals grow by adsorbing As atoms in sites A, B or B'. While sites B and B' are nearly equivalent on (111) surface, site B is much more stable than B' on $(\bar{1}11)$ surface. For this reason the base expansion of the microcrystal in the $[1\bar{1}0]$ direction is easier than the one in the $[110]$ direction, and As atoms in B' sites on the (111) surface easily dissolves.

2.1.2 The arsenization process

The second key article was written by Watanabe, Koguchi and Gotoh in 2000 [24]. This article showed the role of the parameters selected during As irradiation and the possibility to grow high quality quantum dots by droplet epitaxy without using sulfur. The use of sulfur resulted in S atoms remaining incorporated in the quantum dots, deteriorating the optical properties of the nanostructures. The first step of the growth procedure described in the article consisted in the preparation of an high quality $\mathrm{Al}_{0.3}\mathrm{Ga}_{0.7}\mathrm{As}$ barrier layer with a flat surface grown by molecular beam epitaxy at a substrate temperature of 580 °C. The creation of a barrier layer with higher gap material is necessary to obtain quantum confinement in the GaAs nanostructures. Droplet epitaxy was performed after reducing the substrate temperature to 200 °C keeping the background pressure in the range of 10^{-9}-10^{-10} torr. A total amount of 3.7 Ga monolayers were supplied on $c(4 \times 4)$ surface. Panel

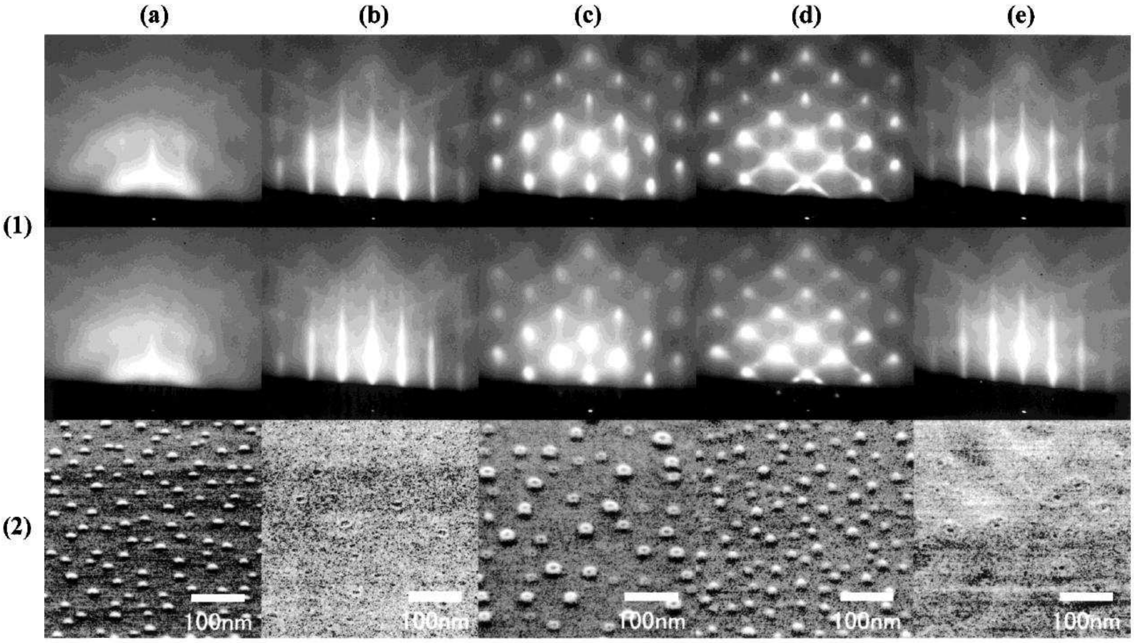

Figure 2.4: RHEED patterns (upper two rows) and SEM surface morphologies (lower row) of the samples at each stage of the growth process described in [24]. In (1), upper row shows the electron beam along $\langle 110 \rangle$, lower row along $\langle 1\bar{1}0 \rangle$. (a) is took after the Ga deposition at 200 °C. (b), (c), (d) and (e) are after subsequent As_4 irradiation with 4×10^{-7} torr at 200 °C, 4×10^{-5} torr at 200 °C, 4×10^{-5} torr at 150 °C and 4×10^{-7} Torr at 150 °C, respectively.

1a in figure 2.4 shows the halo in RHEED patterns along $[110]$ and $[1\bar{1}0]$ directions after Ga deposition. SEM images (panel 2a) showed hemispherical droplets with a density of 3.5×10^{10} cm^{-2} and a mean diameter of 10 nm. Arsenic irradiation was performed under four different conditions of substrate temperature and As flux. On first sample after As_4 irradiation with 4×10^{-7} torr at 200 °C, (1×3) streaky pattern with nodes appeared (panel 1b). The surface observed with SEM was flattened by layer by layer growth (panel 2b). On second sample As_4 flux was increased to 4×10^{-5} torr at a substrate temperature of 200 °C. A pattern composed by transmission spots and $\{111\}$ facets appeared (panel 1c) and surface showed crater-like GaAs microcrystals with a diameter larger than that of the Ga droplets (panel 2c). The third sample was irradiated with an As_4 flux of 4×10^{-5} torr after decreasing substrate temperature to 150 °C. RHEED pattern showed weak spots and $\{111\}$ facets (panel 1d). On the surface, SEM images revealed pyramidal quantum dots with a typical base size of 11×16 nm and a height of 6 nm (panel 2d). The last sample was irradiated with an As_4 flux of 4×10^{-7} torr after decreasing substrate temperature to 150 °C. RHEED pattern turned to nodular streak (panel 1e) and surface showed circular roughness with a radius ~ 3 times the radius of the crater seen on second sample (panel 2e). The growth mechanism can be qualitatively explained as follow. The As molecular beam irradiation after the Ga droplets formation give raise to two different growth processes. The first is a two-dimensional growth, in which As atoms are adsorbed on the Ga-stabilized surface and subsequently, Ga atom migrate from the droplets to the As-stabilized surface. The second is three-dimensional growth, in which As atoms are incorporated from the vapour phase directly into the droplets. The high As flux irradiation promoted 3D growth,

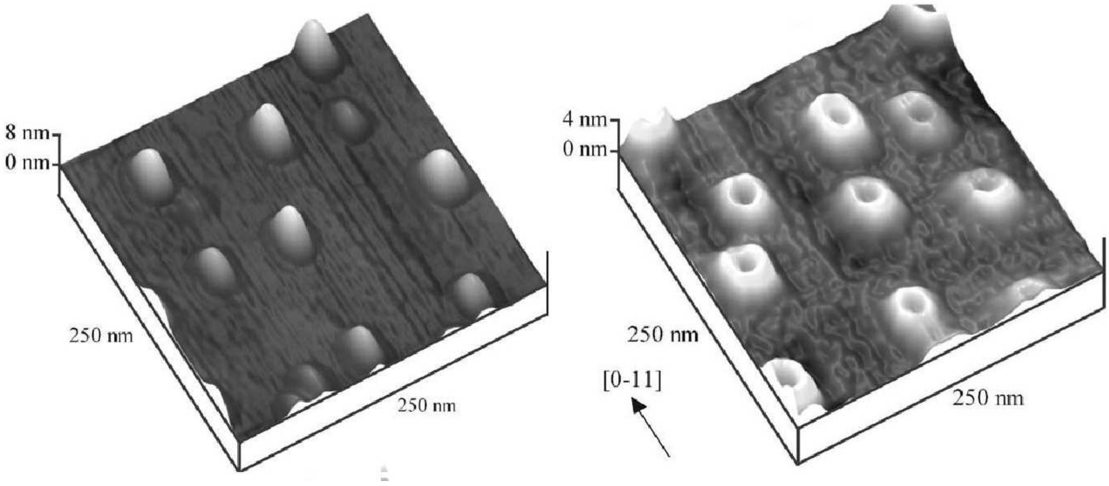

Figure 2.5: Atomic Force Microscope images of the Ga droplets after crystallization at 200° C with an As_4 flux of 2×10^{-4} (left panel) or 1×10^{-5} torr (right panel).

and reduced 2D growth due to Ga atom consumption. The low As flux promoted 2D layer growth. High substrate temperature enhanced Ga migration from the droplets, low substrate temperature is effective in suppressing Ga migration and 2D growth.

The possibility to obtain crater-like structures and their formation mechanism were explored in more detail by Mano and Koguchi [25], supplying 3.75 monolayers of Ga at 200 °C on a $c(4 \times 4)$ reconstructed GaAs(100) surface and then irradiating an As_4 flux of 2×10^{-4} or 1×10^{-5} torr at 200 °C. Atomic force microscope (AFM) images showed pyramidal quantum dots with base dimensions of 50 $\times$ 35 nm and a height of 7.5 nm for the high flux, well defined ring structures with an external mean diameter of 51 nm along $[0\bar{1}1]$ (figure 2.5) and 45 nm along $[011]$ for the low As flux. To better explain the crystallization mechanisms of GaAs nanostructures from Ga droplets two processes are considered. The first one is GaAs formation inside the droplets by As atom diffusion (process A). As atoms stuck on the droplet surface diffuse into the droplets and when they reach the interface between the droplets and the substrate, the As and Ga atoms change into epitaxial GaAs with some probabilities. The second process is GaAs growth at the edge of the droplets (process B). Since both Ga atoms from the droplets and As atoms from the flux are directly supplied to substrate surfaces, a very efficient crystallization is expected in this area. The two processes are correlated to each other and the final shapes of the nanostructures are determined by the balance of them.

It is evident that the growth of quantum nanostructures on AlGaAs or GaAs substrate must consider not only the As diffusion in the droplet, but also the Ga migration induced by the As-stabilized surface and the substrate temperature. Changing As flux and substrate temperature is possible to set a length for the gallium diffusion that will result in a larger radius for the GaAs nanocrystals.

2.1.3 Dots, rings and double rings

The third key article was written by Mano et al. [26] and showed the possibility to fabricate GaAs concentric quantum double rings structures by droplet epitaxy. In this work 3.75 monolayers of Ga were deposited at 300 °C on AlGaAs surface to obtain droplets with a

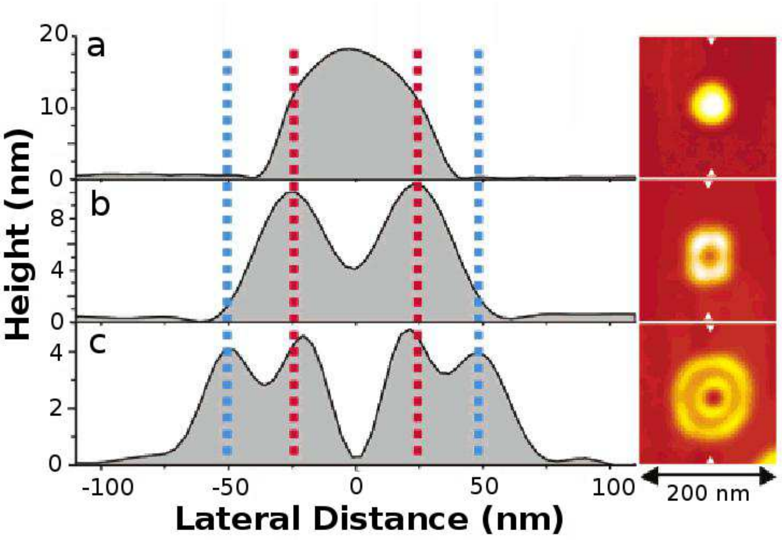

Figure 2.6: Cross section profiles along $\langle 0\bar{1}1 \rangle$ direction and Atomic Force Microscope images of Ga droplets (a) GaAs single rings (b) and GaAs concentric double rings (c).

density of 2×10^9 cm^{-2}. Irradiating the substrate kept at 200 °C with an As_4 flux of 8×10^{-6} is possible to fabricate ring-like nanostructures, with a flux of 2×10^{-6} double concentric quantum ring structures were obtained (figure 2.6). Comparing the cross sectional profiles of the droplets and of the single ring structures along the $[0\bar{1}1]$ direction, was observed that the lateral size of the ring (red-dotted lines in figure 2.6) was almost identical to that of the original Ga droplet. This suggested that a more effective crystallization occurs at the droplet boundaries where the Ga atoms react with the incoming As atoms. A further decrease in As flux intensity reduced the mean height of nanocrystals and gave raise to another ring, forming a concentric double-ring structure. The inner ring diameter was almost identical to that of the single ring seen previously; the outer ring was formed outside the first ring. This fact indicated the migration of Ga atoms away from the droplet. In the crystallization stage Ga atoms were mainly within the droplets and As atoms were densely dispersed on the surface far from the droplet. This concentration gradient started a migration of Ga from the droplet. The interpretation was supported by the fact that the outer ring diameter increased with decreasing As flux intensity, whereas that of the inner ring remained almost unchanged.

2.1.4 Shape control and role of surface reconstrution

To fully understand the formation of the outer ring outlined in the previous section, is necessary to refer to the last key paper, written by Somaschini et al. [27]. The article proposes an interpretation for the formation mechanism of quantum nanostructures grown by droplet epitaxy and presents the fabrication of multiple concentric nanorings. On the $Al_{0.3}Ga_{0.7}As$ barrier layer kept at 350 °C with a $c(4 \times 4)\beta$ surface reconstruction 10 monolayers of gallium were deposited. A first As_4 irradiation was performed for 20 seconds at a substrate temperature of 250 °C with a flux of 8×10^{-7} torr. A second As_4 irradiation on the same sample was performed with the same flux for 20 min at a substrate temperature of 300 °C. To determine the growth dynamics of the resulting nanostructures, morphological

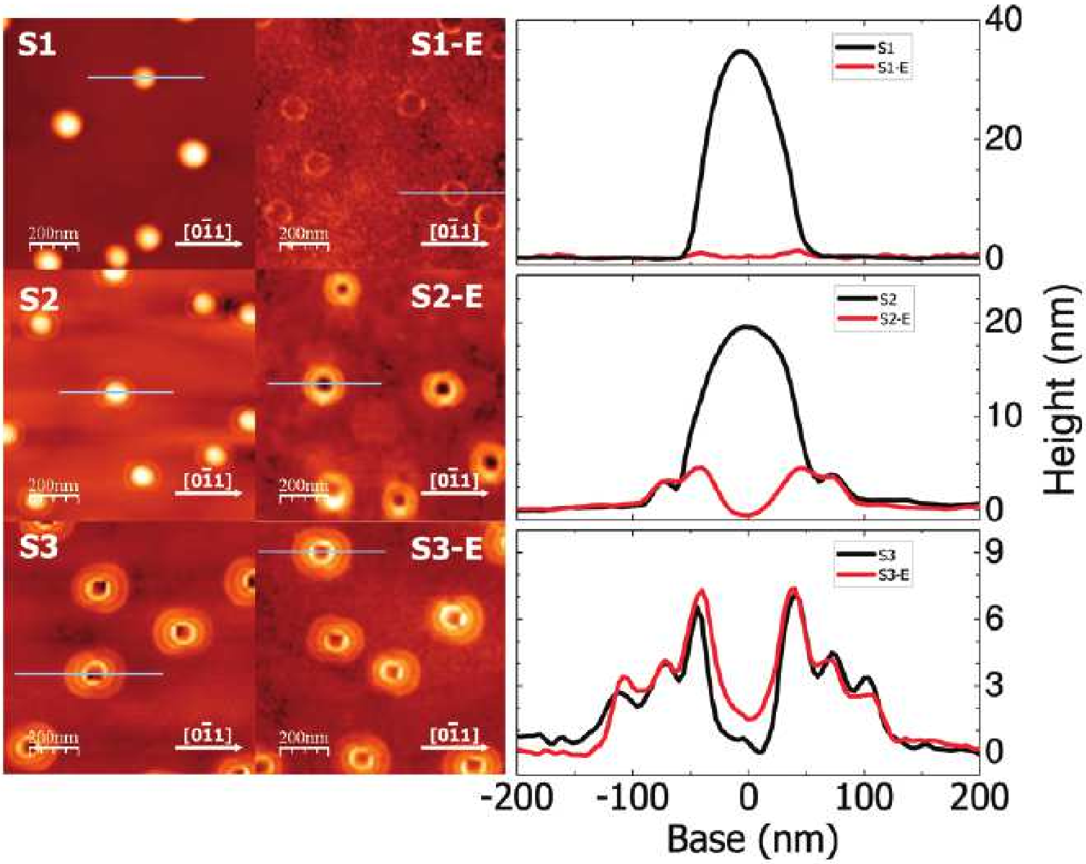

Figure 2.7: AFM images of as-grown samples S1, S2, and S3 (left panels), etched samples S1-E, S2-E, and S3-E (center panels), and corresponding line profiles taken along $[0\bar{1}1]$ direction (right panels). From ref.[27].

characterizations via ex situ AFM measurements were performed just after Ga deposition (S1), after the first arsenization (S2) and after the second arsenization (S3). Because after step S1 and S2 a certain amount of unreacted Ga was present on the surface, pieces of samples S1, S2 and S3 were selectively etched for pure metallic Ga and the etched samples were named S1-E, S2-E, and S3-E, respectively. In figure 2.7, the AFM images and the typical line profiles of the six samples are reported. After the 10 MLs Ga supply at 350 °C (sample S1), nearly hemispherical Ga droplets were formed with an average diameter of around 80 nm, height around 35 nm, and a density of around 8×10^8 cm^{-2}. Only after the etching treatment (sample S1-E) it was possible to identify the presence of a GaAs ring structure under the original droplet coming from the crystallization at the droplet's edge. After the first arsenization step (sample S2) the formation of a complex structure composed by a central dome with the same radius of the initial Ga droplet, surrounded by a shallow ring of about 140 nm diameter was observed. The etching procedure revealed that the short time supply of As did not completely crystallize the Ga atoms in the droplet. The AFM analysis of the etched sample (S2-E) clearly showed that the central dome was made by metallic Ga. The exposed GaAs surface of sample S2-E showed the formation of a double ring structure, whose inner ring was hidden inside the liquid Ga. The final As supply (sample S3) completely crystallized the Ga atoms by forming the outermost third ring structure with a diameter of around 210 nm. At this point, a complete GaAs triple concentric nanoring structures was obtained. After etching (sample S3-E), no evident change was found on the morphology of the surface, thus showing that no unreacted Ga was present. It is clear that the internal and external rings did not shared the same origin. While the two external rings were formed during the two arsenization steps, the inner ring was already formed after the Ga droplet deposition, when no intentional As flux was supplied to the sample. This can be explained by observing that during and after the Ga deposition As atoms coming from the substrate are dissolved into the liquid Ga. This gave raise to a gradient in As concentration inside the droplets, resulting in a gradient of the surface tension that caused an internal convection flux. This mechanism was responsible for the transportation of the As atoms to the edge of the droplet, resulting in the formation of the GaAs inner ring at the droplet's edge. This mechanism was confirmed by the increase of the inner ring height after one hour inside the growth chamber without any arsenization step.

The formation of the two outer rings was explained in terms of balance between the Ga migration from the droplet and As flux. To understand such mechanism, the role of sur-

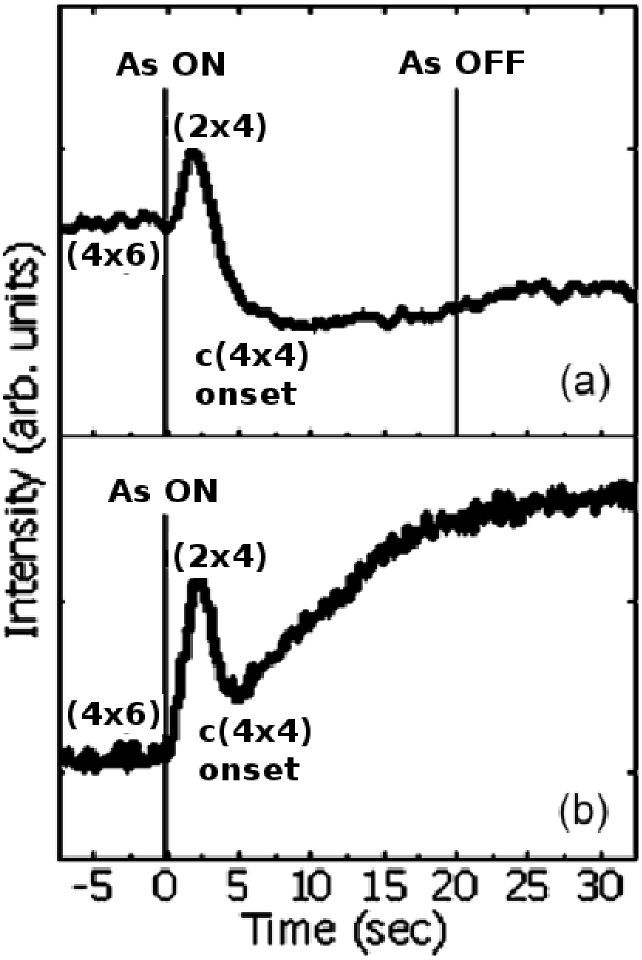

Figure 2.8: Specular beam intensity change as a function of time (a) during the 20 s As supply of 8×10^{-7} Torr at 250° C and (b) during the As supply of the same intensity at 300° C. From [27].

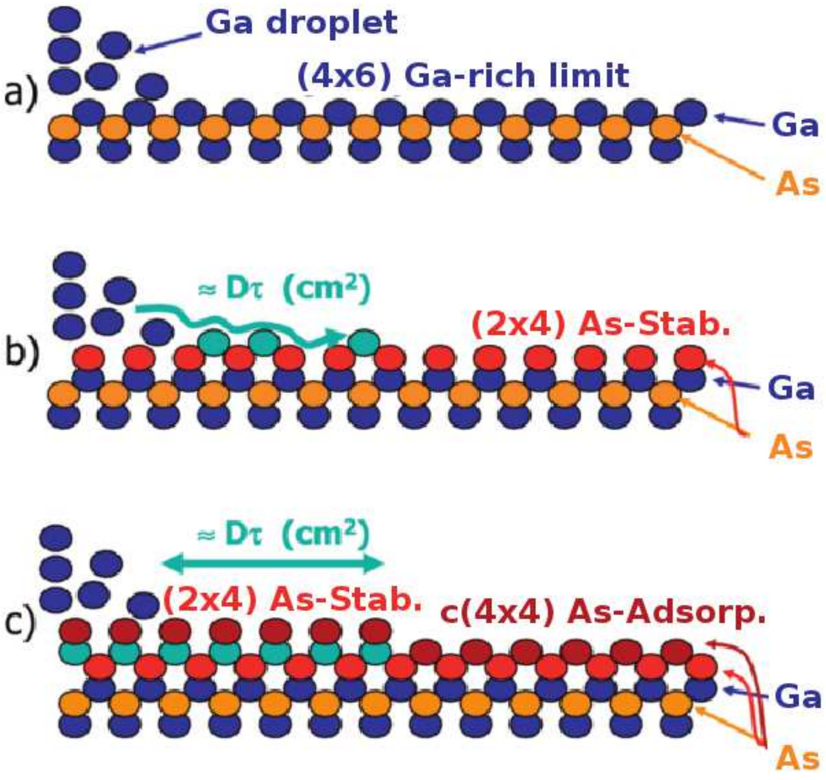

Figure 2.9: Schematic explanation for the formation of outer rings structures. Ga droplets on the Ga-rich (4×6) surface reconstruction (a). Ga atoms from the droplets can migrate covering a mean displacement area of $\sim D\tau$ on (2×4) surface reconstruction appeared during As supply (b). Away from the droplet the surface turns to the As-rich c(4×4). The border of this area act as a pinning site for the migration of the Ga atoms (c). From [27].

face reconstruction is of the utmost importance. The RHEED pattern changed to a (4×6) surface reconstruction just after 1.7 MLs supply of Ga. During arsenization steps the surface reconstruction changed from the Ga-rich (4×6) to As-stabilized (2×4) and finally to As-rich c(4×4) surface reconstruction. Figure 2.8 shows the intensity change of specular-beams in RHEED, during the two arsenization steps. In both steps, the specular-beam intensities increased first, showing the maximum after two seconds of As irradiation, when the formation of (2×4) surface reconstruction was observed, then decreased to the minimum after further three seconds supply of the As flux, corresponding to the initiation of the c(4×4) reconstruction. The final increase in intensities was related to the establishment of an ordered c(4×4) surface reconstruction. The mechanism proposed in [27] for the growth is reported in figure 2.9. Just after the irradiation of the first 1.7 MLs of Ga the surface reconstruction changed from c(4×4) to (4×6) and the Ga droplets were formed with the 8.3 MLs of Ga supplied. On both As irradiation steps, an As-stabilized (2×4) surface reconstruction started to raise and some Ga atoms started to migrate from the droplet forming a monolayer of GaAs on a circular area $\sim D\tau$, where D is the surface diffusion coefficient of Ga atoms and τ the average time interval between arrival and adsorption of As atoms at a specific site. In the meantime, on the surface not affected by Ga migration, As adsorption caused a reconstruction change to c(4×4). The formation of the

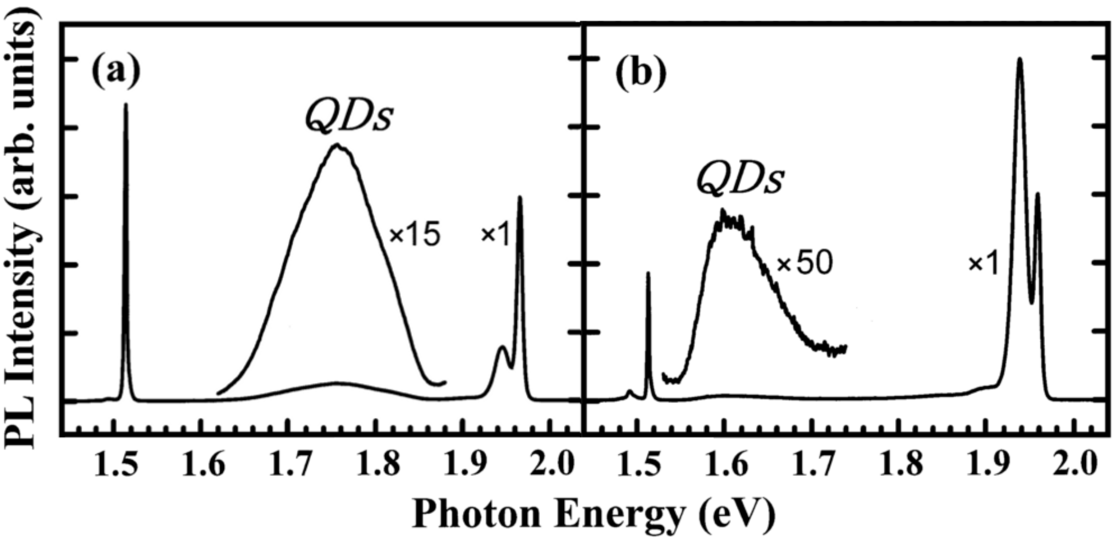

Figure 2.10: Photoluminescence spectra of QDs with different size, 11nm $\times$ 16nm $\times$ 6 nm (a) and 17nm $\times$ 24nm $\times$ 10 nm (b). From [24].

external rings was explained by Ga atoms diffusing on (2×4) surface and crystallized by the As excess at the boundary of the c(4×4) area.

2.2 Photoluminescence of quantum dots grown by droplet epitaxy

The opportunity to fabricate thin layers or nanostructures with a low band gap material in a matrix of a material with high band gap using the molecular beam epitaxy, opens the possibility to control the confinement potential of electrons and holes thus determining the optical and electronic properties of the system [28, 17]. In the GaAs/AlGaAs system (GaAs has a band gap at low temperature of about 1.52 eV, $Al_{0.3}Ga_{0.7}As$ of about 1.97 eV) the carriers are confined in the spatial region with lower energy gap by potential barrier corresponding to the half of the band mismatch between the two materials. In a GaAs quantum dot this confinement exists in all the three spatial directions, and the motion of a carrier resembles the one of a particle in a box described by quantum mechanics.

An effective way to investigate the electronic properties of the quantum nanostructures and the quality of the epitaxial layers is the photoluminescence. Photoluminescence (PL) is a technique in which photons with energy greater than the energy gap of the barrier layer are sent onto the sample surface. Depending on the absorption coefficient of the material, part of the radiation is absorbed and electron-hole pairs are formed. After carrier diffusion and intra-band thermal transitions, the pairs are recombined through radiative and non-radiative inter-band recombination. Collecting the signal is possible to investigate the electronic properties of the quantum nanostructures and the quality of the epitaxial layers grown inside the sample. Depending on the size of the excitation spot on the sample, we have macro-PL (several hundred μm^2 and signal coming from a large number of nanostructures) or micro-PL (signal coming from only one or few nanostructures).

An example of macro-PL measurements at low temperature (20 K) of GaAs quantum nanostructures inside an AlGaAs buffer layer is reported in figure 2.10. The spectral range was delimited by the double peak at ~ 1.96 and ~ 1.94 eV, related to $Al_{0.3}Ga_{0.7}As$ buffer (bound exciton and donor-acceptor respectively [29]), and the double peak at ~ 1.51 and ~ 1.49 related to GaAs layer (again, bound exciton and donor-acceptor respectively [29]). The full width half maxima of the bound exciton peaks are indicators for the quality of the layers. Few meV means good layer quality. The peaks appeared at 1.76 eV (left panel in figure 2.10) and 1.61 eV (right panel in figure 2.10) were due to radiative recombination from the GaAs quantum dots. The different size of the dots on the two samples leaded to a different emission energy. In first approximation this can be understood from quantum mechanics considering the carriers in a dot as particles in a spherically symmetric potential. The calculated eigenvalues for the energy levels are discrete and $\propto r^{-2}$ where r is the radius of the nanostructure. As expected the PL signal from smaller nanostructures appeared at higher energy than the energy of bigger nanostructures. The full width half maxima of the PL emissions was related to size dispersion of the dots and eventually to the presence of emission from the excited states. Finally, the emission intensity from the dots was poor if compared to the one from the barrier. This means that radiative recombination from the nanostructures was not efficient.

To improve the emission from the GaAs quantum dots a post-growth annealing (PGA) was introduced [30]. The results for a PGA of 60 minutes in As_4 atmosphere with temperatures between 520 and 760 °C was an enhancement in photoemission and a shift in the emission peak toward higher energy. As explained in detail in [31, 32], the two effects arose from the interdiffusion of group III atoms and the improvement in the quality of barrier material. The diffusion length of Al is thermally activated and proportional to annealing temperature. Sanguinetti et al. [31] took into account the effect of interdiffusion by considering isotropic diffusion of Al and Ga atoms with a diffusion coefficient independent of the Al concentration. Under this approximation the Al concentration X in the quantum dot varies as [33]

$$X(\vec{r}) = [8\pi l(T)]^{-3/2} \int X_0(\vec{r}_1) exp \left[\frac{(\vec{r} - \vec{r}_1)^2}{4l^2(T)} \right] d\vec{r}_1 \tag{2.1}$$

where $X_0(\vec{r})$ is the initial Al fraction, $l(T)$ is the temperature-dependent interdiffusion length at the GaAs/AlGaAs interfaces. Following this model, Al atoms diffused inside the GaAs dots reducing their size and smoothing the Al composition of the interface as shown in 2.11. The smaller size of the GaAs nanostructures leads to the observed blue shift in the emission wavelength.

The second effect is the recovery of the crystalline quality of the quantum nanostructures and of the barrier material. The low temperature set for the arsenization of the quantum dots and the low temperature during the growth of part of the AlGaAs barrier, was expected to introduce several defects in the crystal lattice. The annealing process was known to enhances the quality of the interface between the dots and the barrier, removing defects and thus improving the photoluminescence signal from the dots.

2.2.1 Calculation of electronic states in nanocrystals

To calculate the energy of the electronic levels in a quantum dot, quantum mechanics and the effective mass approximation (EMA) are used. The approximation consists in summarizing the real band structure inside the semiconductor into the effective mass and the energy of the carrier. These values are took in the extreme points of the valence or

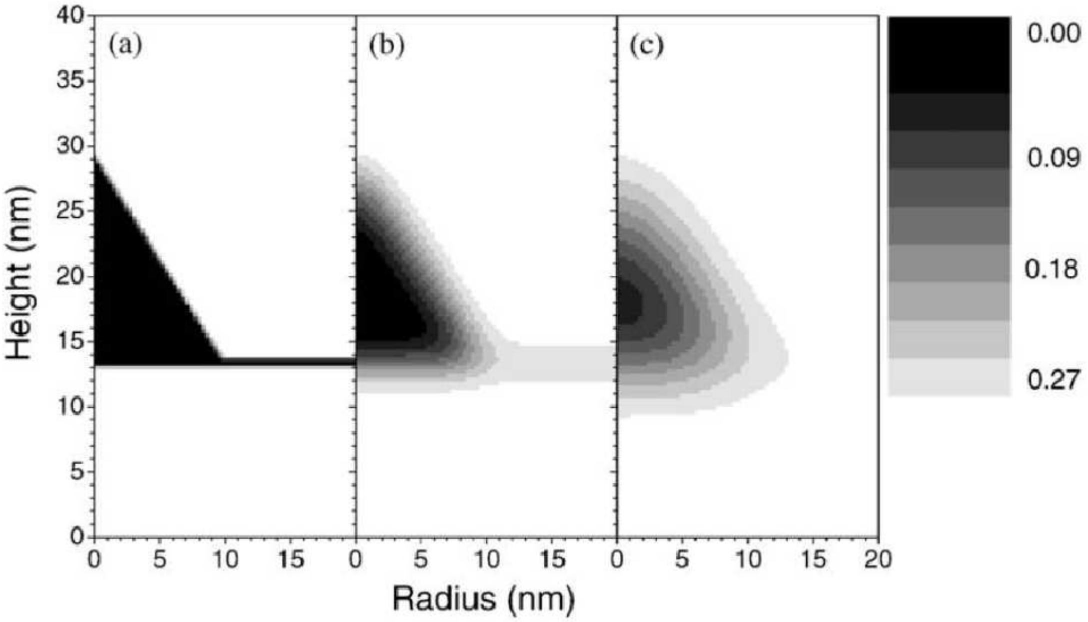

Figure 2.11: calculated QD Al concentration profiles at different interdiffusion length: 0 nm (a), 1 nm (b) and 2 nm (c). From [31].

conduction band, where the bands have a parabolic shape. If we consider the Schrödinger equation for a perfect crystal in a 1D system

$$H_{per}\phi_{n,k}(x) = \epsilon_{n,k}\phi_{n,k}(x) \tag{2.2}$$

the solutions $\phi_{n,k}(x)$ are the Bloch functions. If a perturbation V_p such as a dopant atom or a quantum dot is added to the perfect crystal, the hamiltonian that describes the system is modified as follow

$$[H_{per} + V_p]\,\Psi(x) = E\Psi(x) \tag{2.3}$$

The perturbation theory states that the solutions for the perturbed system can be built from the unperturbed ones as follows

$$\Psi(x) = \sum_n \int_{-\pi/a}^{\pi/a} \chi_n(k)\phi_{n,k}(x)\frac{dk}{2\pi} \tag{2.4}$$

The solution can be simplified by some assumptions. The first is that only the electrons in the minimum of the conduction band and holes in the maximum of valence band have a role in the building of the wave function associated to the system. The second that the perturbation V_p is varying slowly in space. With these assumptions the wave function solution for the perturbed system can be written as the Bloch function in the minimum of the band multiplied by an envelope function that gives the correction for the perturbation

$$\Psi(x) = \phi_{n,0}(x)\chi(x) \tag{2.5}$$

Using the envelope functions in the Schrödinger equation and the assumption about the parabolic bands, we obtain the energy values

$$\epsilon_n(k) = E_c - \frac{\hbar k^2}{2m_0 m_e} \tag{2.6}$$

The overall 3D Schrödinger equation for the perturbed system is then

$$\left[-\frac{\hbar k^2}{2m_0 m_e}\nabla^2 + V_p(R)\right]\chi(R) = E\chi(R) \tag{2.7}$$

What we obtain is an equation similar to one that describes a free electron with a perturbation potential. The only difference is that the effective mass is considered.
One of the simplest solution for this system can be calculated if we consider a spherical potential and a infinite height barrier between the material inside and outside the dot. For this system the eigenvalues are

$$E_n = \frac{\pi\hbar^2}{2m_e R^2}n^2 \tag{2.8}$$

From this equation is clear that the energy levels are discrete and that the eigenvalues have a larger values for smaller nanostructures.
In this work of thesis the calculations to obtain the energy for the levels were performed using the Schrödinger equation and the effective mass approximation following the method outlined in Marzin and Bastard [34]. The approach is to consider a nanostructure described by a height Z_c and a radius R with a cylindrical symmetry. The wavefunctions must vanish on the surface of the nanostructure. The solutions for the one particle hamiltonian

$$H_{e(h)} = E^{z}_{ce(h)} + E^{r,\theta}_{ce(h)} + V_{e(h)}(z,r) \tag{2.9}$$

where

$$E^{z}_{ce(h)} = -\frac{\hbar^2}{2}\left(\frac{\partial}{\partial z}\frac{1}{m^{z}_{e(h)}(z,r)}\frac{\partial}{\partial z}\right) \tag{2.10}$$

$$E^{r,\theta}_{ce(h)} = -\frac{\hbar^2}{2}\left(\frac{1}{r}\frac{\partial}{\partial r}\frac{1}{m^{r}_{e(h)}(z,r)}\frac{\partial}{\partial r} + \frac{1}{m^{r}_{e(h)}(z,r)}\frac{1}{r^2}\frac{\partial^2}{\partial\theta^2}\right) \tag{2.11}$$

and the potential $V_e(z,r)$ is built with the Heavyside function to fit the shape of the dot radially and in height. The terms $m^{z}_{e(h)}(z,r)$ and $m^{r}_{e(h)}(z,r)$ are the electron (hole) effective mass for the motion along z or along its perpendicular plane. The solutions that fulfil equation (2.9) and the boundary conditions can be decomposed on the basis formed by products of Bessel functions of integer order n by sine functions of z

$$\chi_n(r,z,\theta) = \sum_{i>0,j>0} A^{n}_{i,j}\xi^{n}_{i,j} \tag{2.12}$$

$$\xi^{n}_{i,j}(r,z,\theta) = \beta^{n}_{i} J_n(k^{n}_{i} r)e^{in\theta} sin(K_j z) \tag{2.13}$$

where $k^n_i R$ is the i-th zero of the Bessel function of integer order $J^n(x)$, $K_j = 2j\pi/Z_c$, and where β^n_i is a normalization factor. Each value of n yields a family of solutions. The matrix elements are given by

$$\langle\xi^{n}_{i,j} \mid E^{z}_{ce(h)} \mid \xi^{n}_{i,j}\rangle \tag{2.14}$$

and

$$\langle\xi^{n}_{i,j} \mid E^{r}_{ce(h)} \mid \xi^{n}_{i,j}\rangle \tag{2.15}$$

The parameter used in the calculations are reported in table 2.2.1.

Calculations performed with the outlined method for the GaAs quantum dots grown by droplet epitaxy gives results in good agreement with experimental data. In ref. [31] the

	Band mismatch (eV)	$m_{r,z}^{GaAs}$	$m_{r,z}^{AlGaAs}$
Electrons	-0.262	$0.067m_0$	$0.093m_0$
Holes	-0.195	$0.51m_0$	$0.57m_0$

Table 2.1: Parameters

quantum dots were approximated by cone with values for the height and the base obtained by scanning electron microscope images. Taking into account the change in the profile of the dot induced by the annealing procedure, the calculated ground state transition for a dot was 1.61 eV, with ground-to-excited states energy separation of 70 meV, in nice agreement with the macro-PL results of 1.63 eV for the ground state emission and 70 meV ground-to-excited state separation.

In ref. [35] Kuroda et al. performed the same calculations for single and quantum double

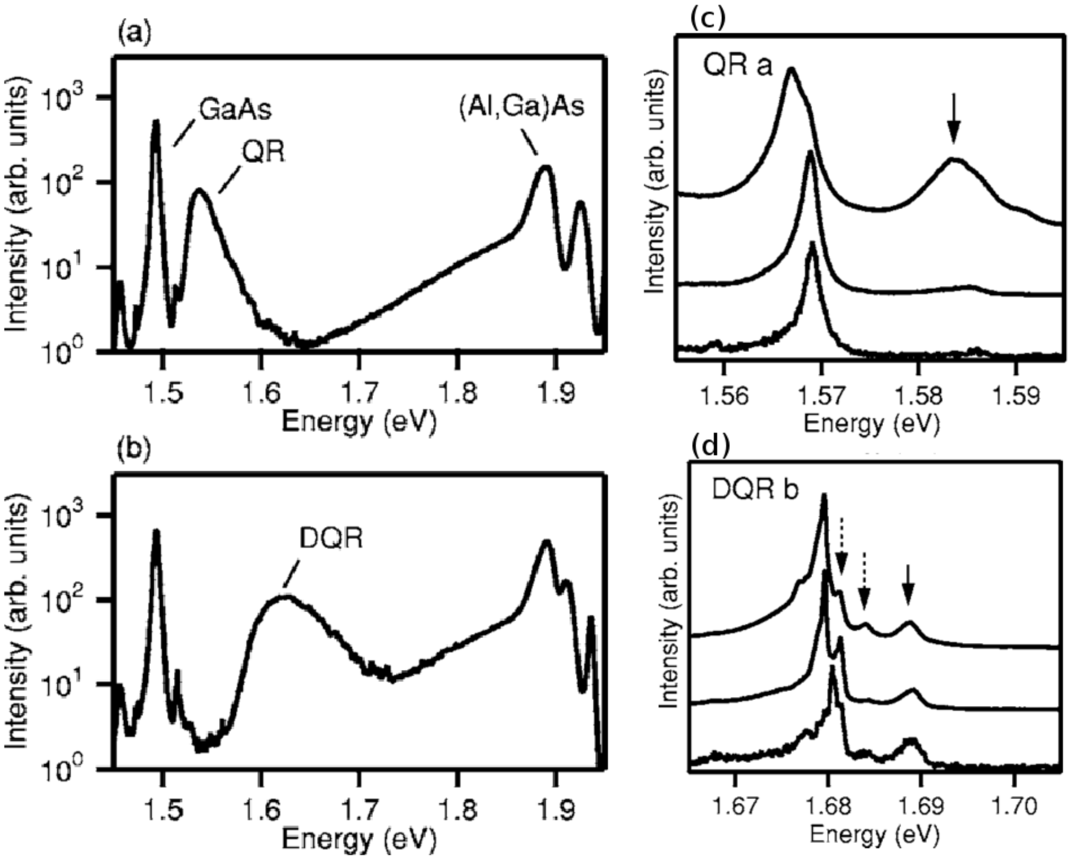

Figure 2.12: far-field emission spectra of the sample with quantum rings (a) and quantum double rings (b) at 5 K with excitation density of 50 mW/cm^2 (left column). Emission spectra for quantum rings (c) and quantum double rings (d). The respective excitation densities were, from bottom to top, 1, 10, and 30 W/cm^2. Spectra are normalized to their maxima and offset for clarity. From [35].

ring structures, presenting PL measurement for broad area and for single nanostructures. Left column of figure 2.12 shows macro-PL spectra of quantum rings (a) and quantum double rings (b). For spectrum (a) the broad emission band at 1.544 eV was attributed

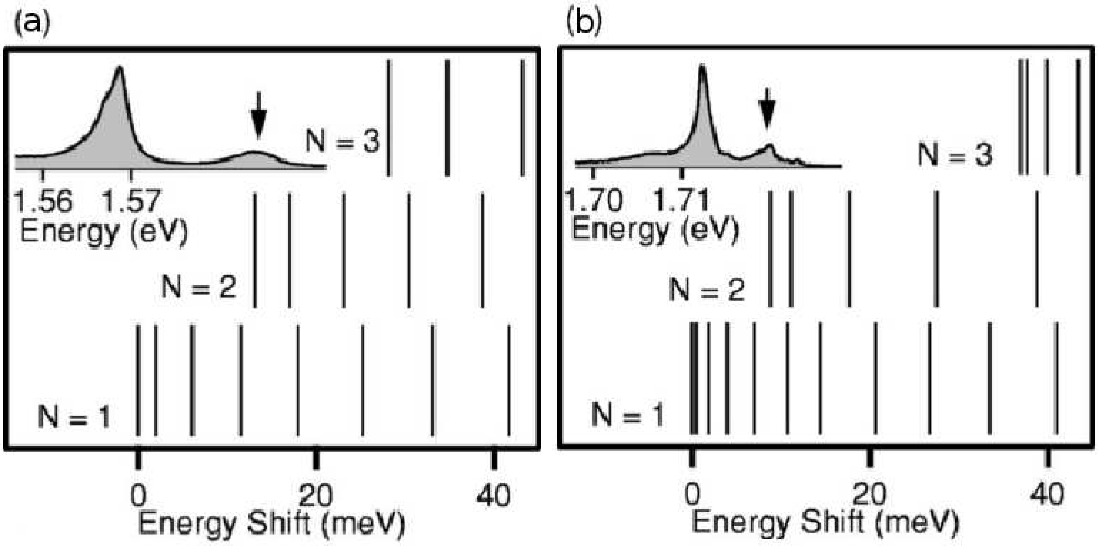

Figure 2.13: series of optical transition energies in quantum rings obtained by the calculation. The micro-PL spectrum of quantum ring at 15 W/cm^2 is shown in the inset (a). The energies of optical transitions in quantum double ring with the micro-PL spectrum at 10 W/cm^2 is reported in inset (b). From [35].

to recombination of an electron and a hole confined in GaAs quantum rings. The line broadening (28 meV) was caused by the size distribution of the rings. Several emission components ranging from 1.7 eV to 1.95 eV were assigned to the presence of impurities and imperfections in the AlGaAs barrier. For spectrum (b) the emission band at 1.628 eV was originated from recombination of the ensemble of quantum double rings. The full width half maximum was 49 meV. The difference in PL energy of double rings compared to that of rings was attributed to the smaller height of double rings. Smaller height induced stronger confinement along the growth direction than in the lateral in-plane direction thus enhancing the confinement energy and causing a blue shift in the PL spectrum. Micro-PL measurements on single quantum ring structure are shown in inset (c). The emission line appeared at 1.569 eV and was attributed to recombination of an electron and a hole, both occupying the ground state of the ring. Increasing excitation intensity a new emission line, indicated by an arrow in figure, emerged at 1.582 eV. Further increase in excitation density caused saturation in the intensity of the original line along with a nonlinear increase in the new line. The satellite line was attributed to electron-hole recombination from an excited level of the ring. The presence of multiple carriers inside a ring also modified the energy levels by the Coulomb interaction among carriers so that for high excitation the ground-state emission was shifted to lower energy. Incoherent collision process among carriers caused also spectral broadening. Similarly to quantum rings, the micro-PL spectra of quantum double rings consisted of a main peak and a satellite one at the high energy side of the main peak. The former was associated with recombination of carriers in the ground state, the latter from the excited states. The satellite peak is present also at the lowest excitation. At high excitation several additional lines are superimposed on the spectra and were attributed to the presence of fine energy structures.

The calculation performed on transition energies for single-carrier levels of quantum rings and quantum double rings are shown in figure 2.13 panel (a) and (b) respectively. Because the system has cylindrical symmetry, each level is specified by the principal quantum number N and the azimuthal quantum number L corresponding to the angular momentum. Two levels with ±L are degenerated at zero magnetic field. Calculations showed that for quantum double rings the electron of N=1 is confined mainly in the outer ring, the electron of N=2 is in the inner ring, and that of N=3 is situated in both rings. Dominant contributions to the optical transition occur from the recombination of electrons and holes characterized by the same quantum numbers. The optical transitions connecting electrons and holes with different quantum numbers have oscillator strengths at least one order of magnitude lower than that connecting electron and holes with the same quantum numbers.

Chapter 3

Heteroepitaxy of GaAs on Silicon

3.1 Crystal structure and surface reconstruction of GaAs, Si and Ge

Silicon and Germanium are group IV elements and are important semiconductor materials, widely used in electronic device fabrication. They have a diamond lattice that is composed of two interpenetrating face centred cubic (FCC) lattices, one displaced from the other by $1/4$ of a lattice constant in each direction. Each site is tetrahedrally coordinated with four other sites in the other sublattice. GaAs is a III-V semiconductor with a zinc-blende lattice, similar to the diamond structure but with the two FCC sublattices of different atoms. On semiconductor surfaces the position of the atoms and the surface atomic structure usually does not agree with that of the bulk. In semiconductors the distortion of the bulk-like atom configuration due to the existence of a surface, leads to the breakage of several tetrahedral bonds. Several rearrangements of surface atoms are possible. A compression of the topmost or of top few interlayer separations is called relaxation, the change in the periodicity parallel to the surface is called reconstruction. Usually surface reconstruction saturate free dangling bonds by forming new bonds, thus decreasing the surface free energy [7]. The new arrangement for the few topmost layers could be usually described by a 2D Bravais lattice.

For GaAs(001) it has been reported that a rich variety of reconstructions are formed depending on surface stoichiometries. The surface reconstructions range from the most As-rich $c(4\times4)$, through (2×4), (6×6), and $c(8\times2)$, to the most Ga-rich (4×6) phases. Here the surface reconstructions observed during this work of thesis are described. The As-rich (2×4) reconstruction usually is present during the MBE growth and for this reason has been extensively studied. Under different conditions of substrate temperature and As flux, different phases (α, β, γ, $\alpha2$, $\beta2$ and $\beta3$) are known [36]. The structure model for the $\beta(2 \times 4)$ reconstruction has three As dimers on the topmost layer (this means 6 As atoms on 8 possible sites and so means an As coverage of 0.75 MLs, see fig. 3.2), the $\beta2(2 \times 4)$ and the $\alpha(2 \times 4)$ two As dimers, the $\gamma(2 \times 4)$ four As dimers and the $\beta3(2 \times 4)$ only one As dimer.

The $c(4 \times 4)$ reconstruction is usually observed under extremely As-rich MBE conditions, when the As/Ga flux ratio is increased and/or when the substrate temperature is lowered.

As shown in right panel of figure 3.3, the $c(4 \times 4)\alpha$ has on the topmost layer three Ga-As dimers and 8 As atoms (the 8 As atoms on the boundary are shared with the neighboring cell), and As coverage for this reconstruction is 1 ML. The $c(4 \times 4)\beta$ (left panel of figure

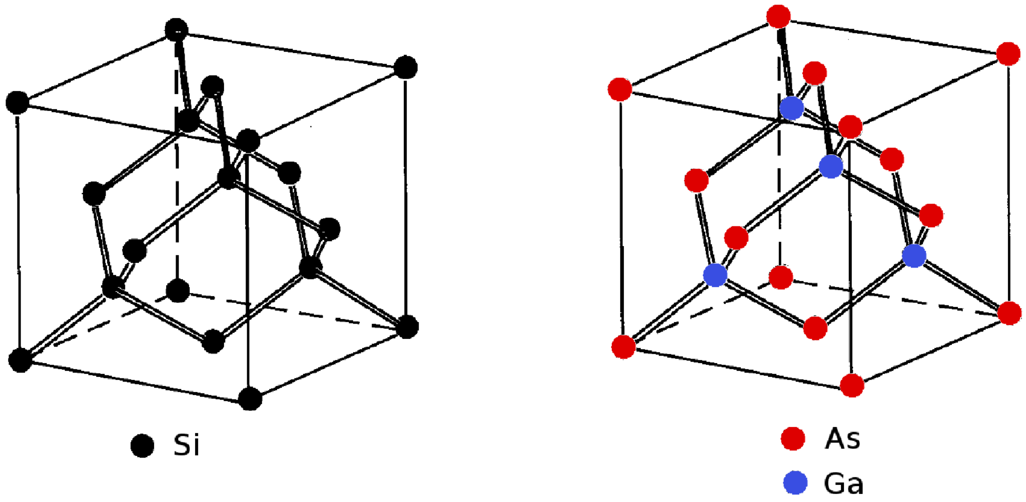

Figure 3.1: the crystal structure of diamond and zinc-blende

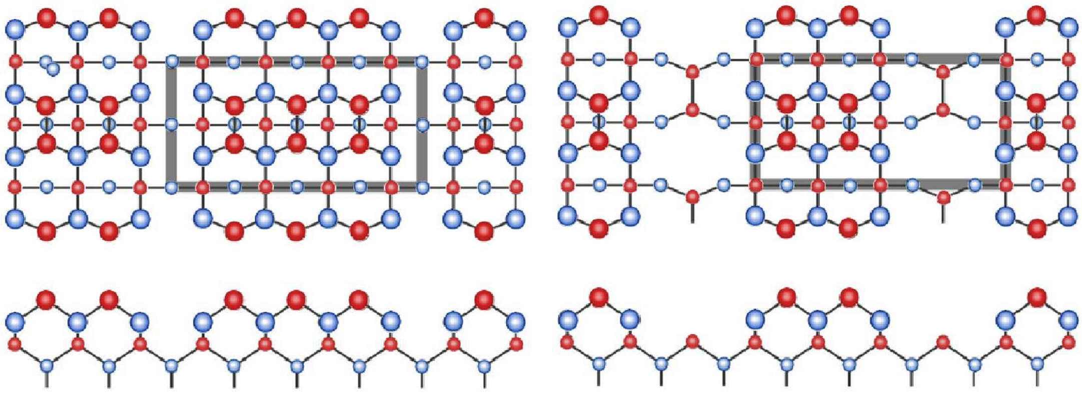

(a) β model.

(b) $\beta2$ model.

Figure 3.2: structure models for As-rich GaAs(001)-(2×4) surface reconstructions. From ref. [36]

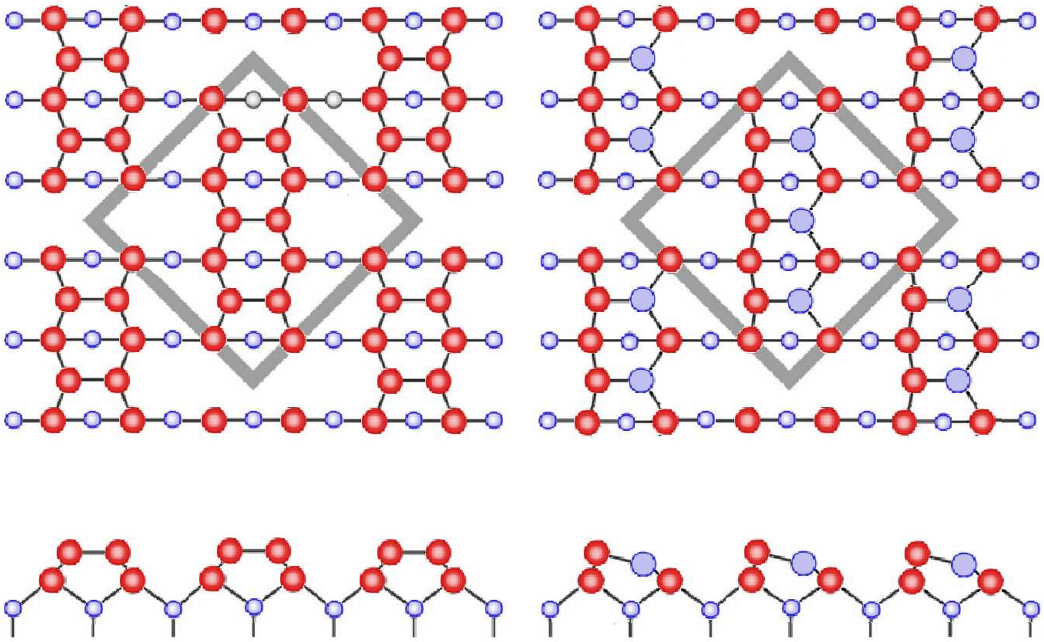

Figure 3.3: three As dimer (α) and three Ga-As dimer (β) structure models for As-rich GaAs(001)-$c(4 \times 4)$ surface reconstructions. Red (blue) circles denote As (Ga) atoms. From ref. [36]

3.3) has 14 As atoms on the topmost layer so that As coverage is 1.75 MLs.

Ga-rich surface reconstructions have been less extensively studied as compared with the As-rich reconstructions. Atomic structures of these reconstructions are still far from being completely understood. Ga-rich reconstructions are usually obtained by heating the As-rich reconstructions $c(4 \times 4)$ and (2×4) without As flux. The Ga-rich reconstruction we well encounter in this thesis is the (4×6). As shown in figure 3.4 this surface reconstruction has 2 Ga atoms on the topmost layer, so that the Ga coverage is 0.083 MLs.

For Si(100) both theoretical predictions (e.g. [37]) and direct observation (e.g. [38]) show that the two dangling bonds on the surface from the diamond structure are saturated by the formation of dimers, which consist of paired surface atoms. The formation of dimers decreases the number of dangling bonds thus lowering the surface energy. The observed reconstruction have a 2×1 periodicity. A typical Si(100) or Ge(100) surface is not perfectly flat, but shows several monoatomic or biatomic steps. When a monoatomic step is present, on the two terraces the dimer direction is tilted by 90°. In 1987 Chadi [39] calculated the stability of single and double step configuration for the Si(100) surface. Uhrberg et al. [40] studied the passivation of dual domain 2×1 Si surface with As flux. After the deposition of 1 ML of As at 400° C the surface again showed a two domains 2×1 reconstruction. Energy minimization calculation showed that a stable reconstruction is composed by As-As dimers on the surface of Si.

3.2 Heteroepitaxy of GaAs on Si

The first attempts to integrate GaAs on Si were performed in the early 1980s growing a GaAs film directly on Si by MBE (e.g. [41, 42]). Only by the 1990s all the basic problems

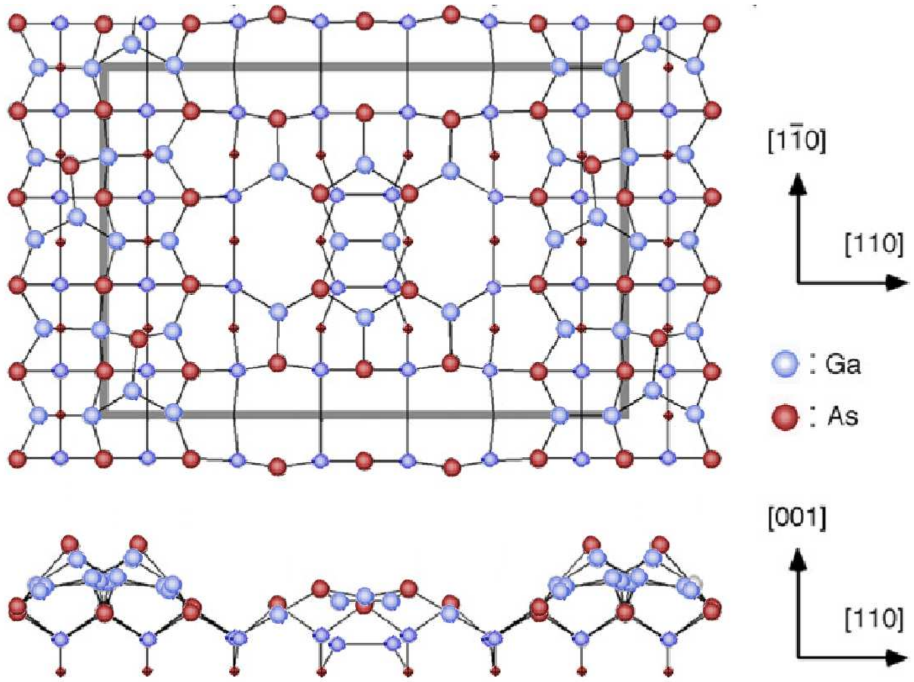

Figure 3.4: structure model for the GaAs(001)-(4×6) surface. From ref. [36]

involved in GaAs epitaxy on Si were identified and reviewed [43]. The first issue is related to the formation of anti-phase domains, due to the growth of a polar semiconductor on a non-polar substrate. Because there are no preferential nucleation site for Ga and As on Si, if the growth of GaAs is started opening simultaneously both beam fluxes, different areas of the Si substrate will be covered by As and Ga, thus resulting in the nucleation of GaAs with two different orientation of the sublattice rotated of $90°$ from one another. Also the preparation of the substrate with an As or a Ga layer is not a sufficient condition to obtain an anti-phase domain free sample. As reported in the previous section, it was theoretically predicted and then confirmed by tunnelling microscopy [37, 38] that on the clean (001) surface of silicon, monoatomic steps are presents. Si atoms on the surface form dimers in such a way that the dimers on one terrace are perpendicular to those of the neighboring one (upper left panel of figure 3.5). Passivating a Si surface with a monolayer of As leads to the formation of As dimers with perpendicular direction on neighboring steps. This model was first proposed in 1987 [39] and the structure of the surface is maintained as the epitaxial growth proceeds. If neighboring Si terraces consist of As dimers perpendicularly directed to each other then the GaAs islands that form on the neighboring terraces will be mutually rotated by $90°$ around the vertical axis. As the islands grow and coalesce, the contacting planes will results in atoms of the same species that give raise to crystal structure defects known as anti-phase defects. The Ga-Ga and As-As bonds breaks the periodicity of the lattice and act as centre of scattering for the carriers and center of non-radiative recombination. The problem was solved by using Si miscut substrates $4-6°$ from the (001) plane. Bringans et al. [44] found that under certain annealing conditions, two-atomic steps form on the silicon (001) vicinal surface and on these terraces Si-Si dimers have an identical orientation (fig. 3.5 upper right panel). For this reason, on the As monolayer deposited before GaAs starts to grow, arsenic dimers also have an identical orientation and GaAs crystallites have the same orientation on either of these two Si surfaces.

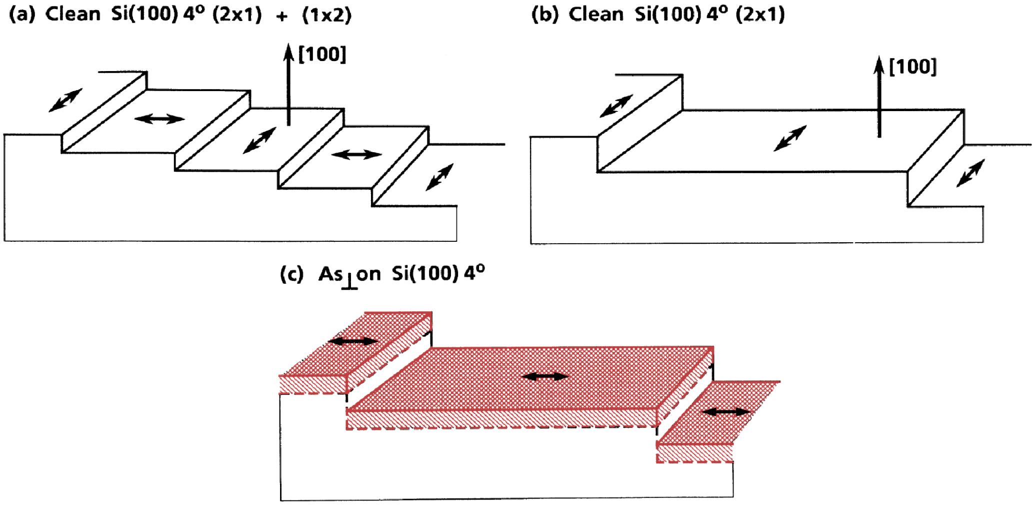

Figure 3.5: direction of dimers on Si(100) surface few degree miscut towards [011] with single steps (a), double steps (b) and with double steps and As passivation (c). From ref. [44]

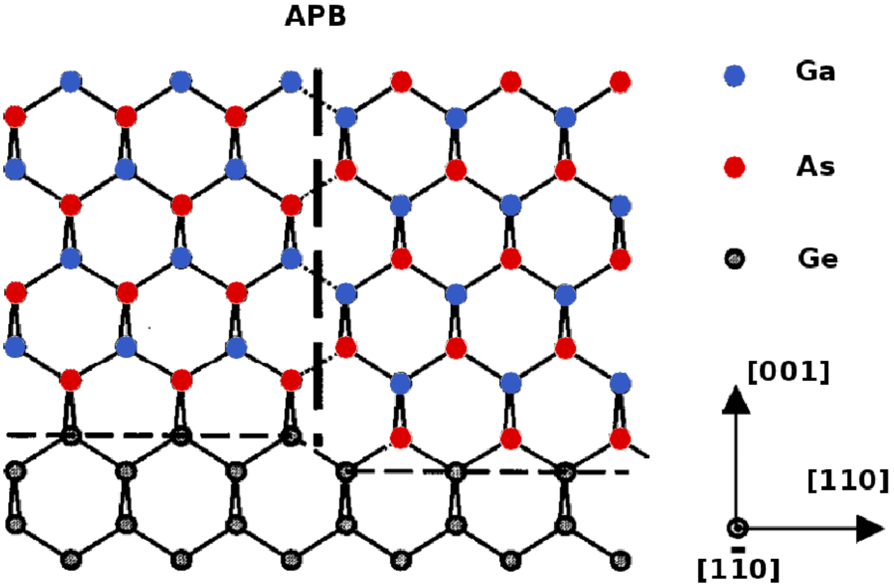

Figure 3.6: anti phase boundary (bold dashed line) nucleated in GaAs by a single atomic-layer step lying on the [001] Si surface. From ref. [45]

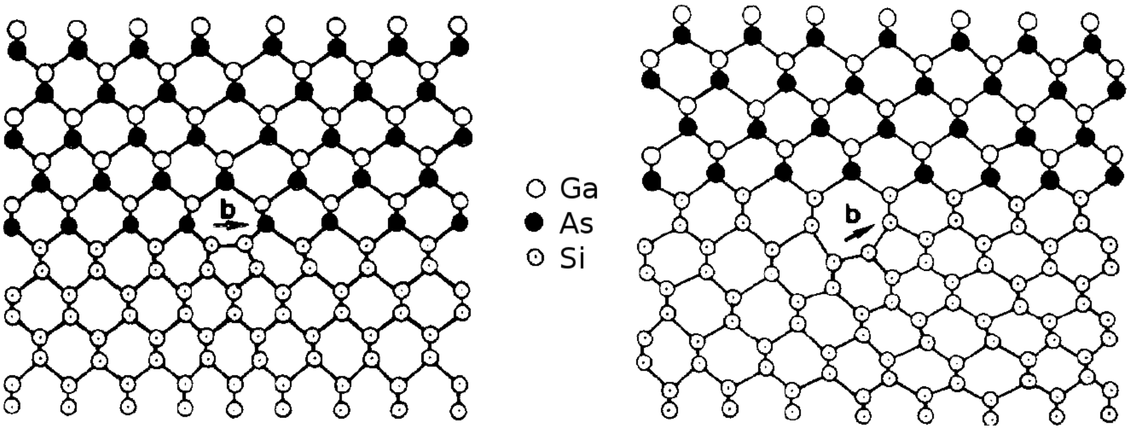

Figure 3.7: the two types of dislocations in zincblende and diamond crystalline semiconductors: type I with Burgers vector parallel to the interface (left panel) and Type II with Burgers vector inclined at an angle to the interface (right panel). From ref. [48]

The second issue is the formation of dislocations in the GaAs layer grown on Si due to the lattice mismatch between GaAs and Si. The lattice parameter of GaAs is $a = 5.653$ Å, for Si is $a = 5.431$ Å, so that the mismatch is about 4%. This mismatch causes strain on the lattice of the epilayer and the energy associated with the strain is proportional to the thickness of the epilayer. If the thickness of the epilayer is small and below a critical value, the mismatch is accommodated by elastic deformation of the lattice, i.e. the GaAs lattice is compressed in the plane of growth and expanded in the plane perpendicular to the plane of growth. When the epilayers become thick [46, 47], the associated strain energy is larger than the misfit dislocation energy, then dislocations are generated to relieve strain energy. Perfect edge dislocations (an extra half-plane of atoms is introduced or removed mid way through the crystal) enable the release of strain energy while inclined dislocations (tipically 60° in the case on GaAs on Si) thread to the surface and degrade the quality of the epilayer creating non-radiative recombination centers and increasing the impurity diffusion along the line of dislocation thread. Si can diffuse from the substrate though the dislocations and causes auto doping in the epilayer [43]. Dislocations are often described in terms of Burgers vectors. In a perfect crystal is always possible to choose a closed path defined by a series of displacements of the Bravais lattice. In a crystal with a defect the same path fails to return to its starting point. The Bravais lattice vector that joins the starting point and the end point is the Burgers vector of the dislocation. The Burgers vector is not dependent on the path chosen. The misfit accommodated by a dislocation is the projection of its Burgers vector onto the substrate plane. The commonly occurring dislocations in zincblende and diamond semiconductors can be classified in two different ways [48]: those whose Burgers vector are parallel to the growth plane (type I dislocations) and others (type II dislocations, see figure 3.7). Type I dislocations are pure edge type, type II dislocations have their Burgers vector at an angle of 45° to the plane of the substrate and 60° to the dislocation line. Type II dislocations can easily move up through the GaAs epilayer and reach the surface. Such a propagation of dislocations from the interface through the epilayer is called threading. Threading dislocations cause impurity diffusion and degradation of optical and electrical properties of epilayers.

Another issue related to lattice mismatch is the nucleation mechanism of GaAs on Si.

From the middle of the 1980s is well known that, in the initial stage of the deposition, GaAs on Si does not form a layer but give raise to islands [49]. In the previous chapter was already outlined the simplified mechanism for the Volmer-Weber growth. In fact, crystalline material coherently adsorbed on a substrate which has a different lattice parameter tries minimize the elastic energy accumulated creating misfit dislocations or with a deformation of the surface called 2D-3D transition [50]. If the misfit is moderate this deformation leads to alternating hills and valleys while for larger misfit the adsorbed film splits into clusters. The energetic advantage is that at the top and on the sides of the islands the adsorbate lattice constant is closer to that of the free adsorbate. The density and the size of the island is controlled through adatom diffusion length by the initial substrate temperature (see e.g. [49, 43]). This is important because the dislocations is most likely to nucleate in the high-stress regions at the edges of big islands near the island-substrate interface [51, 52]. The bigger is the island, the higher is the stress on the external edges and the higher is probability to nucleate a huge number of dislocations. To minimize the density of threading dislocation, GaAs is deposited on Si initially at low temperature to obtain small islands, then annealed and only after these steps a normal temperature GaAs growth (two-step growth) is performed. But also in this case when islands coalesce the rough surface obtained becomes source for defects.

The last issue is the difference in the thermal expansion coefficients, $6.63 \times 10^{-6} K^{-1}$ for GaAs, and $2.3 \times 10^{-6} K^{-1}$ for Si. This difference promotes the nucleation of a great amount of dislocations and of thermal cracks in the GaAs film when the substrate is cooled after the growth or when the sample is heated or cooled.

The formation of anti-phase domains can be easily prevented by using Si substrates with surface few degree miscut from the singular plane (e.g. [53]). Bringans et al. [44] described passivation with As of a Si(100) surface oriented at an angle of 4° from [100] direction toward [011]. Such a surface consists of (100) terraces arranged in a stairway fashion and the step height is usually one atomic layer so that each successive terrace will have its Si-Si dimers direction rotated by 90° as shown in upper left panel of figure 3.5. Annealing such substrate at 1030 °C for few minutes is possible to obtain a surface that has predominantly step height of two atomic layers (upper right panel of figure 3.5). This is due to the lower energy of a double step compared to the sum of the energy of two single step in this configuration. Depending on the substrate temperature, As valve opening time and As flux irradiated, it is possible to obtain a surface coverage mainly composed by As dimers parallel or perpendicular to the steps, but in both cases the GaAs grown will have the same orientation and will not give raise to anti-phase boundaries.

Lattice mismatch and difference in thermal expansion coefficient are more serious problems that can introduce dislocation density as high as $10^9 - 10^{10}$ cm^{-2}. The two-step growth technique, the introduction of thermal cycling or annealing treatment decrease the dislocation density but do not allow to reach a value useful for the fabrication of high optical quality nanostructures.

3.3 Heteroepitaxy of GaAs on Si through a Ge layer

A different approach to solve the issues related to lattice mismatch and thermal expansion coefficients is the fabrication of a buffer layer between Si and GaAs. In the 1980s several studies were made with Ge buffer layer (e.g. [54]). Germanium has a lattice parameter of 5.66 Å, and a thermal expansion coefficient very close to the ones of GaAs. In the 1990s

Fitzgerald and al. [55, 56] studied the growth of a graded GeSi buffer layer on Si subtrate. Because Ge lattice parameter is similar to the one of GaAs, linearly increasing the content of Ge from 0% up to 100% makes the lattice parameter of the buffer layer suitable for the deposition of a GaAs epilayer. The threading dislocation density on such kind of samples was reduced to 2×10^6 cm^{-2}. The preparation of a low threading dislocation density film required slow increase of Ge content (no more than 10% per micron), leading to a large material and time consumption, wafer bowing and layer cracking because of large epilayer thickness. Deposition with high substrate temperature reduced growth time but led to very high roughness on the final Ge surface (up to hundreds of nanometers [56]).

To better understand the possibility to integrate GaAs on Si through a Ge virtual substrate, several experiments were performed to test the quality of a GaAs epilayer directly grown on a Ge substrate. Brammertz at al. [57] studied the quality of GaAs films with different thickness by low-temperature photoluminescence spectroscopy. Several points should be remarked. First of all, also on Ge substrates an anti-phase domain free growth is possible only on miscut substrates. The formation of anti-phase domains on non miscut substrates was confirmed by Nomarski microscope images and improvement of photoluminescence signal of four orders of magnitude from GaAs grown on miscut substrate. For anti-phase domain free samples, measurements showed a band-to-band structure at an energy of ~ 1.5 eV (similarly to GaAs grown on GaAs substrate) and a broad inner band gap structure at an energy of ~ 1.1 eV. For undoped GaAs films with thickness smaller than 200 nm, the band-to-band structure showed a broadening with values of full width half maximum (FWHM) up to 56 meV, which corresponds to high doped layer (estimated to 2×10^{18} cm^{-3}). For thick GaAs layers the band to band structure is separated into two narrow peak due to the split of light-holes and heavy-holes band. This behaviour is related to the strain introduced in the GaAs film by the mismatch between Ge and GaAs lattice parameter. The broad inner band gap structure is in general composed of two gaussian

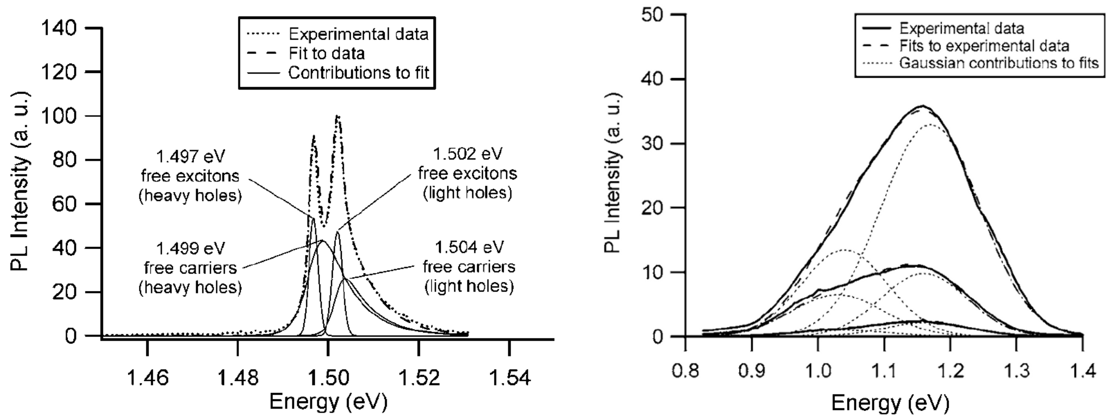

Figure 3.8: left panel: 77 K PL spectrum of a 600 nm thick GaAs film on Ge (dotted line). A fit to the experimental data is shown as well (dashed line). The solid lines show the different components of the fit. Right panel: 77 K spectra of three GaAs films with different thicknesses on Ge substrates (solid lines). The top solid curve is the spectrum of a 140 nm thick film, the middle curve corresponds to a 300 nm thick film, and the bottom curve corresponds to a 600 nm thick film. For every structure a fit to the experimental data is shown (dashed curves) as well as the individual gaussian contributions to the fit with peak positions at 1.04 and 1.17 eV (dotted curves). From ref. [57]

peaks centred around 1.04 and 1.17 eV and with FWHM of about 160 meV. Figure 3.8 shows these structures for three undoped GaAs films with thickness equal to 140, 300, and 600 nm with a fit for every structure that show the individual Gaussian contributions to the structure. The photoluminescence detected is explained with deep trapping states formed when the GaAs is heavily doped at levels in excess of 5×10^{18} cm^{-3}. At this high doping level the GaAs reaches a compensation regime so that additional Ge atoms, instead of replacing Ga atoms in the GaAs lattice as donors, start to occupy the position of the As atoms as acceptors. This behaviour was observed in GaAs heavily doped with Si [58, 59]. When the compensation regime is reached, the doping density stabilizes, because of the mutual elimination of the effects of Si or Ge atoms replacing Ga atoms (Si$_{Ga}$ or Ge$_{Ga}$) and Si or Ge atoms occupying the As positions (Si$_{As}$ or Ge$_{As}$) in the GaAs lattice. Also if the exact nature of the deep trapping states is not generally accepted, there is a prevailing consensus that the lower energy peak is related to the Si$_{Ga}$ – Si$_{As}$ complex whereas the higher energy peak is related to the Si$_{Ga}$ – V$_{Ga}$ complex, where V$_{Ga}$ is a Ga-vacancy site. The same mechanism is reported in [57] for Ge atoms to attribute the 1.04 and 1.17 eV peaks.

Sieg et al. [60] grew GaAs on a Ge substrate and by using an initial low temperature (350° C) deposition reduced the diffusion of Ge and thus the concentration of Ge in the epilayer to less than 2×10^{15} cm^{-3}. To maintain a high GaAs crystal quality at such a low growth temperature, deposition by migration enhanced epitaxy was performed [61]. This technique consists in alternate supplying of Ga and As and allows to grow high quality GaAs films also at low temperature. Ting et al. [45] studied the formation of a single domain GaAs film on pure Ge substrates or on SiGe virtual substrates. In particular they investigated the role of the substrate pre-growth annealing on the formation of a single domain film and the role of the temperature during the first As irradiation in the sub-lattice orientation of GaAs film. The condition to obtain a single domain epilayer is an annealing at T$> 600°$ C. This behavior is explained with the energy required for the formation of double steps on Ge. The subsequent substrate temperature set before As irradiation select the orientation of As dimers on the surface (parallel or perpendicular to the steps) and then the orientation of the GaAs sub-lattice.

In the 1990s Fitzgerald and al. [55, 56] studied the growth of a graded GeSi buffer layer on Si substrate. Because Ge lattice parameter is similar to the one of GaAs, linearly increasing the content of Ge from 0% up to 100% makes the lattice parameter of the buffer layer suitable for the deposition of a GaAs epilayer. As already reported, the threading dislocation density on such kind of epilayer was reduced to 2×10^6 cm^{-2} but at cost of large material and time consumption, and very high roughness on the final Ge surface.

A different technique for growing graded buffer layers of GeSi on Si substrates is low-energy plasma-enhanced chemical vapor deposition (LEPECVD) of Si, Ge, and GeSi [62, 63]. The Chemical Vapor Deposition is a chemical process used to produce thin films with high-purity. The substrate is exposed to one or more gaseous precursors which react on the substrate surface to produce the desired epilayer. The Plasma enhancement is an effective way to increase the growth rates for Si and Ge growth, generating highly reactive neutral radicals and energetic ions which reach the substrate surface greatly enhancing the adatom surface mobilities and the H-removal rate from the surface. In a LEPECVD camera (figure 3.9) the discharge gas (Ar) is fed directly into the plasma source where a Ta filament is heated by a current of typically 120 A. The vacuum is provided by a turbo-molecular pump connected to the growth chamber by an orifice of ~ 1 cm in diameter. The plasma is sustained by applying a voltage of 20-30 V between the grounded chamber

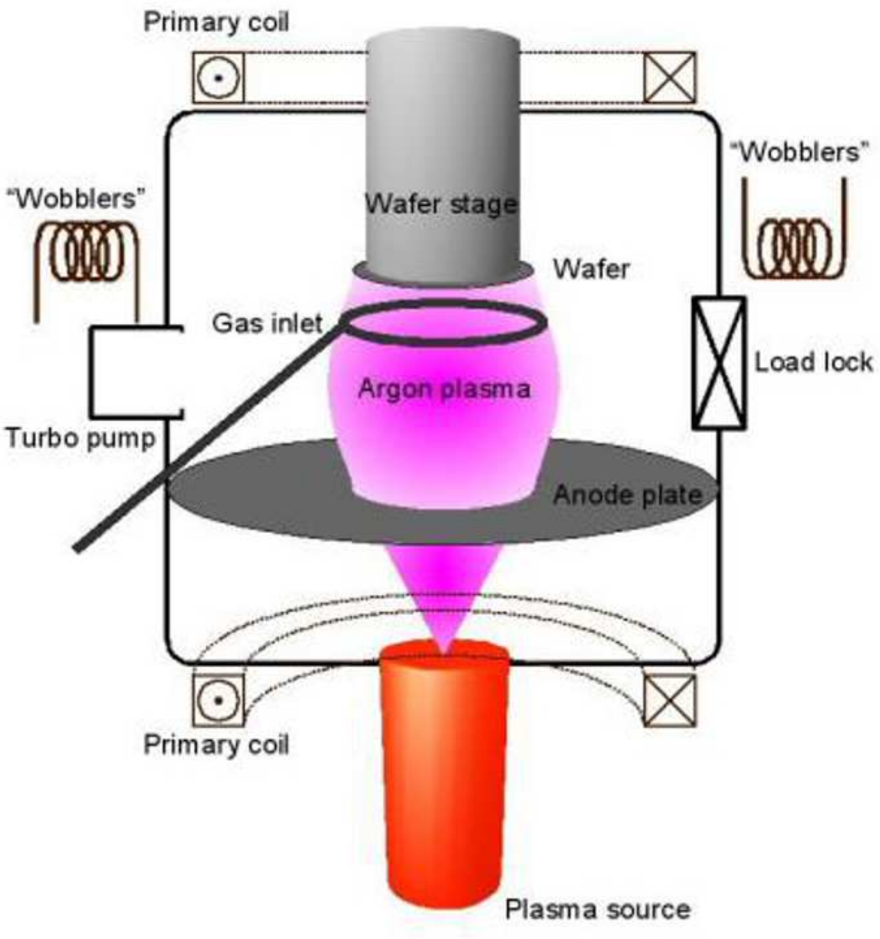

Figure 3.9: schematics for a Low-Energy Plasma-Enhanced Chemical Vapour Deposition camera.

walls and the hot filament. A better control is achieved by a magnetic field, induced by a combination of coils and permanent magnets, by means of which the glowing part of the plasma can be deflected away from the substrate or fully concentrated onto the substrate. The reactive gases, SiH_4, GeH_4 are fed into the chamber by means of a gas dispersal ring placed 5 cm below the substrate. This technique allows the use of a high growth rate (up to 10 nm/s) and low growth temperatures (about 550° C). The density of threading dislocation in Ge/Si films was lowered to 1×10^5 cm^{-2} [64, 65] and the surface roughness reduced to few nanometers [66].

By means of LEPECVD, is possible to deposit pure Ge directly on Si surface without any intermediate SiGe layer. Isella et al. [67, 68] grew 2 μm Ge layer on Si, and performing a post-growth annealing has proved to reduce threading dislocation density [69] to 2×10^{-7} cm^{-2} also using few annealing cycles at low temperatures in order to meet the thermal budget requirements for back-end CMOS technology [70], how is possible to see in figure 3.10.

Colombo et al. [71, 72] studied the quality and the formation of thermal cracks on a GaAs layer deposited on a Ge virtual substrate. The thickness of the GaAs epilayer (2.2μm) is greater than critical thickness (0.24μm) so that the sample was considered fully relaxed at the growth temperature. The low temperature photoluminescence measurements showed a

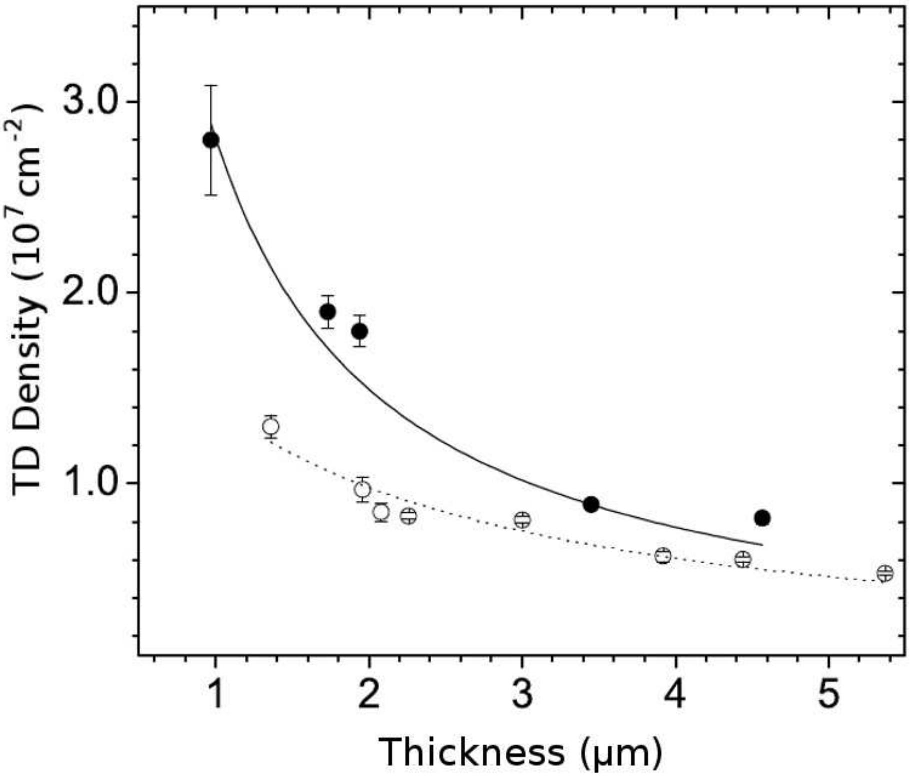

Figure 3.10: threading dislocation density as a function of film thickness for a series of Ge layers deposited on Si at 500 °C and then annealed three times between 600 and 780 °C. Full (open) circles refer to well-oriented (misoriented) layers.

split of the degenerate valence band and a shift toward lower energy of the energy gap due to biaxial strain. The origin of the strain is attributed to the difference in thermal expansion coefficient of GaAs/Ge with Si substrate during the cooling in the growth chamber. Also at room temperature images of the GaAs epilayer obtained via optical microscope showed a crack density of 4 ± 1 mm^{-1}. After several thermal cycles at low temperature the value increased to 12 ± 1 mm^{-1}. Measurements of μ-photoluminescence showed that the position of the main GaAs peak is changing with the distance to the crack. Only near the intersection between two cracks the structure showed a fully relaxed GaAs peak position.

Chapter 4

Experimental setup

4.1 The Gen II MBE system

In this work of thesis a Veeco Gen II MBE machine installed in LNESS laboratory in Como was used. The equipment is composed by three chambers separated by gate valves. The first is an introduction chamber which is possible to open inside a class 100 flow-box. Here the substrates are mounted on special molybdenum blocks and loaded on a trolley. A heater inside the flow-box allows to solder pieces of substrate on molybdenum blocks using melted indium. A different molybdenum block model allows to mount directly a 3" wafer without using indium. From the introduction chamber is also possible to collect the samples after the growth. The vacuum in this chamber is provided by a rotative pump (primary vacuum) and a Leybold Turbovac 361 turbomolecular pump (ultra-high vacuum) that allows to reach 10^{-9} torr. The pressure inside the chamber is monitored by a Pirani and a cold cathode gauge measurement system. To prevent the contamination of the others chambers from the inserted molybdenum blocks and from the wall of the chamber exposed to atmosphere every time the vacuum is broken, a baking system capable to reach 200 °C is available to be used after every opening.

The second chamber is a buffer chamber where is possible to keep substrates ready for the growth in an ultra high vacuum environment. A degas station is available to heat a single substrate up to 600 °C for thermal treatments or to desorb impurities without introducing contamination in the main growth chamber. The vacuum in this chamber is provided by a Varian Triode VacIon ion pump that allows to reach 10^{-10} torr. The pressure inside the chamber is monitored with a UHV nude Bayard-Alpert gauge connected to a Granville-Phillips 350 measurement system. It is also possible to monitor the composition of the atmosphere of this chamber with a mass spectrometer. The trolley with the molyblocks can be moved from introduction chamber to buffer chamber along a rail and it is possible to mount the molyblocks on the degas station with a special transfer arms.

The third chamber is the main growth chamber. The vacuum in this chamber is provided by three different pumps. A cold head connected with a Helix water cooled 8200 compressor is able to reach 10 K and works as a cryogenic pump. A second system is composed by a titanium sublimation and Varian Triode VacIon ion pumps. The combination of these pumps allows to reach 10^{-10} Torr. The pressure inside the chamber is monitored with two different UHV nude Bayard-Alpert gauge connected to a Granville-Phillips 350 measurement system. The first is used to monitor the background pressure, the second can be rotated in the growth position to measure the equivalent pressure of the atomic or molecular beam incoming from the effusion cells. The beam equivalent pressure can be used to

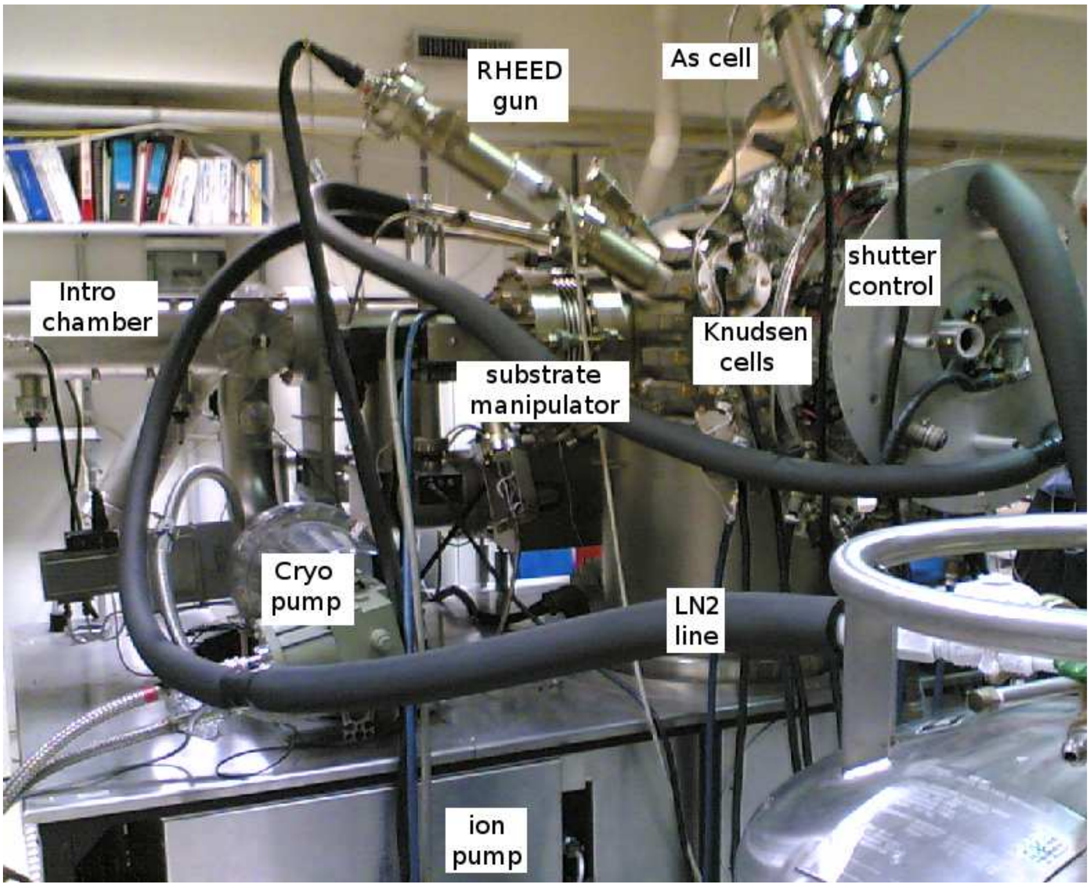

Figure 4.1: MBE Gen II in LNESS laboratory in Como.

calculate the number of atoms or molecules impinging on the substrate. The Gen II MBE system is able to mount up to eight effusion cells arranged radially in front of the substrate holder. Eurotherm 900 EPC controllers (one for each cell) are connected to effusion cell. The controller read the temperature of each crucible with a thermocouple and regulates the voltage and the current necessary to reach and stabilize the temperature selected for the crucible with a power supply. Three effusion cells (the ones for elemental Al, In and Ga) have two separate heating system and thermocouples to carefully control the temperature of the source material in the crucible and of the mouth of the cell to avoid accumulation of material at the mouth of the crucible and to improve the homogeneity of the beam. Other two cells have single filament and are used to provide dopant (Si or Be) during the growth. The last cell is a valved cracker cell for As. The valved cell allows to finely tune the As flux by a needle valve. The Eurotherm 900 EPC temperature control system allows to set a temperature for the bulk zone, which controls As pressure inside the cell, and the cracking zone, that select the arrival on the substrate of As_2 or As_4 molecules. Each cell is provided with a pneumatic shutter to stop or open suddenly the flux. The temperature of the substrate is controlled with a heating system and monitored by a thermocouple also connected with a Eurotherm 900 EPC controller. A optical pyrometer mounted in front of the growth position allow to finely control the substrate temperature. It is also possible to set a rotation speed of the substrate to improve the homogeneity of the deposited film. Inside the main chamber are present three cryo-shrouds which can be filled with liquid nitrogen to improve the vacuum and reduce the contamination of the growth films. The main chamber is also provided with a Staib reflection high energy electron diffraction (RHEED) composed by a electron gun with a maximal voltage of 15 keV and a RHEED fluorescent screen with a CCD camera to acquire the RHEED pattern changes in real time during the growth.

The growth and the buffer chamber are bakeable up to 200 °C mounting special bake shields and it is possible to monitor the baking temperature with six different thermocouples.

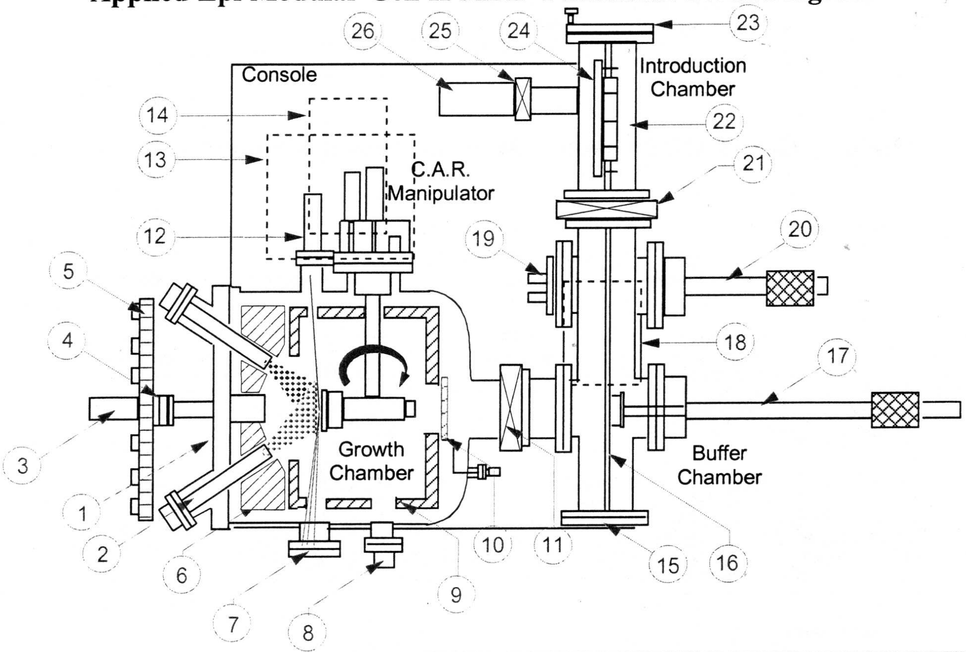
Applied-Epi Modular Gen II MBE Functional Block Diagram

ITEM #	DESCRIPTION	ITEM #	DESCRIPTION	ITEM #	DESCRIPTION	ITEM #	DESCRIPTION	ITEM #	DESCRIPTION
1	Source Flange	6	Source Cryo-panel	11	Growth/Buff Gate Valve	16	Trolley Rail	21	Intro/Buffer Gate Valve
2	Effusion Furnaces	7	RHEED Screen	12	RHEED Source	17	CAR Transfer Arm	22	Outgas Lamps
3	Pyrometer	8	Quad Mass Analyzer	13	Ion Pump (sump)	18	Buffer Ion Pump	23	Quick-hatch Door
4	Heated Pyrometer Viewport	9	Growth Cryo-panel	14	Cryo-pump (sump)	19	Heated Station (HS)	24	Multiple-sample Trolley
5	Removable Shutter Solenoids	10	Master Shutter	15	Buffer End Viewport	20	HS Transfer Arm	25	Intro Pump Gate Valve
								26	Intro Pump (Turbo/Cryo)

Figure 4.2: functional block diagram of a Gen II MBE machine.

It is possible to monitor the pressure reading in growth and buffer chamber, to monitor and set the effusion cells temperature, the shutter position, the substrate temperature and rotation using a special EPI Molly software installed on a Sun SparkStation connected via serial and GPIB connection to the Gen II machine. The schematics of our Gen II system is reported in figure 4.2.

The source of errors during the growth procedures are mainly related to substrate temperature, opening time of the shutters and beam equivalent pressure of As. This is critic especially during the droplet epitaxy procedure, because the density and size of the nanostructures are related to substrate temperature and amount of deposited Ga, while As flux determines the final shape of the nanostructure. Due to the double control system (thermocouple and pyrometer) is possible to estimate the error on the substrate temperature in about $\pm 5°$C. The error on Ga amount deposited are related to the shutter operations and to the flux calibration. For the first we can estimate an error within 1 second, so that the variation of Ga deposited during droplet epitaxy growth is around ± 0.07 ML. For the

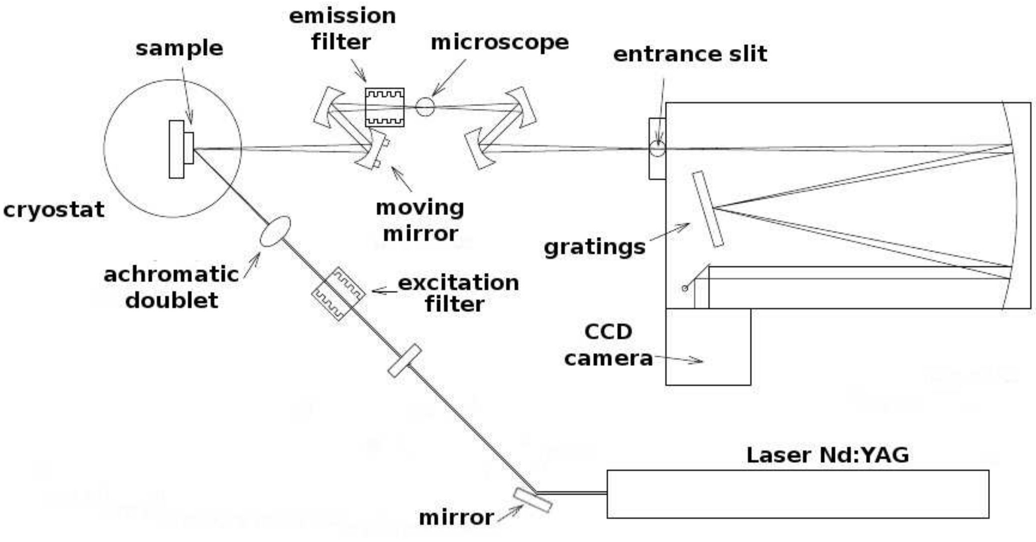

Figure 4.3: schematics of the optical system for the photoluminescence measurements.

calibrated fluxes, the value of the beam equivalent pressure from each cell is controlled every day before the growth, so that the error can only arise from oscillation for long time operation, and can be estimated in about 5%.

4.2 Photoluminescence measurements

The photoluminescence measurements reported in this work of thesis were collected in Dipartimento di Scienza dei Materiali of Università di Milano Bicocca. The photoluminescence was excited with a neodymium doped yttrium aluminium garnet laser with $\lambda_{exc} = 532$ nm ($E_{exc} = 2.33$ eV). The maximal power of the laser is 80 mW. The laser beam was focused with an achromatic doublet with a focal length of 50 mm and strikes on the sample surface with an angle of 45°. The photoluminescence emitted isotropically by the sample, was collected in the normal direction with respect to the sample surface in order to minimize the laser reflected light. Four spherical mirrors focalised the photoluminescence signal collected (about a fraction of 8.8×10^{-4} was collected) to a microscope and to the entrance slit of a monochromator. The microscope allowed to estimate the size of the laser spot. Moving the achromatic doublet and using neutral density filter on excitation side was possible to change the spot size and the excitation power density. The error in the evaluation of the spot size (and so on the exciting power density) can be estimated in about 10%. On emission side a high-pass filter with nominal cutoff wavelength of 665 nm was present to remove the laser light diffused by the sample. The monochromator was a Jarrel-Ash, model 82-025 with focal length 0.5 m, aperture f/8.6 with a diffraction grating with 150 rules/mm, blaze (maximal efficiency) at 0.8 μm and dispersion of 12.8 nm/mm. The entrance slit was kept at 100 μm during the measurements so that the theoretical bandpass for our system is about 1.3 nm.

The signal obtained was focalised on a Andor CCD camera model iDus 401. The camera had a sensor with a matrix of 1024×128 pixels, each pixel a dimension of $26 \times 26 \mu$m. The sensor was cooled by a Peltier system to reduce the number of thermally generated carriers (thermal noise). The measurement range of the CCD camera was between 300 and 1050 nm. The selected range for low temperature measurements was 1.36-2.09 eV. The photoluminescence spectra were acquired in the temperature interval between 13 and 300 K. A cryogenic system Leybold RGD 210 based on Gifford-McMahon cycle was used. To avoid thermal exchange with the external environment and reach low temperature, a vacuum degree of few 10^{-7} was provided inside the cryostat by a rotative and a diffusive pump with a cold trap. A thermal screen was mounted around the sample to prevent thermal irradiation. The pressure inside the cryostat was monitored with Penning gauge. The temperature of the sample was controlled with a SMC TBT model 220 thermo-regulator and monitored with a silicon diode excited with a 10μA current.

4.3 Morphological characterization

Morphological characterization of the samples were performed by an Atomic Force Microscope (AFM), a Scanning Electron Microscope (SEM) and a Transmission Electron Microscope (TEM).

The AFM used for the measurements is a Veeco Innova installed in LNESS laboratory in Como. The microscope is used in tapping mode imaging. Tapping mode imaging is performed by monitoring the oscillation amplitude and phase of an oscillating cantilever probe. The probe to sample distance is set so that the probe tip lightly contacts (“taps”) the sample surface during the cantilever oscillation. As the probe interacts with the surface of a sample, the oscillation amplitude or phase relation to the exciting signal change in response to the interaction. The interaction provides the basis for producing an image of the sample. One advantage of tapping mode AFM is reduction of frictional forces which exert torque on the cantilever. Unlike traditional contact mode which maintains a constant cantilever deflection, the tapping mode feedback loop keeps the cantilever oscillating at a constant amplitude. The tip on the cantilever is oscillated at a frequency near or at the cantilever resonance. A laser beam is reflected off a microfabricated cantilever, onto a mirror, then onto a photodiode. As the cantilever vibrates, the laser spot oscillates across the photodiode and produces an AC voltage. The signal from the photodiode is rectified, then lowpass filtered into a DC voltage measuring the RMS Amplitude. The RMS amplitude is proportional to the amount of cantilever motion. The feedback system compares the RMS amplitude to the setpoint voltage. The two voltages are kept equal by controlling the amplitude of cantilever movement. The sample surface is in close proximity to the cantilever such that the tip touches the surface only at the lowest point of its oscillation. The RMS voltage is reduced to the setpoint voltage by the feedback loop moving the sample nearer to the tip. The sample reduces the cantilever movement until the desired RMS voltage is reached. The oscillation amplitude of the cantilever is held constant by the piezoelectric moving the sample in Z as it is simultaneously translated in X and Y. Engagement in tapping mode requires that the setpoint voltage be smaller than the RMS voltage when the probe to sample distance is large (far from engaged). The tip to sample spacing is reduced until the RMS amplitude is at the setpoint. For large area scan tips with 10 nm resolution were used, for high resolution scan 2 nm resolution tips were mounted.

To obtain the images of real surface of the samples is necessary to consider that the shape, the finite size, and the imperfections of the tip are responsible for nonlinear interaction of the tip with the sample, producing imperfection in the images [73]. Tip-induced distortions are significant whenever the tip radius is comparable to the typical dimension of the sample features to be observed. Overcoming this obstacle requires methods of estimating

Figure 4.4: the scanning electron microscope installed in LNESS laboratory in Como.

the tip geometry and using the estimate to reconstruct the true specimen shape from its measured image. To obtain the detail of the tip structure, blind estimation algorithm can be used [74]. Blind tip estimation algorithm is an extension of the fact that on some surface data we can see images of certain parts of tip directly. The algorithm iterates over all the surface data and at each point tries to refine each tip point according to steepest slope in the direction between concrete tip point and tip apex. The image of the estimated tip can be then used for the reconstruction of the real surface. In the AFM images acquired in this work of thesis were corrected within the program Gwyddion, using the algorithm reported in [74].

The SEM used for the measurements is a FEI XL 30 FEG installed in LNESS laboratory in Como. Four main components combine to produce the images from the sample: an electron gun, a demagnification unit, a scan unit and a detection unit. The electron gun, which is the source emitter, produces electrons within a small spatial volume with a small angular spread and a selectable energy. This beam enters the demagnification unit, consisting of several electromagnetic lenses, and exits to arrive at the specimen surface with a much smaller diameter than that produced by the gun. Electrons striking the specimen react with the atoms of the sample surface and produce three types of signals: X-rays, electrons, and photons. The main detector system picks up the electrons, amplifies them and converts them into electrical voltage. The scan generator signal, fed to the deflection system of the column, moves the beam in a raster pattern over the specimen area. At approximately the same time the monitor for viewing the image is also scanned. The electrical voltage changes as it rasters, which provides serial information of the specimen surface. This signal, modulated by the one from the detection system, produces the image. The images were acquired in planar view to estimate the density and the base size of the nanostructures and with a small tilting angle (tipically $< 10°$) to evaluate the shape and the height of the nanostructures. The resolution of the instrument is 10 nm.

The TEM images were collected in Istituto dei Materiali per l'Elettronica ed il Magnetismo

(IMEM) in Parma. To evaluate the relaxation of GaAs islands on Si substrate high resolution images were collected selecting a diffraction vector to observe the Moiré pattern (i.e., an interference pattern created when two grids are overlaid at an angle, or when they have slightly different mesh sizes). TEM images were also acquired in Energy Filtering mode (EF-TEM). When the electron beam of the TEM reaches the sample, atoms undergoes elastic and inelastic scattering. Elastic scattering gives rise to diffraction pattern according to the Bragg law. Diffraction patterns were acquired to evaluate the crystalline quality of the samples. The inelastically scattered electrons transfered some of their kinetic energy. Some atoms of the sample can be ionized with the emission of electrons from all the shells. Thus, the interaction between electrons and the atoms of the sample produces changes in electron energy and ionization of the sample. The energy lost by the incident electrons depends on the shell structure of the atom hit. Spectroscopy of the energy lost by the primary beam allows to identify the chemical nature of a sample. By setting a window on a specific absorption edge on the spectrum it is possible to get maps of that energy edge, i.e. of the chemical element that has caused that loss of energy. This technique is called Energy Filtering TEM. About the second effect, the equilibrium state of the excited atoms is restored by the usual process of electrons of the outer shells falling down to the inner shells with the emission of high energy photons (in the x-ray spectral region) which are characteristic of each atom and that can be used to identify the atoms of a sample. This technique is called Energy Dispersive Spectroscopy (EDS). Even in this case one can obtain elemental maps in the TEM by appropriate windowing of the EDS spectrum. EDS-TEM and EF-TEM are complementary techniques.

Chapter 5

Growth of GaAs nanostructures on Silicon via Germanium Virtual substrate

The monolithic integration of GaAs nanostructures on Silicon substrates would allow to fabricate III-V specialized devices directly integrated with the nowadays predominant CMOS technology. As described is chapter 3, several trials were made to obtain this result from the beginning of the 1980s. Three main issues were identified: the difference in lattice parameter and in the thermal expansion coefficient between GaAs and Si, and the growth of a polar semiconductor on a non-polar substrate. Only the solution for the last issue is well known in scientific literature, and consists in the growth of GaAs on Si miscut substrates.

In the last decade two effective techniques for the integration of GaAs on Si were explored to override the two remaining issues. The first is the introduction of a virtual substrate, i.e. the growth of a layer able to accommodate the lattice mismatch and the different thermal expansion coefficient. The second is the fabrication of local substrate to minimize the effect of lattice parameter and thermal expansion coefficient differences on a scale of few hundred nanometers. For both research lines we will introduce the droplet epitaxy technique. On virtual substrates to fabricate the optically active GaAs quantum nanostructures, directly on silicon substrate to fabricate tunable GaAs local substrates. As outlined in chapter 2, droplet epitaxy is effective in creating GaAs quantum nanostructures with tunable densities, dimensions, and shapes (e.g. [27]) and is able to maintain a low thermal budget during the growth, being essentially performed at temperatures below 350 °C.

In this chapter the adoption of a Ge virtual substrate will be analysed, in the next chapter the local substrate solution will be explored.

As outlined in chapter 3.3, several experiments demonstrated the efficiency of Ge graded layers to accommodate the lattice parameter and the different thermal expansion coefficient between Si and GaAs. In particular the fabrication of a 2 μm fully relaxed Ge layer on miscut Si substrates by LEPECVD technique proposed by Isella et al. [68] has proved to minimize the three main issues related to GaAs growth on Si, and to solve other three problems related to the fabrication of Ge graded buffer by CVD technique: the low growth speed, the high value of rms for the surface roughness and the high thermal budget needed to obtain a high quality Ge layer with low threading dislocation density.

A last issue to be considered for the integration of III-V devices directly on Si-based CMOS technology, is the compatibility with the low thermal budget required to integrate the nanostructures growth with the CMOS technology. Two different strategies can be adopted. The back-end integration, i.e. when the CMOS circuitry is already realized, or the front-end integration, i.e. when the devices are patterned in the semiconductor but not the metal interconnect layer is created. Keeping the structure at high temperature for long time deteriorates the interconnect layer and reduces the transistor performances. The adoption of thin Ge layer grown by LEPECVD as virtual substrate and of droplet epitaxy technique for the fabrication of GaAs quantum nanostructures allowed us to obtain high quality and high optical efficiency GaAs quantum nanostructures using a thermal budget suitable for the integration with CMOS technology.

5.1 Substrates preparation

5.1.1 Ge Virtual Substrate

The Ge virtual substrates were grown on Si 3" wafer. To prevent anti-phase domain formation in gallium arsenide epilayer, as explained in section 3.2, the orientation of the wafer was (001) miscut $6°$ toward $[110]$ direction. The substrates underwent a RCA cleaning procedure in clean room environment to remove organic contaminants from the wafer surface. Just before the growth the oxide layer on the Si surface was stripped by a 1:10 solution of hydroflouric acid and deionized water to obtain an hydrogen-terminated surface. The wafer was then loaded in the growth chamber of a LEPECVD system were a 2μm Ge layer was deposited at 500 °C. Just after the growth the sample underwent to six in situ ultra-high vacuum thermal annealing cycles between 600 and 780 °C to reduce the threading dislocation density to $\sim 2 \times 10^7$ cm^{-2}. In figure 5.1 the threading dislocation density is reported as a function of film thickness for a series of Ge layers deposited on Si at 500 °C and then annealed three times between 600 and 780 °C. Full circles refer to well-oriented layers, the open circles to misoriented ones.

5.1.2 Growth of Anti-Phase Domain free GaAs

The substrate was then removed from the LEPECVD growth chamber, inserted in a molybdenum 3" adapter and then loaded inside the Gen II MBE system. After a degas at 300 °C in buffer chamber, the substrate was loaded in the growth chamber. The substrate temperature was increased up to 650 °C to desorb the oxide layer formed during the transfer in atmosphere and to allow the transition from single to double steps on Ge surface. The formation of double steps was verified by the RHEED pattern. In the RHEED pattern reported in figure 5.2 the distance corresponding to $2\pi/a$ is 41 pixels, $2\pi/W$ is 8 pixels so that the ratio $a/W = 8/41$. The step height d can be $a/2$ for double step or $a/4$ for single step, the angle α is about 6° from the wafer specifications. From the relation $d = W \sin\alpha$, and estimating an error of 1 pixel on each measurement, the resulting angle we obtain is $\alpha = \arcsin[(1/2)(a/W)]$ so that $\alpha \sim 5.6 \pm 0.7°$ in good agreement with the wafer specification. If the surface presented single steps the result should have been $\alpha \sim 2.8 \pm 0.4°$.

Substrate temperature was then reduced to 580 °C, As flux opened to obtain a beam equivalent pressure of 5×10^{-6} torr to passivate the Ge surface with As dimers. After few seconds the Ga shutter was opened and GaAs deposition started. Figure 5.3 shows the RHEED pattern along $[1\bar{1}0]$ and $[110]$ directions of the Ge surface before passivation (left column), few seconds after starting GaAs deposition and after the growth of about 50 nm

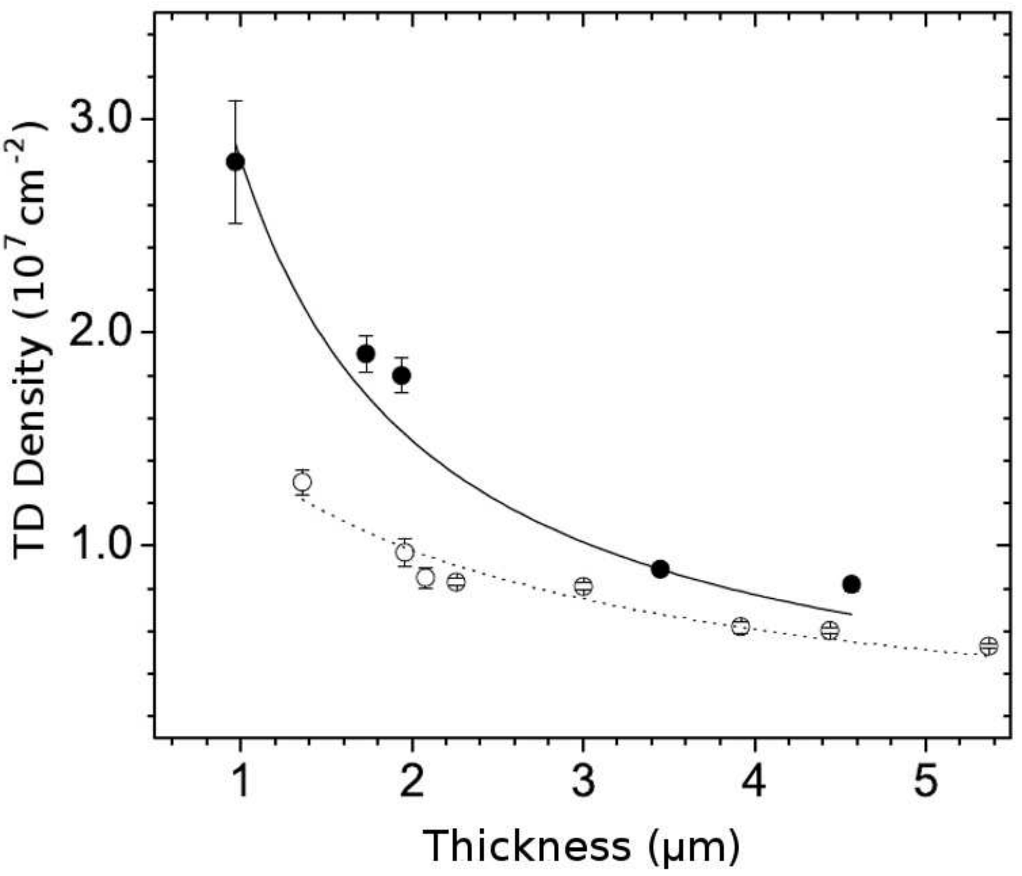

Figure 5.1: threading dislocation density as a function of film thickness for a series of Ge layers deposited on Si at 500 °C and then annealed three times between 600 and 780 °C. Full (open) circles refer to well-oriented (misoriented) layers.

of GaAs (right column). The surface reconstruction at this point is clearly a (2×4), so that we can assert that the growth is almost anti-phase domain free. The confirmation of double step formation and the formation af a (2×4) surface reconstruction are of utter importance, because they allow to ensure the quality of the GaAs epilayer in real time during the growth.

5.2 Quantum dots formation

The formation of a GaAs buffer layer without anti-phase domains is only the first step to obtain GaAs quantum nanostructures integrated on silicon substrate. The formation of a anti-phase domain free GaAs buffer layer on the Ge virtual substrate gives the opportunity to continue the growth exactly as on GaAs substrate with the difference of surface miscut angle and presence of threading dislocations. The fabrication of GaAs quantum nanostructures by droplet epitaxy following the same recipes described in chapter 2 (e.g. [24]) needed to be verified. Also referring to the discussion in chapter 3, several aspects needed to be confirmed: the optical quality of the GaAs layer, the presence of Ge atoms inside the GaAs layer, the possibility to nucleate Ga droplets and GaAs quantum nanostructures on

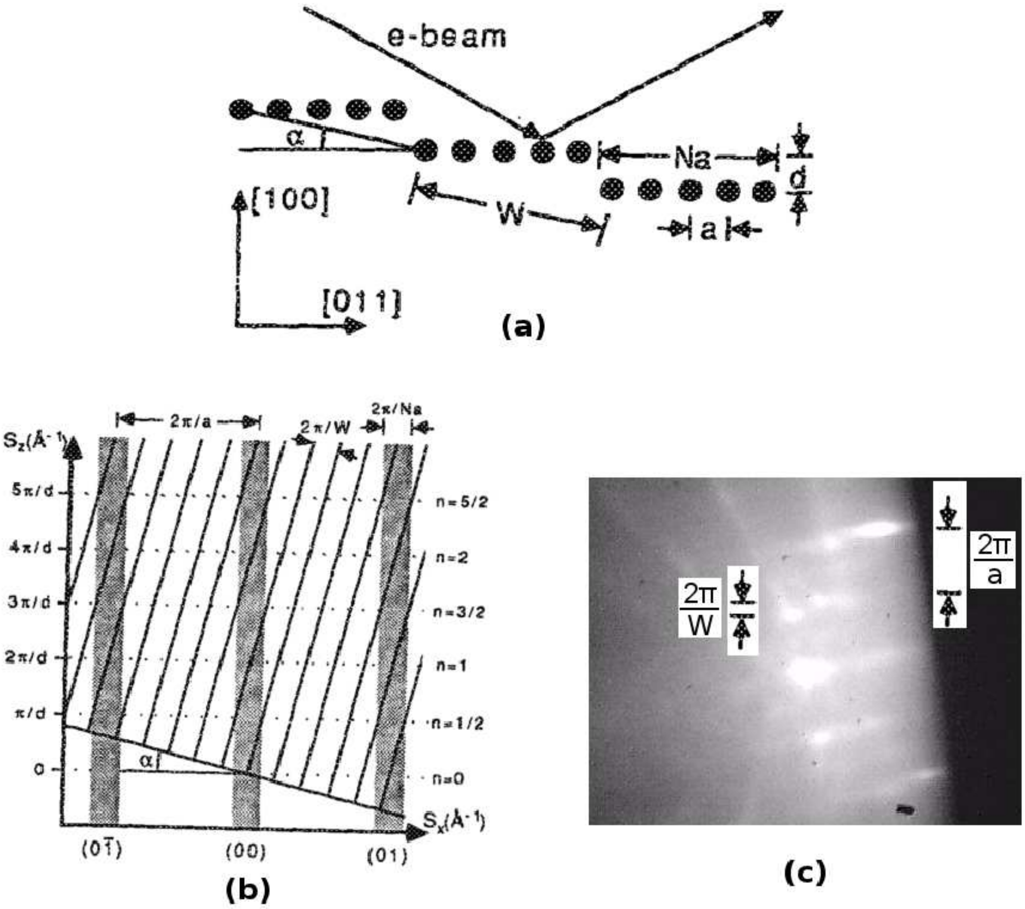

Figure 5.2: schematics of vicinal surface with relevant dimensions (a). Reconstruction of the reciprocal lattice of vicinal surface. The shaded regions represent a single terrace (b). RHEED pattern of Ge buffer surface 6° miscut (c).

the top of the $Al_{0.3}Ga_{0.7}As$ barrier layer also on modified conditions of miscut surface. A set of three samples was prepared for this purpose. On the first Ge virtual substrate a GaAs buffer layer of 1μm was deposited with a rate of about 0.65μm/h at a substrate temperature of 580 °C, then an $Al_{0.3}Ga_{0.7}As$ barrier layer of 150 nm thickness was fabricated. The substrate temperature was decreased to 200 °C and the As valve closed. Surface reconstruction changed from (2×4) to $c(4\times4)$. After temperature stabilization, 3.75 monolayers of Ga were deposited. Substrate temperature was reduced to 150 °C and then an As_4 flux with a beam equivalent pressure of 5×10^{-5} torr was irradiated for 5 minutes. The sample (A1) was analysed with atomic force microscope, and showed (left panel of figure 5.4) the formation of GaAs nanocrystals on the AlGaAs surface with a density of 9.1×10^{9} dots/cm^2 with a mean base size of 44 ± 6 nm and a mean height of 9 ± 2 nm. The profile along $[1\bar{1}0]$ direction is largely compatible with $\{113\}$ family facets (right panel of figure 5.4) while along $[1\bar{1}0]$ direction slope is not so clear. The formation of clear surfaces along $[1\bar{1}0]$ direction is favoured by the geometry of the GaAs lattice, as reported in [21] (see figure 2.3), so that the As absorption sites on (111) surface are more stable than on $(\bar{1}11)$ surface. For this reason As atoms on the (111) surface easily dissolves and the surface is less regular. It is also interesting to see that the size and density of GaAs quantum dots is

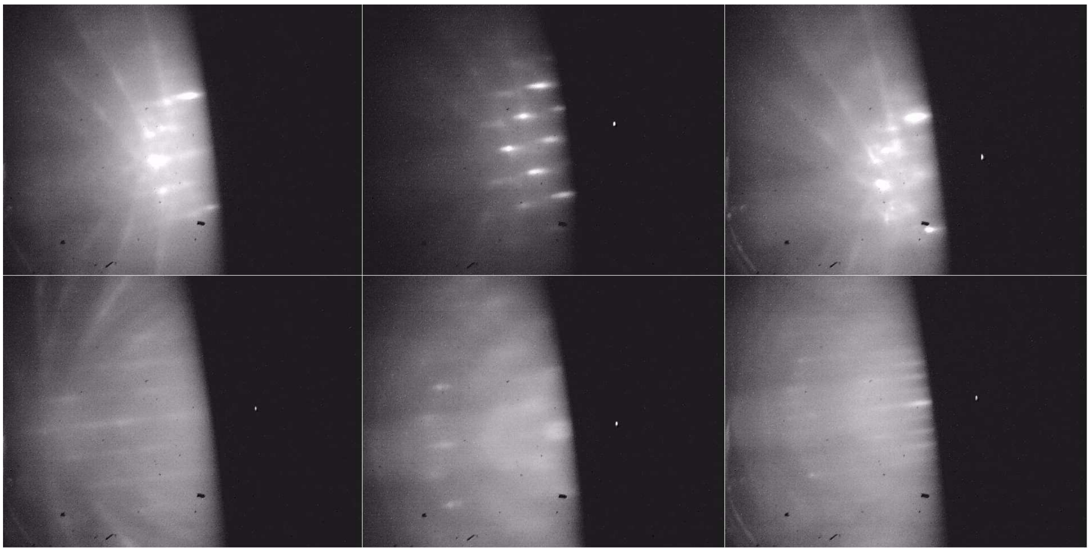

Figure 5.3: RHEED pattern along $[1\bar{1}0]$ direction (upper row) and $[110]$ direction (lower row) of the Ge virtual substrate surface (left column), after opening As and Ga cell shutters (central column) and after few minutes of GaAs growth (right column).

not constant across the surface of the sample, being smaller and with higher density in the substrate valleys. Qualitatively, this behaviour can be explained with the interaction of the gallium droplets with surface steps. In fact, surface steps are preferential nucleation sites for gallium droplets, as shown by Mano et al. [75] on GaAs(110) substrates.

The second sample (A2) was prepared for photoluminescence measurements exactly with the same recipe of sample A1 but the quantum dots were covered with an $\mathrm{Al}_{0.3}\mathrm{Ga}_{0.7}\mathrm{As}$ barrier layer grown partly (~ 30 nm) by Migration Enhanced Epitaxy at 300 °C and partly (~ 120 nm) at 580 °C by MBE. Before removing the sample from the growth chamber, a 30 minutes annealing at 700 °C was performed in As_4 flux. Photoluminescence spectra were measured at 14 K with different excitation power densities. The spectrum of A2 sample showed an intense emission peak at 1.78 eV and is reported in figure 5.5. The photoluminescence band fell in an energy range which was compatible with the emission from GaAs quantum dots grown by droplet epitaxy [31]. In order to attribute this line, electronic structure calculations within the effective mass approximation were performed following the method outlined in chapter 2. In these calculations, the potential for quantum confinement was derived by imposing a cylindrical symmetry to a typical quantum dot profile measured with AFM. The good agreement between the value of 1.78 eV obtained in the PL measurements and the predicted ground state energy $\mathrm{E}_{GS} = 1.75$ eV (inside the broadening due to the quantum dot size dispersion) allowed us to attribute such band to the ensemble emission from quantum dots. The peak observed at 1.94 eV was attributed to radiative recombination inside the AlGaAs barrier, the peaks at 1.49 and 1.45 eV to C and Ge contaminants inside the GaAs layer.

To better understand the origin of the two shoulders around the main peak at 1.78 eV, a third sample (A3) was prepared as a blank following the same recipe of sample A2, but without the deposition of Ga droplets. In this way the sample had exactly the same matrix of the sample A2 but without the GaAs quantum dots. The comparison between samples A2 and A3 showed different common features. The measurements of the two samples

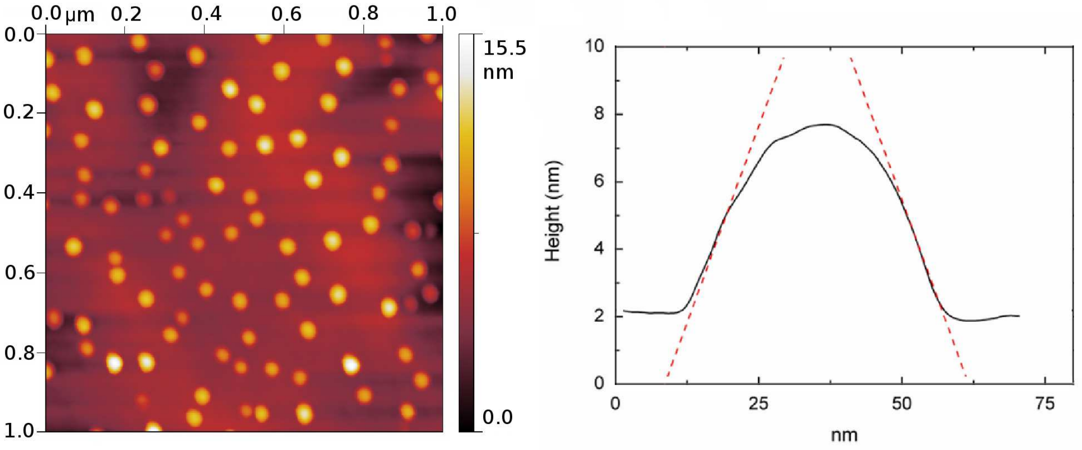

Figure 5.4: AFM image of GaAs quantum dots on sample A1 (left panel). The density is 9.1×10^9 dots/cm^2 and the profile along $[1\bar{1}0]$ direction is mostly compatible with $\{113\}$ facets (dashed red line in right panel).

reported in figure 5.6 were took at the same temperature with similar condition of excitation power density. The GaAs related peaks around 1.5 eV showed the same shape and intensity. The Al$_{0.3}$Ga$_{0.7}$As related peak around 1.9 eV was more intense in the blank sample A3 and was split between bound exciton and donor-acceptor lines. The small shift observed was attributed to small compositional difference in Al content. At 1.86 and 1.69 eV satellite peaks were present in both spectra. The 1.78 eV band in sample A2, related to GaAs quantum dots, is much stronger than any other band observed in the two samples and is present only in the sample A2. Anyway the blank sample A3 showed radiative recombination from states deep inside the Al$_{0.3}$Ga$_{0.7}$As band gap at 1.81 and 1.76 eV. Probably these bands are present also in the A2 sample but overwhelmed by the signal from the GaAs quantum nanostructures.

From the data presented emerges clearly the possibility to fabricate optically active GaAs quantum nanostructures on silicon substrate through a Ge layer. The signal from the dots is at least one order of magnitude stronger than the signals coming from other radiative recombinations. But it is also clear that the region between 1.7 and 1.9 eV is not a good choice for the emission of the nanostructures, due to the presence of several radiative recombination levels inside the Al$_{0.3}$Ga$_{0.7}$As band gap. As already explained in section 3.3, a strong contamination of Ge is expected, and this gives raise to radiative recombination from the impurities in GaAs and AlGaAs layers. The comparison with scientific literature results [29, 76], reports an acceptor binding energy of about 25 meV and 80 meV for carbon and germanium respectively in Al$_{0.3}$Ga$_{0.7}$As. For GaAs epilayers grown on Ge substrate Brammertz et al. [57] attributed some deep level ($\sim$ 300 meV below the gap) to complex defects involving Ge impurities. High density of Ge atoms in GaAs (density $> 10^{18}$ atoms/cm^2) creates the so called "compensation regime" in which part of the Ge atoms, not only replace Ga atoms in the GaAs lattice as donors (Ge$_{Ga}$), but also start to occupy the position of the As atoms as acceptors (Ge$_{As}$). The behaviour is similar to the one known for Si in GaAs and in the scientific literature does exist a prevailing consensus about the attribution of two strong PL peaks to the complex of two Ge atoms acting as donor and acceptor and to the Ge$_{Ga}$ – V$_{Ga}$ complex, where V$_{Ga}$ is a Ga-vacancy site. Considering these data, it is possible to attribute the right shoulder in spectra of samples

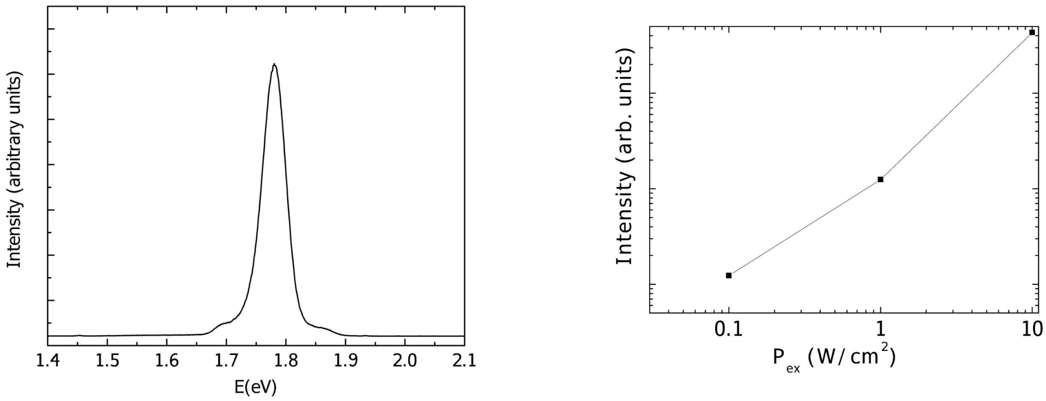

Figure 5.5: In left panel PL measurements at low temperature for A2 sample. Excitation power density is 1 W/cm^2. In right panel intensity of the peak for different excitation density.

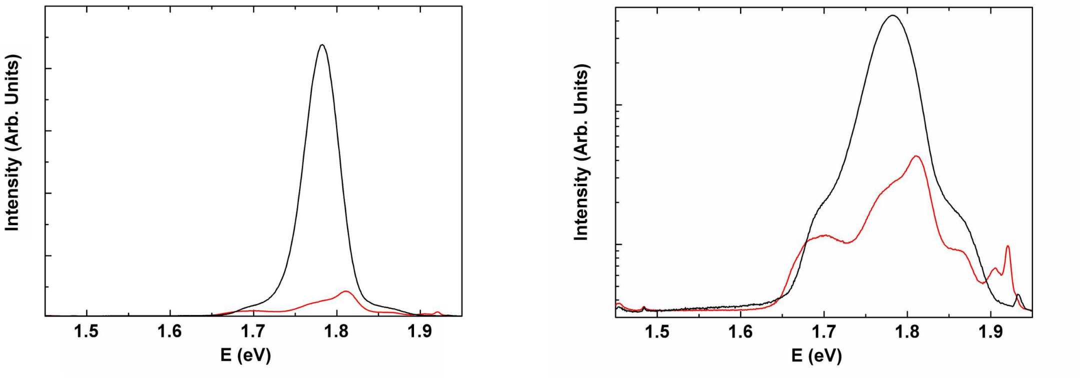

Figure 5.6: PL measurements at low temperature for the A2 sample (black line) and blank sample A3 (red line) grown on Ge virtual substrate. Linear (left panel) and logarithmic (right panel) are reported. Excitation power density is 10 W/cm^2.

A2 and A3 to C acceptor and the peak in spectrum of sample A2 to Ge acceptor. The shoulder at about 1.7 eV can be attributed to deep states due to Ge complexes. We will test these assumptions in the proceeding, with the spectra of other samples.

5.3 Reduction of Ge diffusion

Some experiments were performed to test the possibility to reduce the radiative recombination from defect states in the $Al_{0.3}Ga_{0.7}As$ barrier. To obtain such a result, a stopping layer to limit the diffusion of Ge atoms inside GaAs was deposited between the Ge substrate and the GaAs buffer layer.
Scientific literature reports the possibility to create interfacial layers between Ge and GaAs to reduce the diffusion of Ge atoms inside GaAs epilayer. In the experiment performed by Chia et al. [77] the fabrication of different AlAs layer with thickness up to 30 nm,

limited diffusion of Ge atoms in a GaAs/AlAs/Ge(100) system. The concentration of Ge atoms was measured by secondary ion mass spectrometry measurements and the reduced diffusion of Ge atoms explained with the higher Al-As bonding energy. The experiments showed how the Ge contamination of GaAs layer was largely prevented by the AlAs layer. In our system the experiment was performed introducing in the growth recipe a 30 nm AlAs layer deposited at 580 °C just after the Ge surface passivation with As. After the initial AlAs layer the new sample (B1) was fabricated as a blank following the same recipe used for sample A3 described in the previous section. The RHEED pattern showed a (2×4) surface reconstruction after depositing few tens of nanometer of GaAs, thus confirming the absence of anti-phase domains. The PL measurement performed on the sample B1 at low temperature showed instead no improvements. The emission spectrum was the same observed for sample A3. The different behaviour between our experiment and the one cited was explained with the presence of threading dislocations in our Ge virtual substrate. The AlAs layer is effective to stop the Ge atoms migration inside the GaAs lattice for the higher energy of Al-As bond compared to Ga-As bond. But AlAs layer cannot be expected to effectively reducing diffusion of Ge atoms through the threading dislocations or in decreasing the threading dislocation density. This also means that on Ge virtual substrate the diffusion of Ge atoms inside the GaAs epilayer through threading dislocations is a highly efficient mechanism and that AlAs stopping layer is not effective.

A different approach to improve the quality of the GaAs and AlGaAs layers is the introduction of a thin interfacial GaAs layer grown at low substrate temperature to limit the thermal diffusion of Ge atoms. The method was outlined by Sieg et al. [60, 78] for limiting Ge atoms diffusion on Ge(001) miscut substrate to GaAs epilayer depositing initially 10 monolayers of GaAs by Migration Enhanced Epitaxy (MEE) at 350 °C. A successive study by Tanoto et al. [79] indicated the best choice for substrate temperature to obtain a GaAs flat surface at 250 °C during MEE. As explained by Horikoshi et al. [80] MEE procedure is necessary to deposit a GaAs epilayer at low temperature to obtain high quality and low roughness film. Due to low diffusivity of Ga atoms at substrate temperature < 350°C, the alternate deposition of Ga and As allows a better accommodation of the surface. In our system the experiment was performed introducing in the growth recipe a initial layer of 10 monolayers grown at 250°C. At such a low temperature is necessary to select carefully the amount of Ga and As deposited for each monolayer to prevent the formation of a non stoichiometric compound. Anyway, also in this case the PL measurement performed on this sample B2 at low temperature showed no improvements. Again the difference with the result reported in scientific literature is due to the presence of threading dislocations. The low temperature is expected to allow the creation of an almost Ge free GaAs layer on the top of Ge wafer, but during the successive deposition at 580 °C, the suppression of diffusion through threading dislocation is not efficient. Again, the mechanism is effective for the growth on Ge wafer but is not useful on a Ge virtual substrate where the diffusion is mainly due to threading dislocations.

To confirm the role of the threading dislocations in the Ge atoms diffusion, two experiments were performed. In the first one (sample B3), the grown have took place on a Ge virtual substrate and the AlGaAs layer was deposited at lower temperature (350 °C) to slightly reduce the thermally activated Ge diffusion. For such a low temperature is necessary to deposit a AlGaAs epilayer by MEE to obtain high quality and low roughness film. To reduce the threading dislocation density, the second sample (B4) was fabricated on a SiGe graded buffer deposited on Si(001) substrate miscut 6° toward $[110]$. The buffer layer was grown in LEPECVD growth chamber at 500 °C increasing the Ge content with a rate of 7 %/μm so that the total thickness of the epilayer was $\sim 14\mu$m. The threading dislocation on this substrate was 4×10^6 cm^{-2} as reported by Marchionna et al. [65], so about one order of magnitude below the value measured on the Ge virtual substrate. The growth inside the Gen II machine followed exactly the recipe already described for sample B3. The sample, just removed from the growth chamber, showed a milky surface. This feature was not due to anti-phase domain formation (the RHEED pattern showed a clear (2×4) surface reconstruction during the GaAs epilayer deposition) but to the presence of thermal cracks. This was confirmed by optical microscope. Images showed the presence

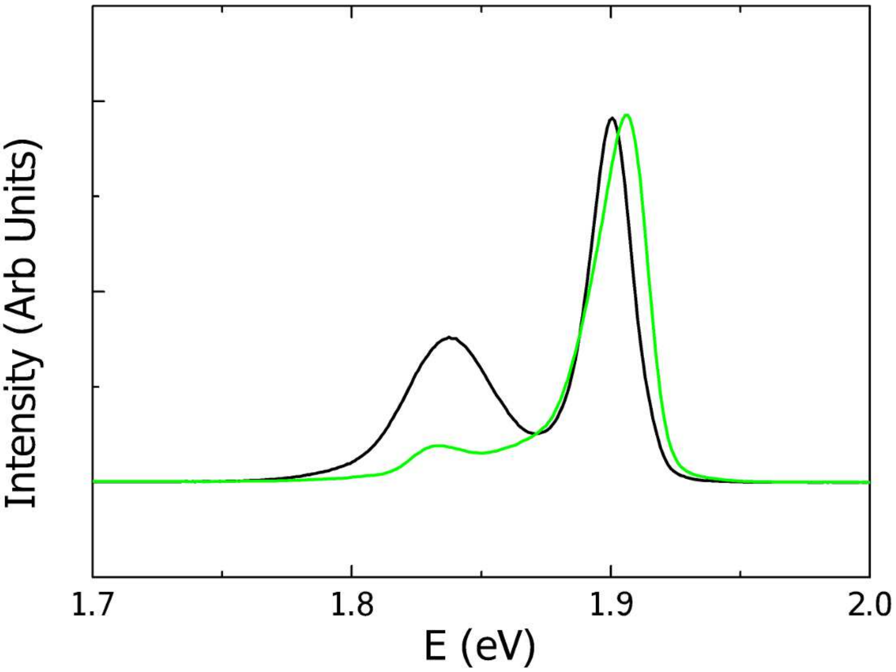

Figure 5.7: PL spectra of samples B3 (green line) and B4 (black line) at 14 K with excitation power density of 6 W/cm^2.

of thermal cracks with a density of 14 ± 3 mm. Such defect are expected to be mainly formed during the temperature reduction between 580 and 350 °C for the optical active layer deposition and during the final temperature depletion from 350 °C to room temperature. The PL measurements performed at 14 K with an excitation power density of 6 W/cm^2 showed a reduced signal from the bands inside the AlGaAs gap (figure 5.7). Now only two main peaks are observed, one at 1.9 eV, attributed to C neutral acceptors in the AlGaAs barrier, and a peak at 1.83 eV, attributed to Ge neutral acceptor in the AlGaAs barrier [29, 76]. The reduction of the peak at 1.83 between the sample B3 and B4 confirmed the relation between the threading dislocation density and the contamination of the optically active region.

5.4 Coupled Ring Disks and Low Thermal Budget growth

It appears clearly from the considerations of the previous section that is not possible to fully prevent the interdiffusion of Ge atoms inside the GaAs and AlGaAs layers. For this reason, the first step to observe a clear emission from the GaAs nanostructures is to select a different emission energy. The region between 1.55 and 1.7 eV is not affected by the radiative recombination due to Ge and C related impurities, and can be reached fabricating nanostructures with weaker quantum confinement. With droplet epitaxy is quite simple to fabricate GaAs nanostructures fitted for this needing. For three different reasons, a useful structure to be used for our purposes is the coupled ring disk [81]. The spectral emission observed for these nanostructures fabricated on GaAs substrate is in the selected region. The potential profile predicted for these nanostructures resembles the one of the dot-in-a-well nanostructures (i.e. each quantum dot is fabricated on a quantum well) and is expected to reduce the threshold when ring disks are embedded in laser diodes structures [82], and to improve the detection mechanism for infrared detectors [83]. Moreover, coupled ring disk grown on GaAs substrate have been reported to be efficient detectors in the infrared region [84]. To approach our goal not only to fabricate GaAs nanostructures integrated on Si, but also to maintain a low thermal budget for the integration with CMOS technology, we have also to notice that coupled ring disk are fabricated keeping the substrate temperature at 350 °C, so that is also possible to fabricate the whole optically active region (AlGaAs barrier layers and quantum nanostructures) at the constant temperature of 350 °C. This temperature is compatible with back-end CMOS technology, and is also expected to slightly reduce the thermally activated diffusion of Ge in the optically active layer.

Following these indications a new recipe was prepared and a second set of samples was fabricated. The temperature of the 2 μm pure Ge virtual substrate was increased up to 650 °C to desorb the oxide layer and to allow the formation of double steps on Ge surface. Substrate temperature was then decreased to 580 °C and a GaAs buffer layer of 1 μm was deposited. Temperature was reduced to 350 °C, observing the change in surface reconstruction to $c(4 \times 4)$. A barrier layer of 80 nm was deposited by MEE and at the same substrate temperature of 350 °C the As valve was closed to prepare a suitable environment for the Ga droplet formation on the AlGaAs surface. Ten monolayers of Ga was deposited. Analysing the intensity change of the RHEED pattern was possible to observe that the surface reconstruction changed from $c(4 \times 4)$ to (4×6) after 1 monolayer of Ga, so that droplets were formed by 9 monolayers. The As_4 flux of 8×10^{-6} torr was irradiated for 20 minutes keeping the same substrate temperature. The first sample (C1) was removed from the growth chamber after this step and analysed by AFM. The produced nanostructures were characterized by a regular, nanometers high, flat disk with a diameter of about three hundreds of nanometers and a hole at the center of ~ 80 nm. The rim of the inner hole is protruded over the disk surface by some nanometers. The density of the nanostructures was 6×10^8 cm^{-2}. The formation mechanism of the coupled ring disk (CRD) nanostructures can be explained with the model outlined in section 2.4 and was analysed in detail in [81]. A second sample (C2) was prepared for photoluminescence measurements exactly with the same recipe of sample C1 but was covered with a 80 nm $Al_{0.3}Ga_{0.7}As$ barrier layer deposited again by MEE keeping the substrate temperature at 350 °C. The whole optically active region of the sample (barrier layers and GaAs nanostructures) was grown at a constant temperature of 350 °C. A last sample (C3) was prepared as a blank following the same recipe of sample C2, but without the deposition of Ga droplets. In this way the

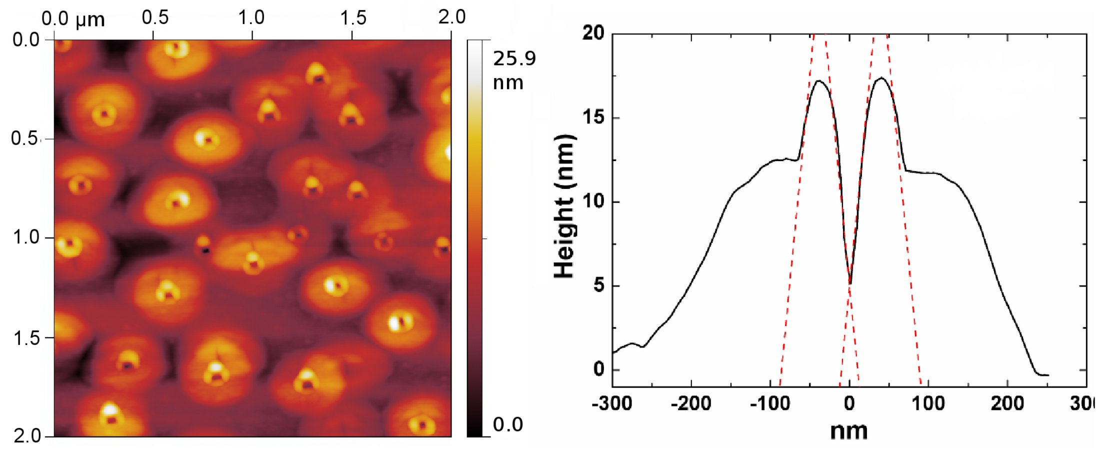

Figure 5.8: AFM image of the surface of sample C1 (upper panel). Profile of a single CRD along $[1\bar{1}0]$ direction (lower panel). Red dashed lines indicates $\{113\}$ planes.

sample had exactly the same matrix of the sample C2 but without the GaAs CRD. Sample C2 was removed from the growth chamber, cutted and some parts underwent a Rapid Thermal Annealing (RTA) step. RTA procedure consisted in a rapid heating (200 °C/min) in nitrogen atmosphere up to selected temperature of 500 °C (sample C2RTA500) or 600 °C (C2RTA600). After 4 minutes the temperature was reduced to room temperature with the same rate. RTA procedure has proved to be as effective as in situ PGA [85], but, due to the reduced annealing time, it allows to maintain a lower thermal budget.

PL spectra for samples C2 and C3 were measured at 14 K with different excitation power densities (see figure 5.9). The two spectra showed sets of similar peaks around 1.9 and 1.5 eV, the former related to radiative transition in the AlGaAs barrier layer (1.89 and 1.83 eV), the latter to GaAs buffer layer (1.50,1.48 and 1.45 eV). PL spectrum of sample C2 also showed an intense peak at 1.53 eV with a satellite peak at 1.56 eV. These radiative transitions were not observed in the C3 sample (blank) and were so attributed to recombination inside CRDs. Comparison between PL spectra reported in figure 5.9 and 5.6 shows that reduced temperature for the growth of the optically active region decreased the PL signal related to Ge atom contamination inside the AlGaAs barrier. The two main peaks at 1.82-1.83 eV and 1.87-1.89 eV can be now attributed to neutral donor to neutral Ge acceptor and neutral donor to neutral carbon acceptor respectively [29, 76]. The deep bands inside the AlGaAs gap disappeared, probably for the lower Ge diffusion. The introduction of different quantum nanostructures also allowed to select an emission region not affected by impurity-related recombinations.

PL spectra measured at 14 K with an excitation power density of 6 W/cm^2 of samples C2, C2RTA500 and C2RTA600 are reported in left panel of figure 5.10. It is interesting to observe that the GaAs related region is unchanged by the annealing procedure. The GaAs layer was growth at high temperature, so that the annealing procedure was expected not to introduce any important modification. The AlGaAs related region was subject to different changes. The peak at 1.89 eV was not modified by the 500 °C annealing step and decreased after the 600 °C annealing step. The peak at 1.83 eV was decreased by the annealing step at 500 °C but greatly enhanced by the annealing step at 600 °C and at least two satellite peaks appeared on the low energy tail. Also the CRD emission band was modified by the annealing treatment: a blue-shift of the emission peak and an enhance-

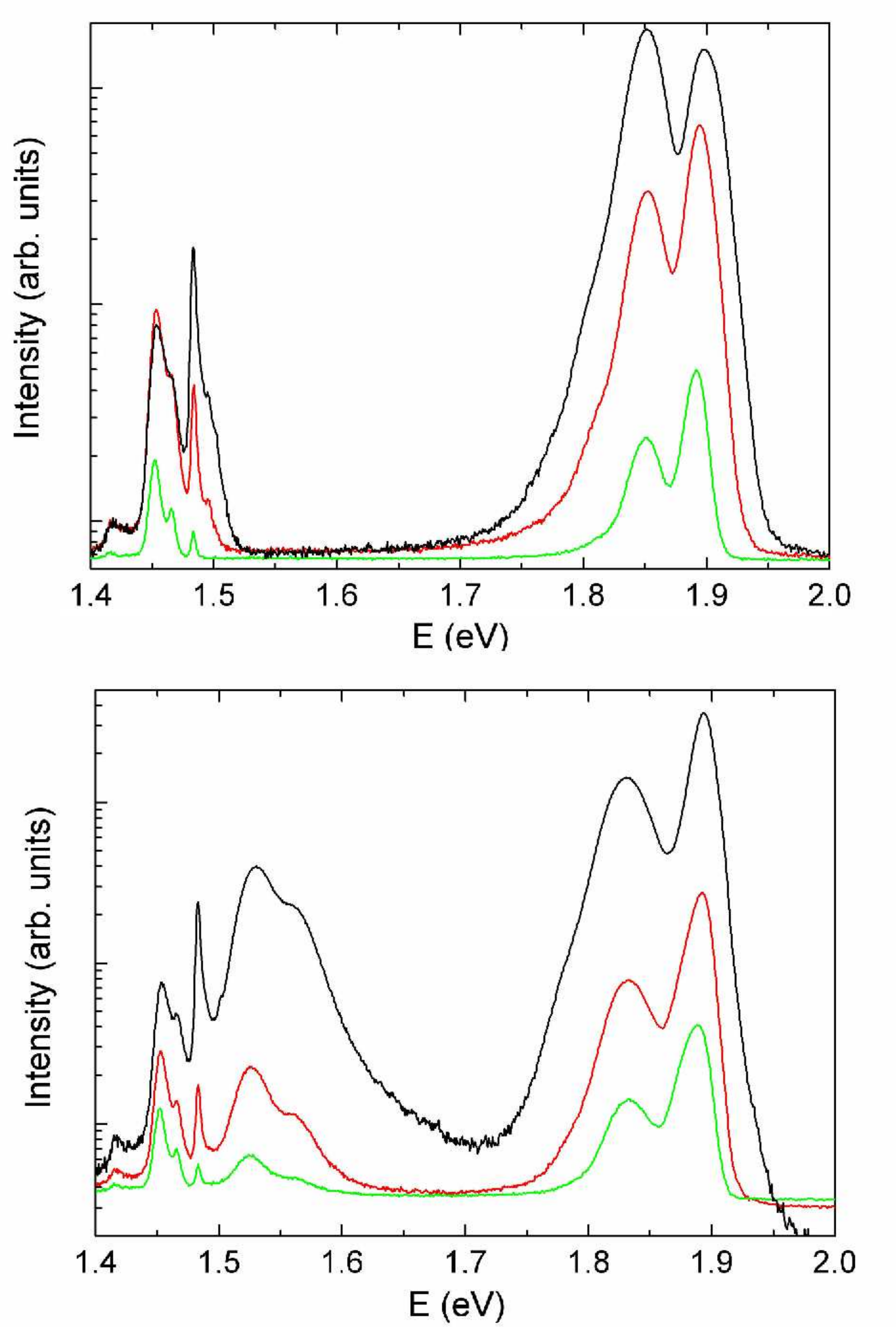

Figure 5.9: PL measurements at low temperature for the C3 sample (upper panel). PL measurements at low temperature for the C2 sample not annealed (lower panel). Power density was 60 (black line), 6 (red line) and 0.6 W/cm^2 (green line).

ment in the integrated intensity was observed (reported in detail in the right panel of figure 5.10). The behaviour outlined can be explained as follows. As already discussed in section 2.5, post growth thermal annealing step is known to improve the poor crystalline quality of the as-grown structure. In fact, the low temperature kept during the growth of the quantum nanostructures fabricated by droplet epitaxy and of the layers grown by MEE introduced a variety of lattice defects, including type III and type V vacancies, interstitials, and defect complexes. On the other hand, in addition to lattice recovery, the RTA treatment induced also two types of interdiffusion. The first was the diffusion of group III species, promoted by any of the lattice defects introduced during the growth and which changes the compositional profile of the nanostructures (see section 2.5 for more details). The second was the diffusion of Ge atoms through the threading dislocations. Considering these effects, is possible to explicate the spectra reported in figure 5.10. The AlGaAs barrier quality was at the same time improved by the diffusion of group III atoms and contaminated by the diffusion of Ge atoms. The AlGaAs barrier quality was surely improved for both the RTA procedures, but the higher temperature used also introduced a strong diffusion of contaminants, resulting in the broad band around 1.8 eV. The CRD band was improved by the RTA treatment as expected. The integrated intensity enhancement and the blue-shift observed are phenomena well known for GaAs quantum nanostructures grown by droplet epitaxy (e.g. [85]).

Following the method outlined in section 2.6 the theoretical emission energy of CRDs (sample C2RTA600) was calculated in the effective mass approximation using as confinement potential the profile of the nanostructures obtained by AFM measurements. The theoretically calculated CRD ground electronic and hole states appeared to be confined in the ring structure, which is formed at the edge of the inner CRD hole. The calculated emission energy well fits the observed PL peak value ($E_{GS} = 1.56$ eV). The CRD excited state was attributed to the quantum well-like state extended along the disk ($E_{EX} = 1.59$ eV). The low confinement energy (~ 30 meV) is due to the relatively large, but still capable of quantum confinement, thickness of the disk. For the calculations the interdiffusion of Al atoms at the CRD interface was taken into account.

The PL spectrum evolution with the temperature of sample C2RTA600 is reported in panel (a) of figure 5.11. As predicted by the Varshni law, the energy gap of semiconductor materials is reduced by increasing temperature, so that also the CRD emission red shifted, as expected, with the increasing temperature. As the temperature was raised, the ratio between the emission from the ground state and the emission from the excited state was decreased. The CRD band was still clearly visible at room temperature where the main contribution was due to the excited state emission. The ratio between the integrated intensity of ground state and excited state, reported in panel (c) of figure 5.11, showed an activation energy of ~ 45 meV, which corresponds to the energy difference between ground and excited state emission. It was possible to attribute the relative increase of excited state emission to a change in equilibrium population of ground and excited states. As the temperature increased, the population ratio of the two states evolved according to the Fermi law. The predominance of disk emission respect to the ring one at RT was related to the different density of states (much higher in the disk case) attributable to the different dimensionality of the two CRD sub-systems (0D for the ring and 2D for disk). The CRD band integrated intensity was reduced by a factor ~ 400 raising temperature from 14 to 293 K. The Arrhenius plot of PL integrated intensity, reported in panel (b) of figure 5.11, shows a clear temperature activated quenching, with a measured activation energy $E_{QUE} \sim 100$ meV. The low quenching energy, much smaller than any energy barrier in

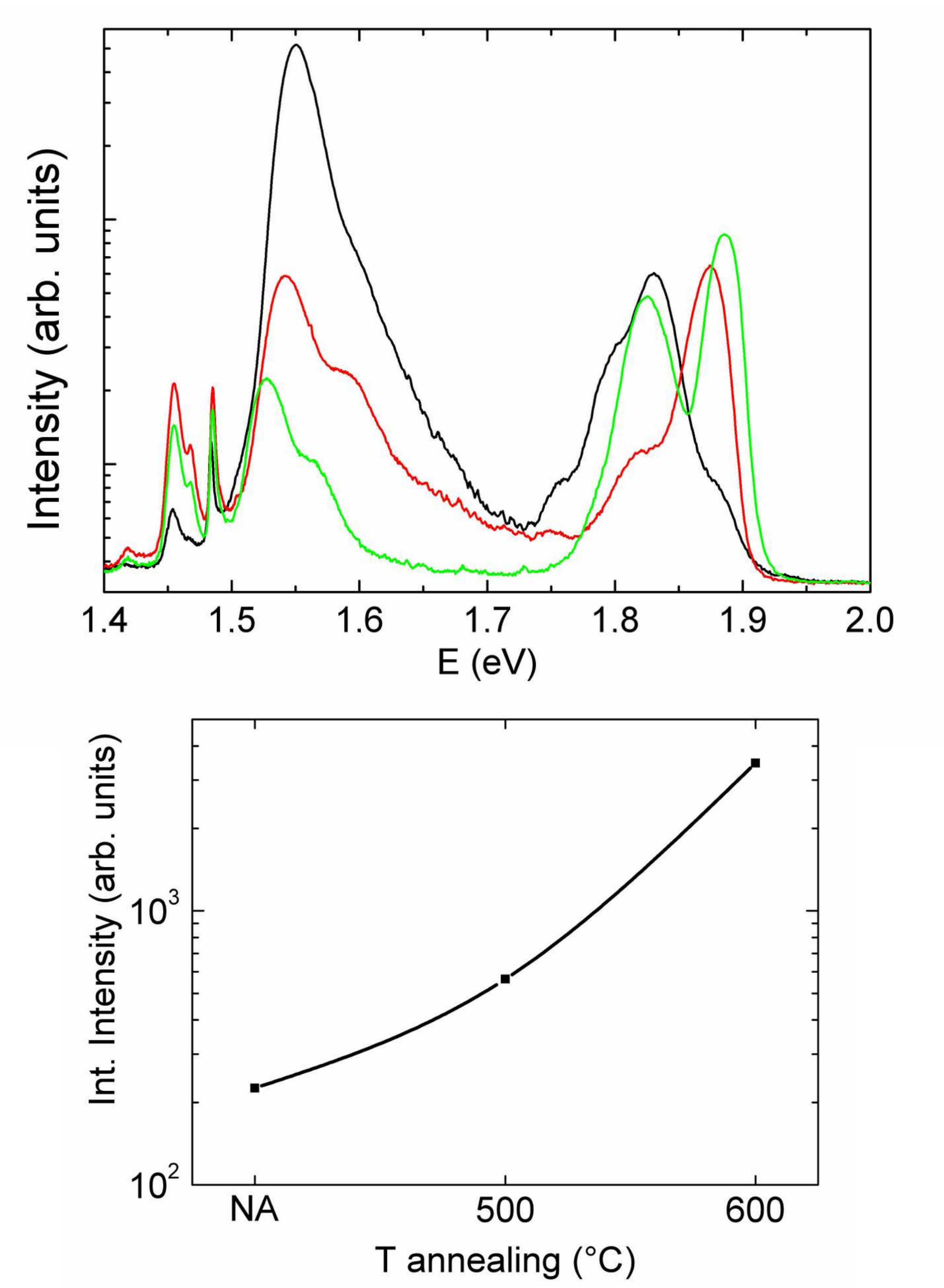

Figure 5.10: PL measurements at low temperature for the samples C2 (green line), C2RTA500 (red line) and C2RTA600 (black line) with excitation power density of 6 W/cm^2 (left panel). Integrated intensity for the CRD emission band versus the annealing temperature (right panel).

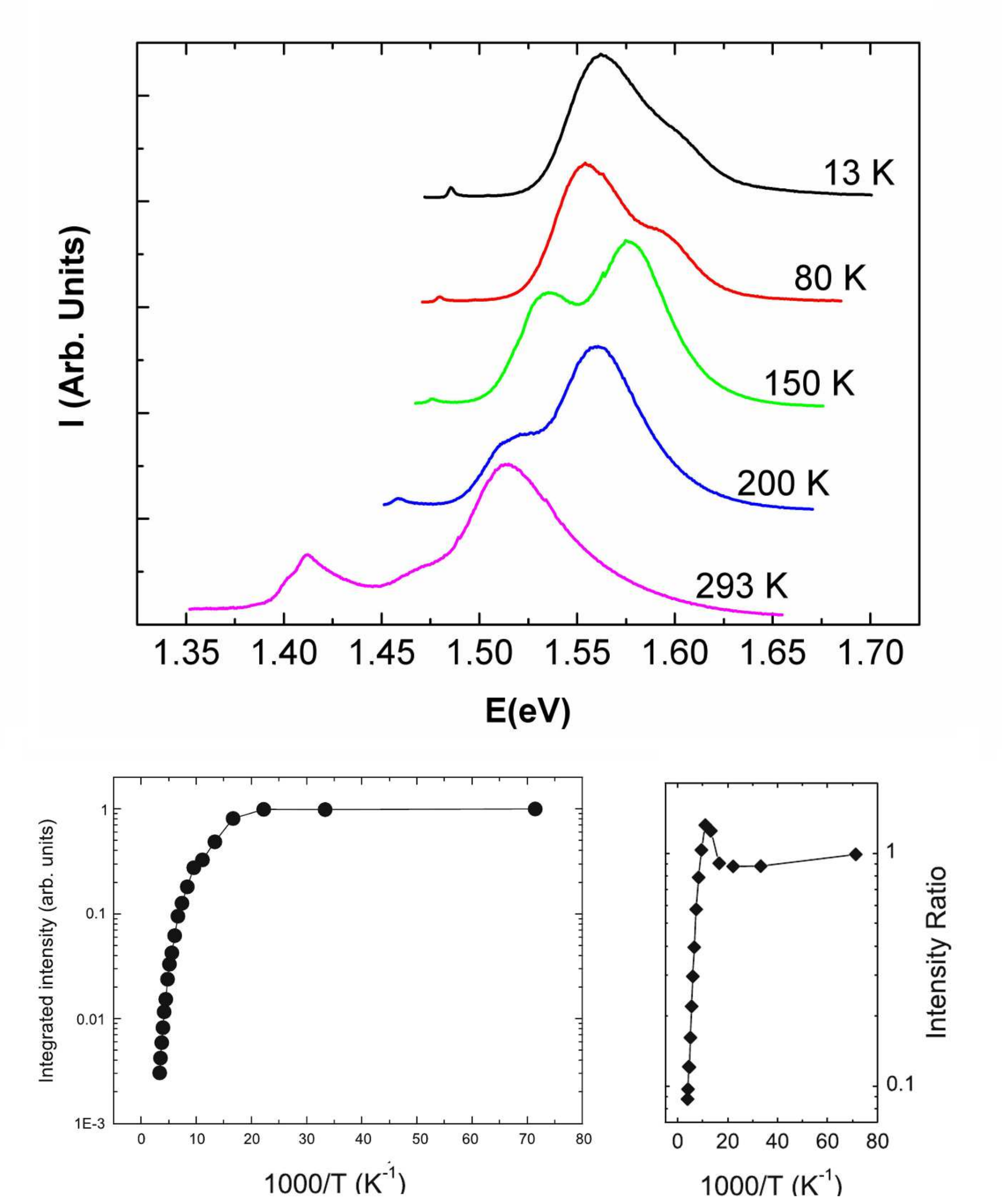

Figure 5.11: (panel a) Normalized PL spectra of CRD band at different temperatures for the sample C2RTA600 with excitation power density of 6 W/cm^2. (Panel b) Arrhenius plot of the integrated intensity of CRD band. (Panel c) Arrhenius plot of the intensity ratio between the ground state emission peak and the excited state.

the CRD system, and the relatively mild reduction in the signal between 14 K and RT, suggested to be attributed to a non-radiative recombination due to defects directly accessible from CRD, or to the quenching active during the carrier diffusion and capture process [85]. Is possible to observe that a high defectivity is expected at the interface between the internal ring of the CRDs structures and the MEE growth barrier layer, due to the unusual ring geometry, which prevents the correct diffusion of adatoms in the inner part of the ring. Finally, to complete the characterization of the fabricated GaAs quantum nanostructures, the ratio η between the number of photogenerated carriers in the GaAs/AlGaAs active layer and the number of photons emitted by the CRDs was calculated. The value obtained for the C2RTA600 sample was $\sim 3 \times 10^{-3}$ at T = 14 K and P$_{exc} = 6$ W/cm^2. This value calculated for GaAs CRDs grown by droplet epitaxy on Si substrate through a Ge virtual substrate well compares with $\sim 1 \times 10^{-2}$ obtained for a standard quantum dot sample (sample D680 of Ref. [32]) grown by droplet epitaxy on a GaAs substrate with a similar nanostructure density ($\rho = 1.2 \times 10^9$ cm^{-2}). The yield η drops to $\sim 8 \times 10^{-6}$ at room temperature due to temperature activated non-radiative recombination channels. While at low temperature η was independent from the excitation power density, at room temperature a clear dependence $\eta \propto P_{exc}^a$ with $a \sim 2$ emerged. Such behavior has been attributed to the saturation of non-radiative recombination channels in the barrier as reported in [86].

5.5 Conclusions

In this chapter the fabrication of high quality GaAs quantum nanostructures on Si with low thermal budget and through Germanium virtual substrate was described. The low thermal budget introduced has a great technological relevance. The final goal in the fabrication of III-V quantum nanostructures on Si substrate is the integration of specialized III-V devices within the existing complementary metal oxide semiconductor (CMOS) technology. In this case, strict constraints on thermal budget for growth and processing of the epilayer are imposed, especially in the case of back-end process, that is, after the CMOS circuitry has been already realized. Fabrication of GaAs nanostructures by droplet epitaxy is intrinsically a low thermal budget procedure, perfectly suited for the realization of growth recipes compatible with back-end integration of III-V nanostructures on CMOS, being performed at temperature of 200-350 °C. Also the temperature of 350 °C set for the fabrication of the barrier layers by MEE is compliant with low thermal budget requirements. The rapid termal annealing temperature used, 600 °C for short period (4 minutes), is reported to be insignificant for the $> 0.25\mu$m CMOS technology back-end integration compatibility [87]. High thermal budget growths were used only for the fabrication of GaAs and Ge buffer layers. About the former, a low temperature deposition such as MEE or modulation MBE techniques [88, 89] are suitable to reduce the thermal budget. About the latter, Ge deposition here adopted is reported to be fully front-end integrable [68]. After this step, integration of Ge virtual substrate into the CMOS process to fabricate selected areas with the required lattice is possible. This makes the whole fabrication process compatible to integration on $> 0.25\mu$m CMOS technology.

Chapter 6

Fabrication of GaAs local substrates on Silicon

As described in the introduction of the previous chapter, a different approach to solve the issues related to the integration of III-V quantum nanostructures on Si substrate is the adoption of local artificial substrates. The concept of local artificial substrate lies in the possibility of fabricating a suitable surface for a subsequent epitaxial growth not on the whole surface of the sample, but locally, using as base some structures fabricated, for example, by self-assembly or by a nano-patterning technique. This approach for the integration of GaAs on Si, decreasing the surface of contact between the two materials to few hundred nanometers, reduces considerably the issues related to lattice mismatch and to thermal coefficient difference. An example of this approach is reported in [90] where the use of nano-patterning allowed to grow GaAs pillars on Si substrate, solving or reducing the issues related to III-V growth on Si.

In this chapter we propose a self-assembling growth procedure based on droplet epitaxy for the fabrication of GaAs islands on Si substrate to be used as local artificial substrates. The adoption of droplet epitaxy allows to self-assembly formation of islands without the presence of a patterning and allows to perform a low thermal budget growth, maintaining the compatibility with CMOS technology. The GaAs islands grown by droplet epitaxy are good candidates to serve as bases for the nucleation of InAs quantum dots atop islands. The nucleation of InAs quantum dots on GaAs island fabricated on patterned GaAs substrate was explored by Wong et al. [91, 92], reporting the possibility to preferentially nucleate InAs quantum dots on specific GaAs island facets. This mechanism can be introduced on GaAs island growth on Si substrates with precise exposed facets to solve the issues related to the integration of III-V quantum nanostructures on Si substrate.

6.1 Experimental procedure

The substrate used for the growths reported in this chapter were Si(001) 3" wafer. The substrates underwent a RCA cleaning procedure in clean room environment to remove organic contaminants from the wafer surface. The first step consisted in dipping inside a solution of deionized water, hydrogen peroxide and ammonium hydroxide (with volumes 5:1:1) at 80 °C for 10 minutes. The wafers were then rinsed in deionized water and dipped inside a second solution of deionized water, hydrogen peroxide and hydrocloric acid (with volumes 5:1:1) at 80 °C for 10 minutes. The wafers were again rinsed in deionized water and finally dried with dry nitrogen. Just before the growth the oxide layer on the Si surface was stripped by a 1:10 solution of hydroflouric acid and deionized water to obtain an hydrogen-terminated surface. The substrate were fixed on special molybdenum holders or cutted in 6 pieces and soldered with pure indium on molybdenum adapter and then loaded inside the Gen II MBE system.

Two different sets of experiments for the creation of GaAs islands on Si substrates by droplet epitaxy were performed: in the first one the amount of Ga supplied was fixed at 3.0 monolayers and the substrate temperature changed, in the second set the substrate temperature was fixed at 350 °C and the amount of supplied Ga changed.

The growth for the first set of samples was performed on pieces of Si substrate cut and soldered with pure indium on molybdenum blocks. After a degas step at 300 °C in buffer chamber, the substrates were loaded in the growth chamber. The substrate temperature was increased up to 780 °C to desorb the hydrogen and expose the Si surface. The RHEED pattern showed a mixed (2×1) and (1×2) surface reconstructions [93]. The substrate temperature was then decreased to Ga deposition value (see second column of table 6.1) and an amount of 3.0 monolayers was deposited. Temperature was further decreased to 150 °C and an As_4 flux with a beam equivalent pressure of 4×10^{-5} torr irradiated for 30 minutes.

Sample	Ga deposition temperature (°C)	Ga amount (MLs)	As irradiation temperature (°C)
A1	250	3.0	150
A2	300	3.0	150
A3	600	3.0	150

Table 6.1: parameters for the growth of the first set of samples

The growth for the second set of samples was performed on 3" wafers fixed on special molybdenum holders. The procedure for the degassing and hydrogen desorption was the same described for the first set of samples. After the hydrogen desorption, the substrate temperature was reduced to 350 °C and the amount of Ga reported in the third column of table 6.1 was supplied. Temperature was further decreased to 150 °C and an As_4 flux with a beam equivalent pressure of 5×10^{-5} torr irradiated for 5 minutes.

Sample	Ga deposition temperature (°C)	Ga amount (MLs)	As irradiation temperature (°C)
B1	350	30.0	150
B2	350	4.0	150
B3	350	0.5	150

Table 6.2: parameters for the growth of the second set of samples

A last sample (C) was fabricated depositing 30 monolayers of Ga at 300 °C on a Si substrate prepared with the same procedure of samples in set A and B. The sample was not irradiated with As_4 flux.

During the Ga deposition, the RHEED pattern turned to halo (left panel in figure 6.1), indicating the Ga droplet formation on the surface. After the irradiation of the substrate with As, the RHEED pattern (right panel in figure 6.1) of samples A1, A2 and B3 turned to spotty, demonstrating the formation of GaAs nanocrystals. On samples A3, B2 and B1

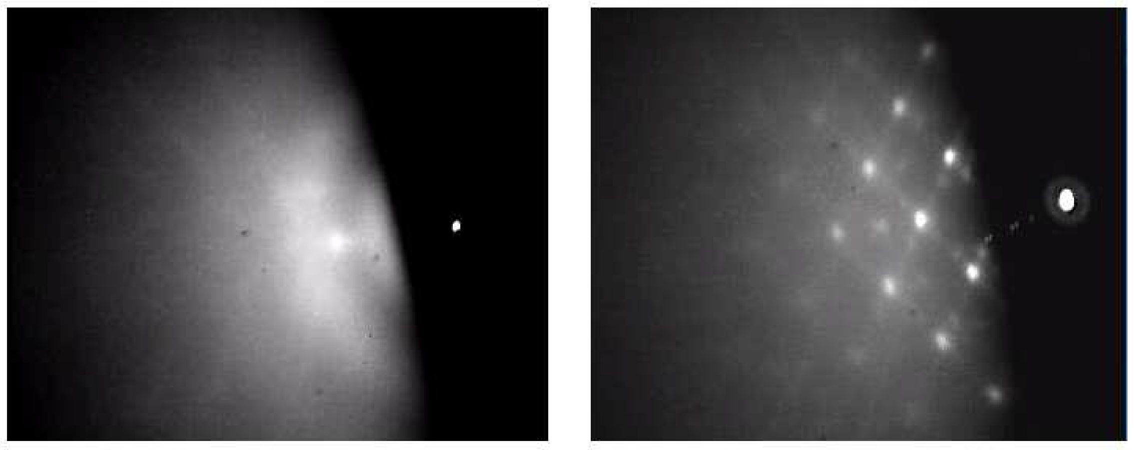

Figure 6.1: RHEED pattern after Ga deposition (left panel) and after As irradiation (right panel) on sample A1.

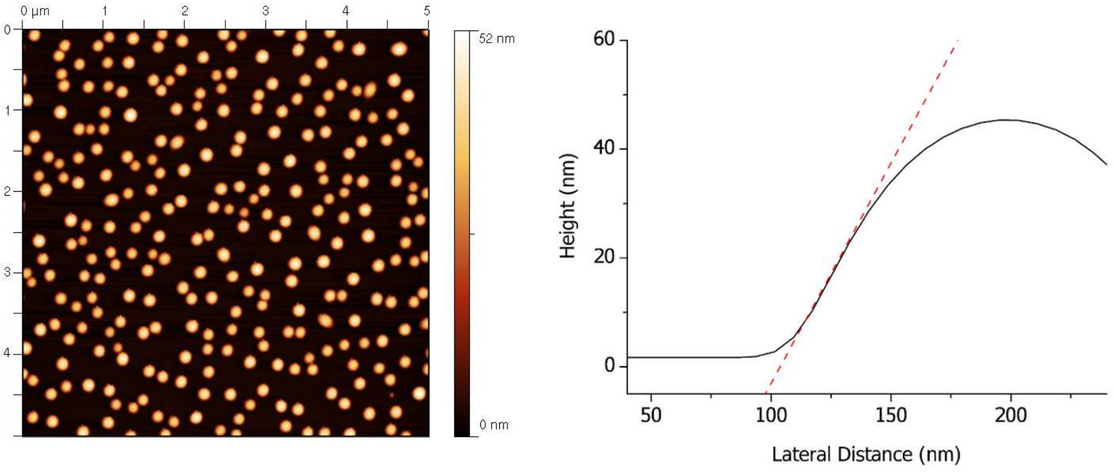

Figure 6.2: AFM 5μm $\times 5\mu$m scan on surfaces of set C samples (left panel) and profile of a single droplet (right panel).

spotty pattern was not observed clearly.
Observation of RHEED intensity during Ga deposition did not evidenced oscillations or other features resembling the formation of a Ga layer on Si surface.

6.2 Characterization of GaAs islands

After the growth, the samples were removed from the growth chamber and analysed by atomic force microscope (AFM), scanning electron microscope (SEM) and transmission electron microscope (TEM). Figure 6.2 shows a 5μm $\times 5\mu$m AFM scan on surface of sample C. The image showed the formation of hemispherical droplets with a density of 8.6×10^8 cm^{-2} and a mean radius of 85.1 ± 5.5. From AFM profiles (see right panel of figure 6.2) a contact angle between the droplets and the Si surface of about 39° was calculated. The angle did not changed depending on the crystallographic direction considered and the size of the droplet. Also the samples of set A and B were characterized by AFM measurements (figure 6.3). The values obtained from these images for the density and for the mean size of the GaAs islands are reported in table 6.2. Several important results emerged from these data. The density of droplets and of GaAs nanostructures for the two samples on which Ga deposition was performed at the same temperature of 300 °C resulted to be the same (8.8×10^8 cm^{-2} on sample A2 and 8.6×10^8 cm^{-2} on sample C). It appeared clearly that each Ga droplet, after the As irradiation at 150 °C, was transformed into a GaAs island. Moreover, the density of the GaAs nanostructures showed a clear dependence on substrate temperature during Ga deposition. The higher was the substrate temperature, the lower was the resulting density of the nanostructures. Arrhenius plot for the density of nanostructures is reported in figure 6.4. The temperature dependence followed a well defined temperature activated law of the form $\rho(T) \propto \exp(E_a/k_BT)$. This behaviour was expected, due to activated processes that control the Ga droplet formation on the growth substrate. The activation energy calculated from figure 6.4 was E$_a = 0.22$ eV. The observed behaviour demonstrates that is possible to control the density of the nanostructures by setting the proper substrate temperature during the Ga deposition. It is also possible to tune the size of GaAs nanostructures formed on the surface by selecting the amount of Ga deposited and using simple geometrical considerations to estimate the mean volume of Ga droplets and of GaAs nanostructures.

Sample	Density (islands/cm^2)	Mean radius (nm)	Mean height (nm)
A1	1.4×10^9	37.2 ± 2.5	24.6 ± 6.3
A2	8.8×10^8	52.0 ± 3.7	44.8 ± 7.5
A3	1.9×10^7	129.8 ± 10.5	126.7 ± 10.4
B1	3.8×10^8	109.4 ± 7.7	103.3 ± 12.7
B2	3.9×10^8	83.2 ± 4.8	71.6 ± 9.5
B3	3.8×10^8	35.1 ± 3.2	22.7 ± 4.2

Table 6.3: density and size of the GaAs island on Si substrate for the six samples.

Figure 6.5 shows the distribution of size and density on the two sets of samples analysed. The error bar reported for size were obtained from the full width at half maximum of the base size histograms of the islands. The GaAs nanostructures base size histograms for all the six samples showed a monomodal Poissonian distribution. The relative standard deviation in size of the samples are all below 10%. In the large islands case (samples B1 and A3) the observed value of 7% nicely approaches the best result obtained by Stranski-Krastanow growth of SiGe islands on a patterned substrates [94]. A slightly larger dispersion is observed for the height of the islands.

6.2.1 Quality of GaAs islands

TEM analysis were performed in collaboration with Dr. Cesare Frigeri of IMEM-CNR in Parma on samples A1, A3 and B1 to estimate the crystalline quality of the GaAs island. The images obtained at low magnification confirmed the density of GaAs nanostructures. Figure 6.6 reports the electron diffraction pattern from a single GaAs island of sample A3. The very weak intensity of one GaAs spot $(\bar{4}00)$ and the slight asymmetry in the spots intensity was due to slight misalignment with respect to the exact (001) zone axis. Inset

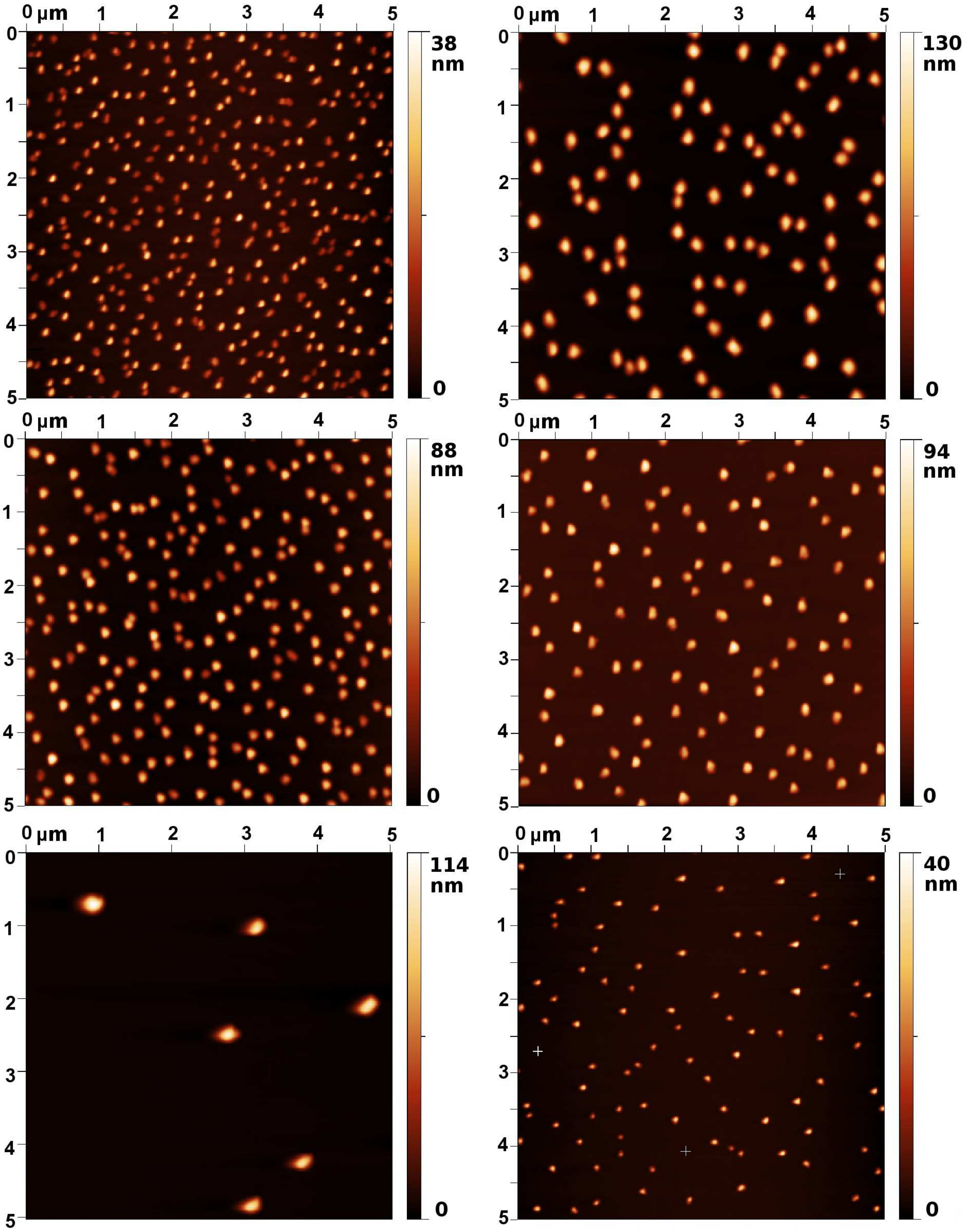

Figure 6.3: AFM 5μm $\times 5\mu$m scan on surfaces of set A samples (left column) and of set B samples (right column).

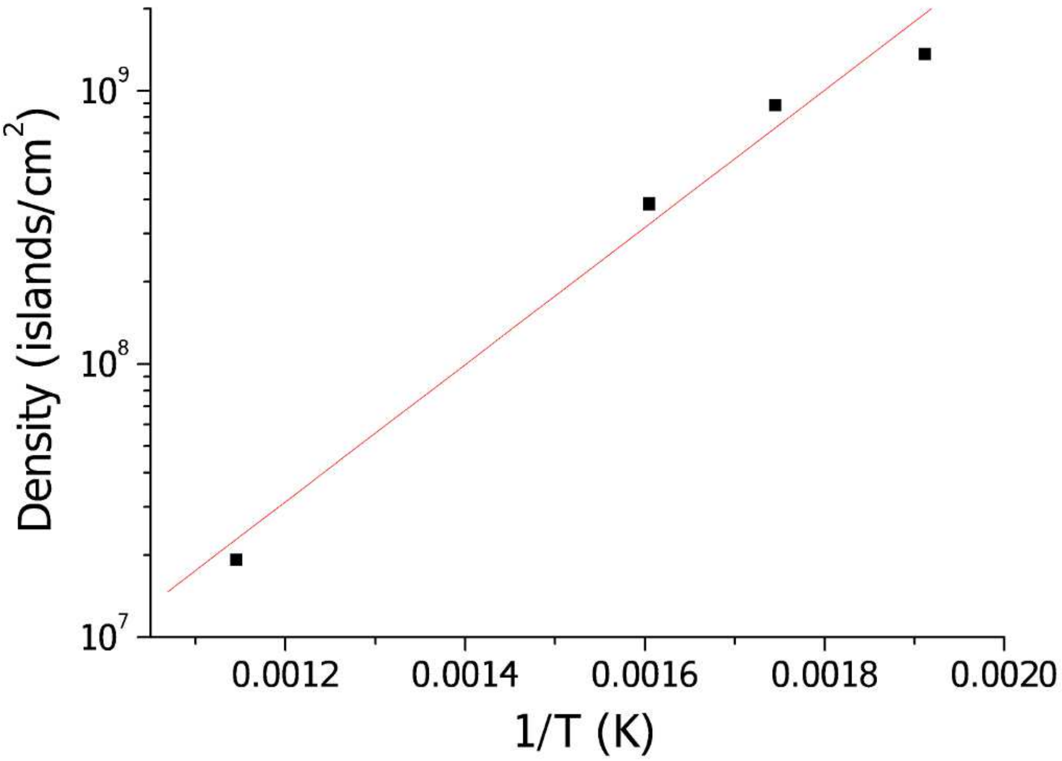

Figure 6.4: Arrhenius plot for the density of GaAs nanostructures on Si substrate.

shows the magnification of the (220) spot. The patterns of both Si and GaAs were present, confirming the formation of GaAs crystal. The less intense spots around the main Si and GaAs ones were due to double diffraction on the GaAs island and on Si substrate. Spots A and B, e.g., of the inset were due to double diffraction from the $2\overline{2}0$ and 400 GaAs spots, respectively.

TEM images acquired selecting a diffraction vector $< 220 >$ on samples A1 and A3 are showed in figure 6.7. On both samples Moiré fringes were visible. The spacing between the fringes D was related to the distance between the lattice planes of Si and GaAs by the relation $D = d_{Si}/(d_{GaAs} - d_{Si})$ where d$_{Si}$ and d$_{GaAs}$ were the distances between $< 220 >$ planes of Si and GaAs respectively. The expected value for D was 4.80. For A1 we obtained 4.40, and 4.72 for sample A3. Considering the small number of fringes and the non perfect parallelism, the results obtained are in agreement with the ones expected for bulk material, demonstrating the fully relaxation of GaAs islands. The fringe indicated by an arrow in left panel of figure 6.7 (sample A1) did not crossed the whole island and was indicative of the presence of a dislocation, probably passing through the island in the position of the fringe defect. The arrangement of Moiré fringes is more complex in right panel of figure 6.7 (sample A3). Fringes are visible only in border areas of the island. This should be related to large dimension of the GaAs islands on this sample.

By mean of Energy Dispersive Spectroscopy TEM was possible to obtain a compositional map of chemical composition inside the islands. In panel (b) and (d) of figure 6.8 were reported the compositional profiles along the direction indicated by the lines in panel (a)

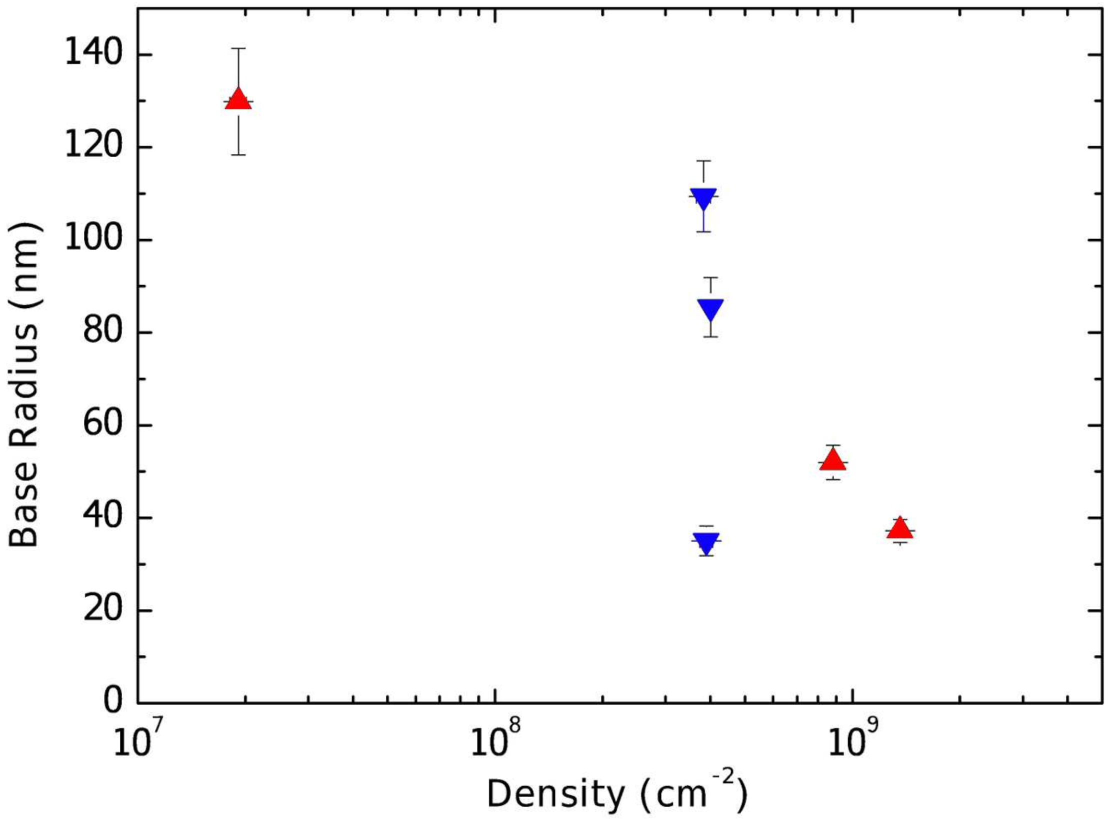

Figure 6.5: Distribution of size and density for the six different samples of GaAs islands on Si substrate.

and (c). The data reported is related to the content of Ga and As inside two different GaAs islands on samples A1. From the data obtained was possible to conclude that Ga and As are in stoichiometric ratio for the first island, while for the second a spike in Ga composition is observed in the right part of the profile.

An explanation for this behaviour emerged from high resolution SEM images. Upper left panel of figure 6.9 shows a high resolution image of a GaAs island on sample B1. On the surface of the island is possible to observe several hemispherical protuberances. The composition of these features, observed on samples A3 and B1 (big GaAs islands), was made clear by a selective wet etching for unreacted liquid Ga on the surface. This procedure was performed in a clean-room environment by dipping the sample for 30 seconds in concentrated (37%) hydrochloric acid at room temperature and then by a subsequent rinse in deionized water. At room temperature HCl is reported to remove metallic Ga from surface [95] but not to attack GaAs [96, 97] and Si(001) surface [98]. After the etching procedure high resolution SEM changed to the one showed in lower left panel of figure 6.9. The source of the gallium protuberances on the top of the islands can be only liquid gallium deposited on Si surface and not reacted with the As flux. The presence of some amount of unreacted gallium on top of GaAs quantum nanostructures fabricated by droplet epitaxy is reported in [27] and is related to a fabrication process that uses low flux and short As supply time. In the sets of experiments here reported the problem could not lie in the amount of supplied As, because there is no improvement between short and a long As supply (5 minutes for sample B1 but 30 minutes for sample A3).

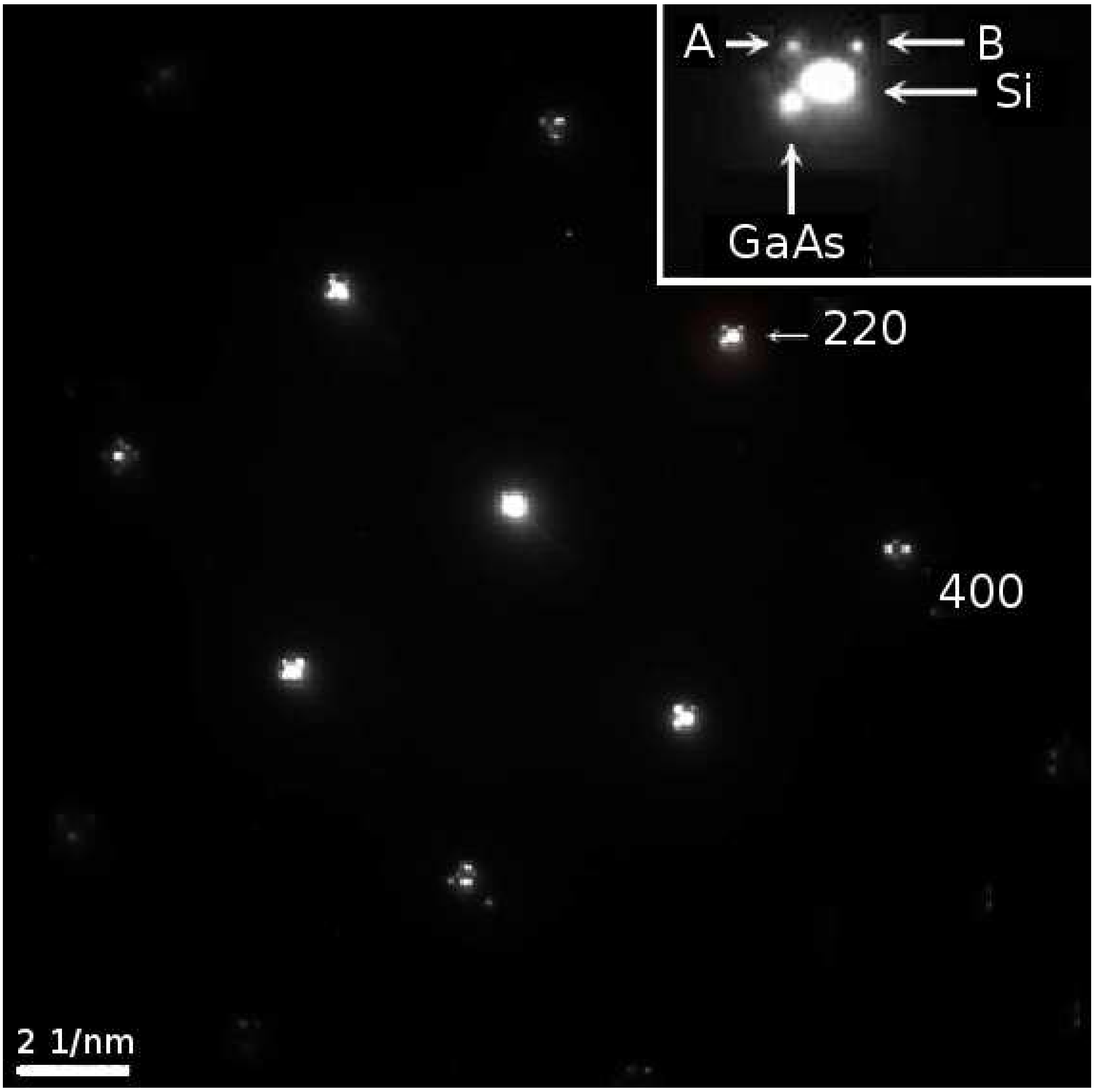

Figure 6.6: Electron diffraction pattern from a single GaAs island on Silicon substrate. Inset shows magnification of (220) spot.

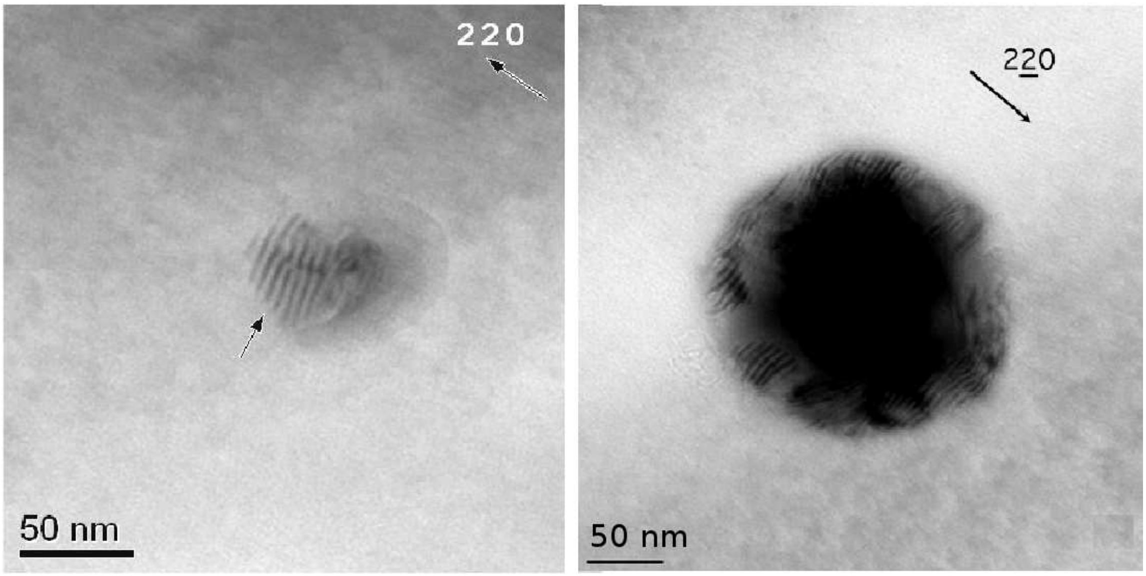

Figure 6.7: TEM images of single GaAs islands on samples A1 and A3 selecting a diffraction vector $< 220 >$.

Another feature observed on surface of sample B1, before the etching procedure, was the presence of some material forming partial rings around some islands (right panel of figure 6.9). Partial rings structures appeared to be composed by small hemispheres of few tens nanometer size. After the wet etching procedure, the partial rings were not significantly modified, so that the composition of these structures was related to GaAs and not to liquid Ga. The explanation for the formation of these rings can be in the liquid Ga on the top of the islands fallen during the island growth. Another explanation can be in the movement of the liquid droplets on the substrate surface described by Tersoff et al. [99] and caused by the formation of a surface with a different free energy after the movement of the droplet.

6.2.2 Faceting

Calculating the mean aspect ratio (i.e. the ratio between the height and the diameter) for the islands fabricated on each sample using the values of mean height and mean radius reported in table 6.2, it is possible to observe a trend between the aspect ratio and the mean size of the islands. Figure 6.10 reports the relation between height and aspect ratio of each GaAs island in an area of 5 μm $\times$ 5 μm on surface of samples B1 (black circles), B2 (red circles) and B3 (green circles). The mean aspect ratio is increasing from 0.3 on sample B3 to 0.4 on sample B2 and to 0.5 on sample B1. A similar behaviour was observed also on samples of set A.

The modification in shape for the different growth conditions can be observed not only in the aspect ratio but also in the exposed facets on the GaAs island surface. High resolution planar SEM and AFM images showed that the GaAs islands fabricated on all the samples were characterized by a round base, dictated by the starting droplet geometry, and, after the etching treatment, well defined surfaces. Figure 6.11 shows the AFM profiles of typical GaAs islands along the $[110]$ and $[1\bar{1}0]$ directions. Profiles of larger islands on sample A3 (upper panel of figure 6.11) and B1 showed that typically the angle between the bottom part of the island and the Si surface is about $54°$, while the upper part of the islands

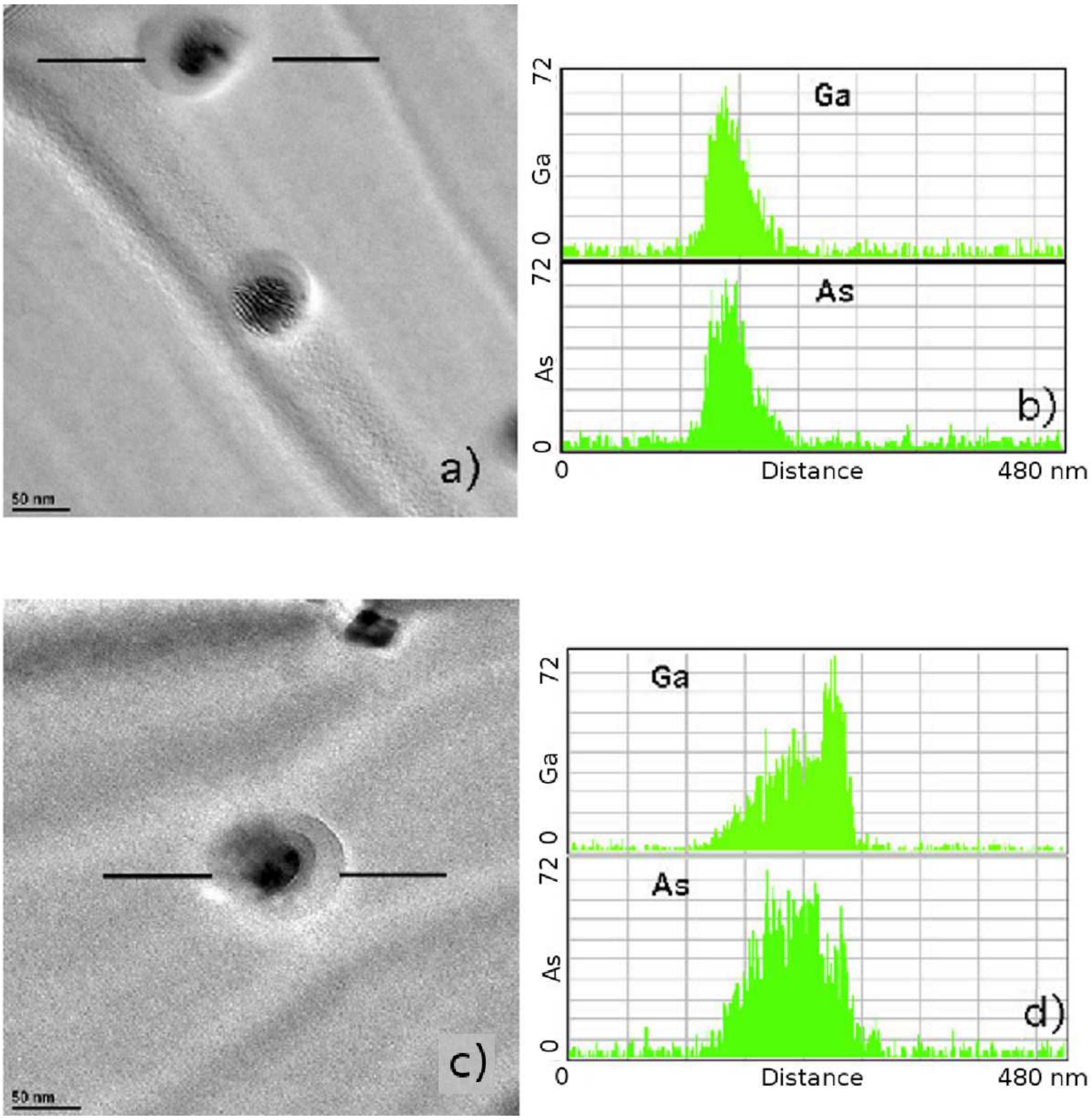

Figure 6.8: compositional profiles of two typical island on sample A1 along the direction indicated in panel (a) and (c).

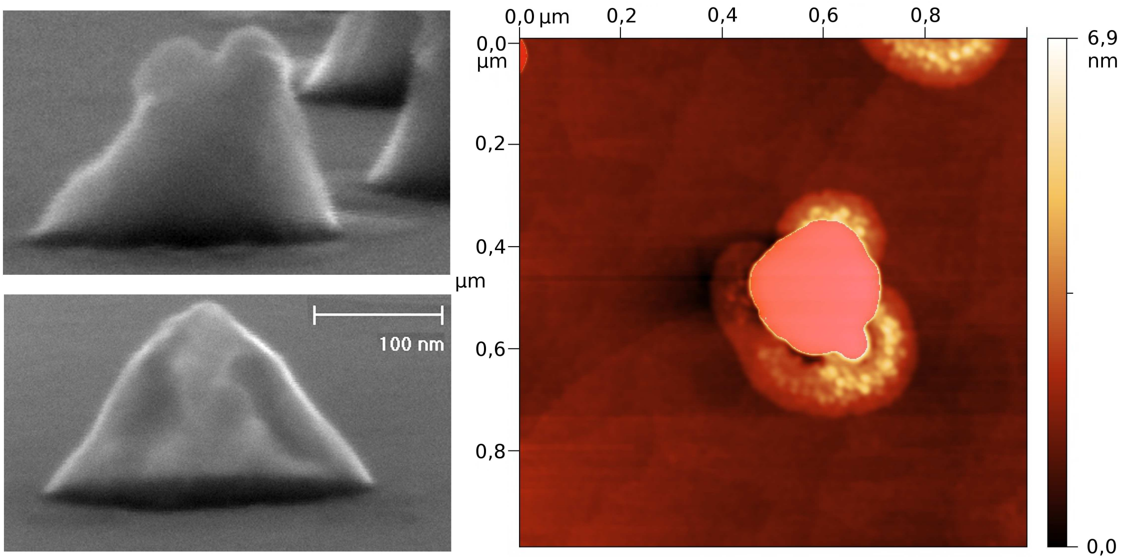

Figure 6.9: SEM images of GaAs islands on sample B1 as grown (upper left panel) and after selective etching for liquid Ga remove (lower left panel). AFM image of islands on sample B1 cutted at 6.9 nm height to enhance surface features (right panel).

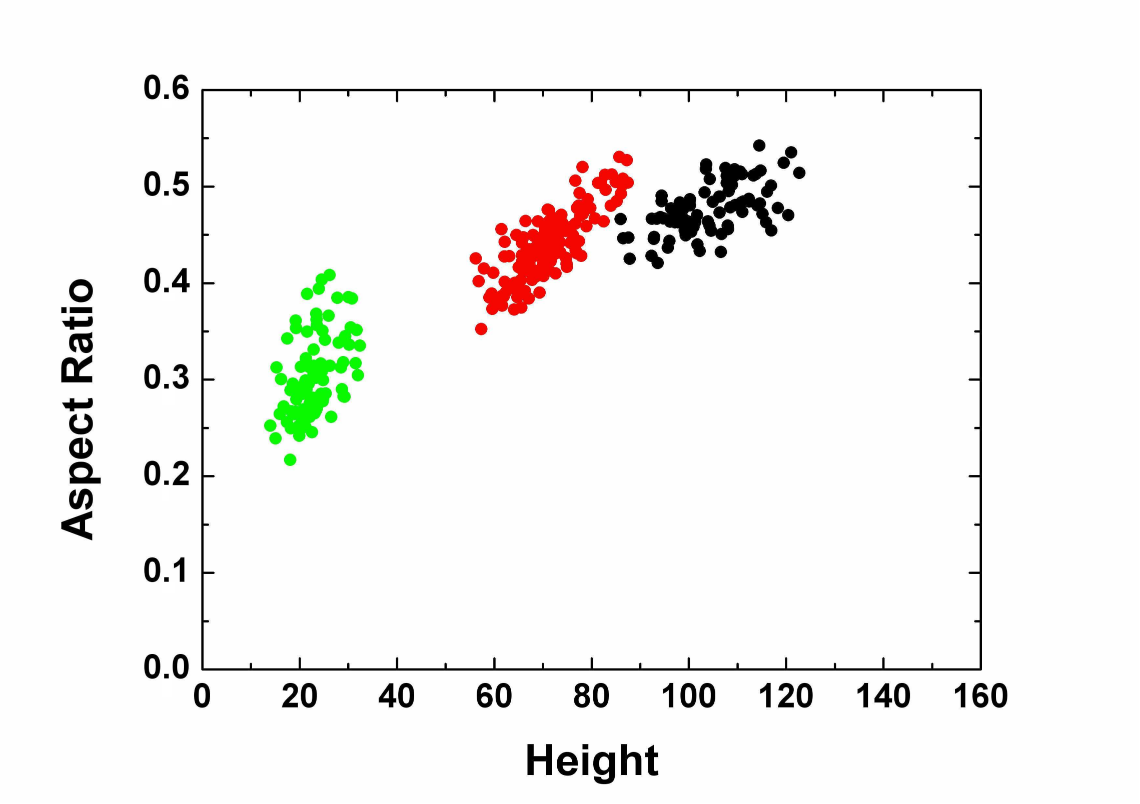

Figure 6.10: relation between height and aspect ratio of islands on sample B1 (black circles), B2 (red circles) and B3 (green circles).

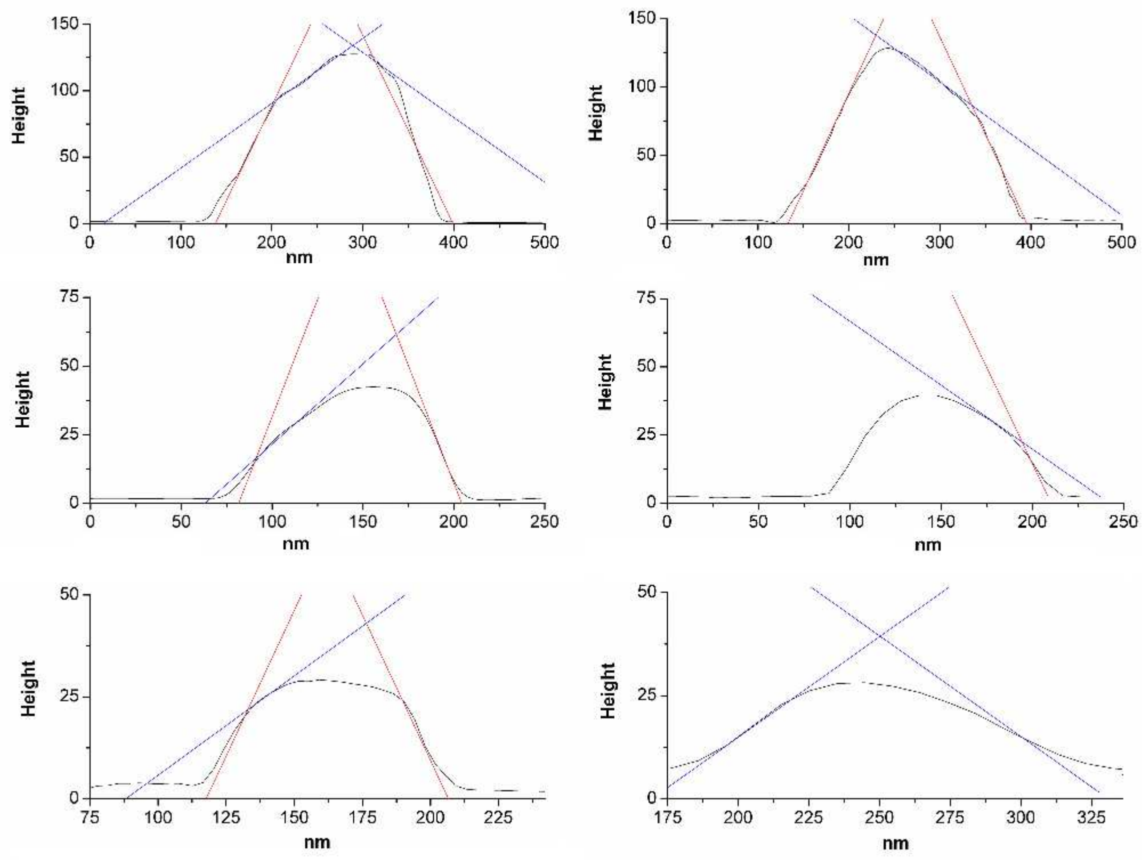

Figure 6.11: AFM profiles along $[110]$ (left column) and $[1\bar{1}0]$ (right column) directions of typical islands on samples A3 (upper panels), A2 (central panels) and B3 (lower panels). Red lines fit the profiles with $\{111\}$ planes, green lines with $\{113\}$ planes.

flattened, typically forming an angle of about 25° with the substrate. The angle of 54° is compatible with the formation of a facet along the planes of family $\{111\}$, while the angle of 26° was compatible with the formation of a facet along the planes of family $\{113\}$. Profiles of middle sized islands (sample A2, reported in central panel of figure 6.11, and sample B2) typically showed a similar behaviour, but here the part of the profile compatible with $\{111\}$ planes was reduced and enlarged the portion compatible with $\{113\}$ planes. Finally, profiles of smaller islands (sample B3, reported in central panel of figure 6.11, and sample A1) exposed larger part of profile compatible with $\{113\}$ planes, while the part of the profile related to $\{111\}$ planes was reduced or suppressed. Slope compatible with the formation of $\{101\}$ and $\{115\}$ was observed on some islands of samples A2 and A1, respectively. Formation of $\{101\}$, $\{115\}$, $\{111\}$ and $\{113\}$ facets is not surprising, because these facet families are known to be stable on GaAs surface [100, 12].

On high resolution AFM scans of single GaAs island for different samples, facet analysis was performed. Results for samples B1, A2 and B3 are reported in figure 6.12. Each plot showed the distribution of angles θ and ϕ related to the vector **n** perpendicular to the local plane tangent to each point of the high resolution AFM scan of a single GaAs island. The angle θ was reported on the plot as distance from the centre and measured the inclination of the vector **n** with respect to the $[001]$ direction (i.e. $\theta = 0$ at the centre of the plot means a local plane parallel to Si substrate). The angle ϕ was reported on the plot as the angle with the x axis and measured the angle between the projection of the vector **n** on the (001) plane and the $[100]$ (upper plot) or $[110]$ direction (lower and central plots). The plots showed the formation of facets along $\{111\}$ family plane on sample B1, along $\{101\}$ on sample A2 and $\{113\}$ on sample B3. Two more features emerged from the plots: lines crossing the origin and circles. Both behaviours indicated that the upper part of the island resembled the hemispherical shape of the original droplet. For example, the two lines crossing the origin in the upper plot (sample B1) showed that along $[110]$ and $[1\bar{1}0]$ directions the upper part of the island the slope is decreasing little by little down to zero. The partial ring observed in central plot (sample A2) attested the good cylindrical symmetry of the island.

High resolution AFM scans also showed some irregularities on the surface of the samples, and the profiles reported in figure 6.11 showed an incomplete symmetry, especially in the upper part of the islands. This behaviour con be attributed to the presence of threading dislocations inside the GaAs islands, and to the to the rapid formation of the GaAs crystal during the arsenization.

6.3 Conclusions

Droplet epitaxy is a suitable technique to provide local artificial substrates tunable in size and density, to be used for the integration of III-V quantum nanostructures on Si substrate, getting rid of the lattice mismatch between GaAs and Si and the formation of thermal cracks.

The GaAs islands fabricated by droplet epitaxy on silicon substrate are quite similar to those observed in Volmer-Weber GaAs island grown on Si for shape, aspect ratio and faceting, as reported in left column of figure 6.13. Also starting from completely different growth conditions, big islands on both images show an aspect ratio of 0.5 and expose $\{111\}$ and $\{113\}$ family plane facets. The main advantages of GaAs island grown by droplet epitaxy is the independent control of density and average size, made possible by

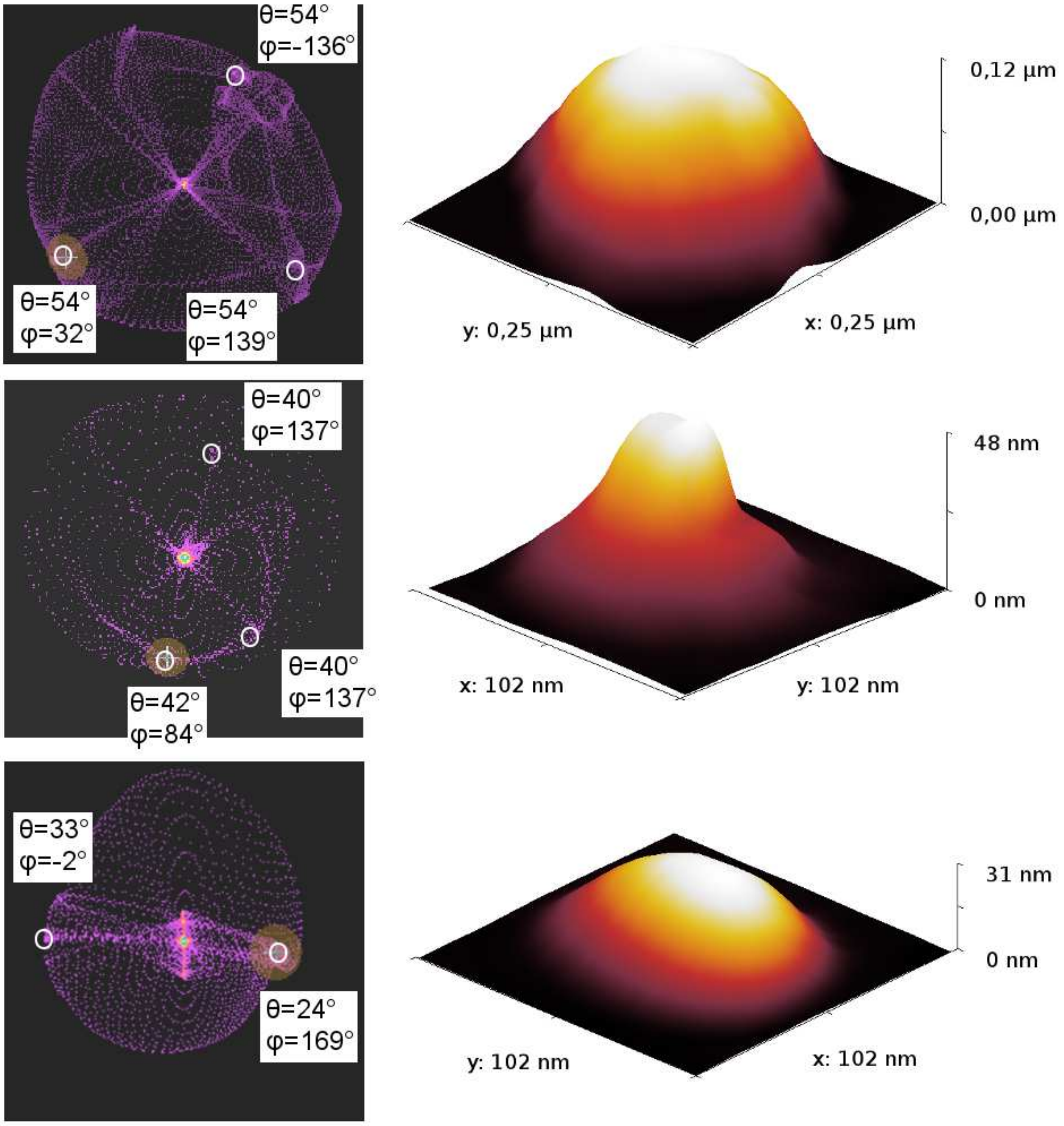

Figure 6.12: facet analysis (left column) from AFM images of single GaAs island (right column) on sample B1 (upper row), A2 (central row) and B3 (lower row). For the plots $\phi = 0$ corresponds to the direction $[100]$ (upper plot) or $[110]$ direction (lower and central plots). Circles show the position of most intense spots.

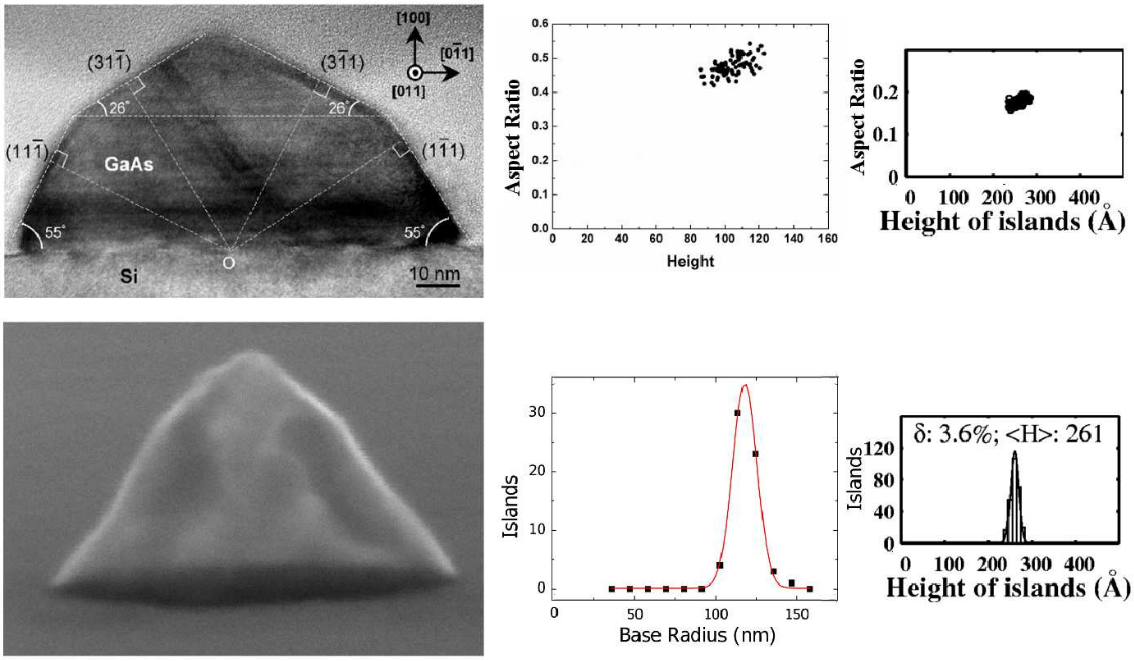

Figure 6.13: in left column: upper panel, TEM image of GaAs island on silicon substrate by Volmer-Weber growth (from [13]), lower panel, SEM image of GaAs island on B1 sample. In right columns: comparison between size dispersion for Ge islands on patterned Si substrate (upper panels) and GaAs island on Si substrate for sample B1 (lower panel).

the two steps (Ga deposition and As irradiation), and the narrow size distribution, close to the best results obtained in Stranski-Krastanow growth using patterning substrates. In central and left columns of figure 6.13 are reported data about size dispersion for Ge island growth on silicon substrate [94] (upper row) and GaAs island on sample B1 growth by droplet epitaxy (lower row). GaAs islands growth by droplet epitaxy show size dispersion lower than 10% on all the sample described in this work. The result is important, because such a low value was reported in scientific literature only for patterned substrates.

For the preparation of suitable surface on the local artificial substrates it was decisive the removal of liquid Ga protuberances. Only after removing the unreacted material is possible to prepare islands suitable for a subsequent III-V quantum nanostructures nucleation. Without this step nucleation would occur not only on an regular GaAs surface but partially on liquid gallium. As shown, the 30 s HCl etching procedure has demonstrated to be effective in the preparation of well defined island surfaces. After this step islands show a well defined profile and expose side facets belonging mainly to the $\{111\}$ and $\{113\}$ families. These surfaces plays an important role for the subsequent fabrication of quantum nanostructures on the top of artificial substrates. It is reported [91] a stronger affinity for the nucleation of InAs small quantum dots on high index surface like $\{113\}$ or $\{115\}$ than on $\{111\}$. This behaviour can be used for the preferential nucleation of InAs nanostructures on the GaAs island for the integration of III-V nanostructures on silicon substrate.

The selected technique for the fabrication of the GaAs islands, the droplet epitaxy, is intrinsically low thermal budget. Except for the Ga deposition on sample A3, performed at 600 °C, the fabrication of GaAs islands on the other five samples followed the requirements for the integration with CMOS technology [87]. In fact, due to the high tunability of droplet epitaxy, a wide range of island densities and sizes are reachable without breaking the low thermal budget requirements, making droplet epitaxy perfectly suited for the fabrication of local artificial substrates.

List of publications

- P. Regoliosi, M. Guehl, G. Scarpa, P. Lugli, L. Persano, P. Del Carro, A. Camposeo, R. Cingolani, D. Pisignano, S. Bietti, E. Grilli, and M. Guzzi, "Thermal tunability of monolithic polymer microcavities," *Applied Physics Letters*, vol. 92, no. 25, p. 253310, 2008

- S. Sanguinetti, T. Mano, A. Gerosa, C. Somaschini, S. Bietti, N. Koguchi, E. Grilli, M. Guzzi, M. Gurioli, and M. Abbarchi, "Rapid thermal annealing effects on self-assembled quantum dot and quantum ring structures," *Journal of Applied Physics*, vol. 104, no. 11, p. 113519, 2008

- S. Bietti, C. Somaschini, M. Abbarchi, N. Koguchi, S. Sanguinetti, E. Poliani, M. Bonfanti, M. Gurioli, A. Vinattieri, T. Kuroda, T. Mano, and S. Sakoda, "Quantum dots to double concentric quantum ring structures transition," *Physica Status Solidi (C)*, vol. 6, pp. 928–931, Apr. 2009

- S. Bietti, S. Sanguinetti, C. Somaschini, N. Koguchi, G. Isella, D. Chrastina, and A. Fedorov, "Fabrication of GaAs quantum dots by droplet epitaxy on Si/Ge virtual substrate," *IOP Conference Series: Materials Science and Engineering*, vol. 6, p. 012009, Nov. 2009

- S. Bietti, C. Somaschini, S. Sanguinetti, N. Koguchi, G. Isella, and D. Chrastina, "Fabrication of high efficiency III-V quantum nanostructures at low thermal budget on Si," *Applied Physics Letters*, vol. 95, no. 24, p. 241102, 2009

- C. Somaschini, S. Bietti, N. Koguchi, and S. Sanguinetti, "Fabrication of multiple concentric nanoring structures.," *Nano Letters*, vol. 9, pp. 3419–24, Oct. 2009

- C. Somaschini, S. Bietti, S. Sanguinetti, N. Koguchi, A. Fedorov, M. Abbarchi, and M. Gurioli, "Fabrication of GaAs concentric multiple quantum rings by droplet epitaxy," *IOP Conference Series: Materials Science and Engineering*, vol. 6, p. 012008, Nov. 2009

- S. Bietti, C. Somaschini, S. Sanguinetti, N. Koguchi, G. Isella, D. Chrastina, and A. Fedorov, "Low Thermal Budget Fabrication of III-V Quantum Nanostructures on Si Substrates," *Journal of Physics: Conference Series*, vol. 245, p. 012078, Sept. 2010

- C. Somaschini, S. Bietti, S. Sanguinetti, N. Koguchi, and A. Fedorov, "Control of the lateral growth morphology in GaAs Droplet Epitaxy," *Journal of Physics: Conference Series*, vol. 245, p. 012082, Sept. 2010

- S. Bietti, C. Somaschini, N. Koguchi, C. Frigeri, and S. Sanguinetti, "Self-Assembled Local Artificial Substrates of GaAs on Si Substrate," *Nanoscale Research Letters*, pp. 9–11, 2010
- S. Bietti, C. Somaschini, E. Sarti, N. Koguchi, S. Sanguinetti, G. Isella, D. Chrastina, and A. Fedorov, "Photoluminescence Study of Low Thermal Budget III-V Nanostructures on Silicon by Droplet Epitaxy," *Nanoscale Research Letters*, vol. 5, pp. 1650–1653, 2010
- C. Somaschini, S. Bietti, A. Fedorov, N. Koguchi, and S. Sanguinetti, "Growth Interruption Effect on the Fabrication of GaAs Concentric Multiple Rings by Droplet Epitaxy," *Nanoscale Research Letters*, pp. 5–8, Aug. 2010
- C. Somaschini, S. Bietti, A. Fedorov, N. Koguchi, and S. Sanguinetti, "Concentric Multiple Rings by Droplet Epitaxy: Fabrication and Study of the Morphological Anisotropy," *Nanoscale Research Letters*, pp. 9–11, Aug. 2010
- C. Somaschini, S. Bietti, N. Koguchi, F. Montalenti, C. Frigeri, and S. Sanguinetti, "Self-assembled GaAs islands on Si by droplet epitaxy," *Applied Physics Letters*, vol. 97, no. 5, p. 053101, 2010
- C. Somaschini, S. Bietti, S. Sanguinetti, N. Koguchi, and A. Fedorov, "Self-assembled GaAs/AlGaAs coupled quantum ring-disk structures by droplet epitaxy," *Nanotechnology*, vol. 21, p. 125601, Mar. 2010

Bibliography

[1] K. Gunther *Zeitschrift für Naturforschung*, vol. 13a, p. 1981, 1958.

[2] J. Davey and T. Pankey, “Epitaxial GaAs films deposited by vacuum evaporation,” *Journal of Applied Physics*, vol. 39, no. 4, pp. 1941–1948, 1968.

[3] A. Cho, M. Panish, and I. Hayashi *3rd Int. Symp. on Gallium Arsenide and Related Compounds, The Institute of Physics, Conference Series*, no. 9, pp. 18–29, 1970.

[4] H. Shelton and A. Cho, “Evaporative lifetimes of copper, chromium, beryllium, nickel, iron, and titanium on tungsten and oxygenated tungsten,” *Journal of Applied Physics*, vol. 37, no. 9, pp. 3544–3548, 1966.

[5] J. Arthur Jr., “Interaction of Ga and As_2 molecular beams with GaAs surfaces,” *Journal of Applied Physics*, vol. 39, no. 8, pp. 4032–4034, 1968.

[6] A. Cho and I. Hayashi, “Surface structures and photoluminescence of molecular beam epitaxial films of GaAs,” *Solid State Electronics*, vol. 14, no. 2, pp. 125–132, 1971.

[7] H. Luth, *Solid surfaces, interfaces and thin films*. Springer, 2001.

[8] H. Vineyard, “Frequency factors and isotope effects in solid state rate processes,” *Journal of Physics and Chemistry of Solids*, vol. 3, pp. 121–127, 1957.

[9] C. Herring, “Some Theorems on the Free Energies of Crystal Surfaces,” *Physical Review*, vol. 82, pp. 87–93, 1951.

[10] J. T. Robinson, A. Rastelli, O. Schmidt, and O. D. Dubon, “Global faceting behavior of strained Ge islands on Si,” *Nanotechnology*, vol. 20, p. 085708, Feb. 2009.

[11] N. Moll, A. Kley, E. Pehlke, and M. Scheffler, “GaAs equilibrium crystal shape from first principles.,” *Physical review. B, Condensed matter*, vol. 54, pp. 8844–8855, Sept. 1996.

[12] P.-S. Wong, B. Liang, R. Molecke, J. Tatebayashi, and D. L. Huffaker, “Controlled Formation and Dynamic Wulff Simulation of Equilibrium Crystal Shapes of GaAs Pyramidal Structures on Nanopatterned Substrates,” *Crystal Growth & Design*, vol. 10, pp. 2509–2514, June 2010.

[13] H. Usui, H. Yasuda, and H. Mori, “Crystal shape of GaAs nanocrystals deposited on Si(100) by molecular beam epitaxy,” *Thin Solid Films*, vol. 516, pp. 2487 – 2490, 2008.

[14] J. H. Neave, B. A. Joyce, P. J. Dobson, and N. Norton, “Dynamics of film growth of GaAs by MBE from Rheed observations,” *Applied Physics A Solids and Surfaces*, pp. 1–8, May 1983.

[15] N. J. C. Ingle, A. Yuskauskas, R. Wicks, M. Paul, and S. Leung, “The structural analysis possibilities of reflection high energy electron diffraction,” *Journal of Physics D: Applied Physics*, vol. 43, p. 133001, Apr. 2010.

[16] B. J. Ohlsson and M. S. Miller, “Growth of strained GaAs islands on (001) GaP: a RHEED study of quantum wire formation,” *Journal of Crystal Growth*, vol. 188, pp. 387–391, 1998.

[17] D. Bimberg, N. Grundmann, and N. N. Ledentsov, *Quantum Dots Heterostructures*. Wiley, 1998.

[18] K. Akahane, N. Yamamoto, and T. Kawanishi, “High Characteristic Temperature of Highly Stacked Quantum-Dot Laser for 1.55-μm Band,” *IEEE Photonics Technology Letters*, vol. 22, pp. 103–105, Jan. 2010.

[19] K. Akahane, N. Yamamoto, and M. Tsuchiya, “Highly stacked quantum-dot laser fabricated using a strain compensation technique,” *Applied Physics Letters*, vol. 93, no. 4, p. 041121, 2008.

[20] N. Koguchi, S. Takahashi, and T. Chikyow, “New MBE growth method for InSb quantum well boxes,” *Journal of Crystal Growth*, vol. 111, pp. 688–692, 1991.

[21] N. Koguchi and K. Ishige, “Growth of GaAs Epitaxial Microcrystal on an S-Terminated GaAs Substrate by Successive Irradiation of Ga and As Molecular Beams,” *Japanese Journal of Applied Physics*, vol. 32, pp. 2052–2058, 1993.

[22] C. Deparis, J. Massies, and I. Introduction, “Surface stoichiometry variation associated with GaAs (001) reconstruction transitions,” *Journal of Crystal Growth*, vol. 108, pp. 157–172, 1991.

[23] J. Osaka, N. Inoue, Y. Mada, K. Yamada, and K. Wada, “In-situ observation of roughening process of MBE GaAs surface by scanning reflection electron microscopy,” *Journal of Crystal Growth*, vol. 99, pp. 120–123, 1990.

[24] K. Watanabe, N. Koguchi, and Y. Gotoh, “Fabrication of GaAs Quantum Dots by Modified Droplet Epitaxy,” *Japanese Journal of Applied Physics*, vol. 39, no. 2, pp. 79–81, 2000.

[25] T. Mano and N. Koguchi, “Nanometer-scale GaAs ring structure grown by droplet epitaxy,” *Journal of Crystal Growth*, vol. 278, pp. 108–112, May 2005.

[26] T. Mano, T. Kuroda, S. Sanguinetti, T. Ochiai, T. Tateno, J. Kim, T. Noda, M. Kawabe, K. Sakoda, G. Kido, and N. Koguchi, “Self-assembly of concentric quantum double rings.,” *Nano letters*, vol. 5, pp. 425–8, Mar. 2005.

[27] C. Somaschini, S. Bietti, N. Koguchi, and S. Sanguinetti, “Fabrication of multiple concentric nanoring structures.,” *Nano Letters*, vol. 9, pp. 3419–24, Oct. 2009.

[28] M. A. Kastner, "Mesoscopic physics and artificial atoms," *Physics Today*, pp. 573–585, 1992.

[29] L. Pavesi and M. Guzzi, "Photoluminescence of $\mathrm{AI}_x\mathrm{Ga}_{1-x}\mathrm{As}$ alloys," *Journal of Applied Physics*, vol. 75, no. 10, p. 4779, 1994.

[30] K. Watanabe, S. Tsukamoto, Y. Gotoh, and N. Koguchi, "Photoluminescence studies of GaAs quantum dots grown by droplet epitaxy," *Journal of Crystal Growth*, vol. 227-228, pp. 1073–1077, July 2001.

[31] S. Sanguinetti, K. Watanabe, T. Kuroda, F. Minami, Y. Gotoh, and N. Koguchi, "Effects of post-growth annealing on the optical properties of self-assembled GaAs/AlGaAs quantum dots," *Journal of Crystal Growth*, vol. 242, pp. 321–331, 2002.

[32] V. Mantovani, S. Sanguinetti, M. Guzzi, E. Grilli, M. Gurioli, K. Watanabe, and N. Koguchi, "Low density GaAs/AlGaAs quantum dots grown by modified droplet epitaxy," *Journal of Applied Physics*, vol. 96, no. 8, p. 4416, 2004.

[33] J. Crank, *The Mathematics of Diffusion*. Clarendon Press, 1955.

[34] J.-Y. Marzin and G. Bastard, "Calculation of the energy levels in InAs/GaAs quantum dots," *Solid State Communications*, vol. 92, no. 5, pp. 437–442, 1994.

[35] T. Kuroda, T. Mano, T. Ochiai, S. Sanguinetti, K. Sakoda, G. Kido, and N. Koguchi, "Optical transitions in quantum ring complexes," *Physical Review B*, vol. 72, p. 205301, Nov. 2005.

[36] A. Ohtake, "Surface reconstructions on GaAs(001)," *Surface Science Reports*, vol. 63, pp. 295–327, July 2008.

[37] D. J. Chadi, "Atomic and Electronics-Structures of Reconstructed Si(100) Surfaces," *Physical Review Letters*, vol. 43, no. 1, pp. 43–47, 1979.

[38] R. J. Hamers, R. M. Tromp, and J. E. Demuth, "Scannig tunneling microscopy of Si(001)," *Physical Review B*, vol. 34, no. 8, p. 5343, 1986.

[39] D. J. Chadi, "Stabilities of single-layer and bilayer steps on Si(001) surfaces," *Physical Review Letters*, vol. 59, no. 15, p. 1691, 1987.

[40] R. I. G. Uhrberg, R. D. Bringans, R. Z. Bachrach, and J. E. Northup, "Electronic and atomic structure of arsenic terminated Si(100)," *Journal of Vacuum Science & Technology A*, vol. 4, no. 3, p. 1259, 1986.

[41] R. Fischer, W. T. Masselink, J. Klem, T. Henderson, T. C. McGlinn, M. V. Klein, H. Morkoc, J. H. Mazur, and J. Washburn, "Growth and properties of GaAs/AlGaAs on nonpolar substrates using molecular beam epitaxy," *Journal of Applied Physics*, vol. 58, no. 1, p. 374, 1985.

[42] W. I. Wang, "Molecular beam epitaxial growth and material properties of GaAs and AIGaAs on Si (100)," *Applied Physics Letters*, vol. 44, no. 12, pp. 1149–1151, 1984.

[43] S. F. Fang, K. Adomi, S. Iyer, H. Morkoc, H. Zabel, C. Choi, and N. Otsuka, “Gallium arsenide and other compound semiconductors on silicon,” *Journal of Applied Physics*, vol. 68, no. 7, p. R31, 1990.

[44] R. D. Bringans, D. K. Biegelsen, and L. E. Swartz, “Atomic-Step rearrangement on Si(100) by Interaction with Arsenic and the Implication for GaAs-on-Si Epitaxy,” *Physical Review B*, vol. 44, pp. 3054–3063, 1991.

[45] S. M. Ting and E. A. Fitzgerald, “Metal-organic chemical vapor deposition of single domain GaAs on Ge/Ge$_x$Si$_{1-x}$/Si and Ge substrates,” *Journal of Applied Physics*, vol. 87, no. 5, p. 2618, 2000.

[46] J. H. Van Der Merwe, “Crystal Interfaces. Part II. Finite Overgrowths,” *Journal of Applied Physics*, vol. 34, no. 1, p. 123, 1963.

[47] J. W. Matthews and A. E. Blakeslee, “Defects in epitaxial multilayers I. Misfit dislocations,” *Journal of Crystal Growth*, vol. 27, pp. 118–125, 1974.

[48] N. Otsuka, C. Choi, L. A. Kolodziejski, R. L. Gunshor, R. Fischer, C. K. Peng, H. Morkoc, Y. Nakamura, and S. Nagakura, “Study of heteroepitaxial interfaces by atomic resolution electron microscopy,” *Journal of Vacuum Science & Technology B*, vol. 4, p. 896, July 1986.

[49] D. K. Biegelsen, F. A. Ponce, A. J. Smith, and J. C. Tramontana, “Initial stages of epitaxial growth of GaAs on (100) silicon,” *Journal of Applied Physics*, vol. 61, no. 5, p. 1856, 1987.

[50] P. Politi, G. Grenet, A. Marty, A. Ponchet, and J. Villain, “Instabilities in crystal growth by atomic or molecular beams,” *Physics Reports*, vol. 324, pp. 271–404, Feb. 2000.

[51] F. K. LeGoues, M. C. Reuter, J. Tersoff, M. Hammar, and R. M. Tromp, “Cyclic growth of strained-relaxed islands,” *Physical Review Letters*, vol. 73, no. 2, p. 300, 1994.

[52] S. Guha, A. Madhukar, and K. C. Rajkumar, “Onset of incoherency and defect introduction in the initial stages of molecular beam epitaxieal growth of highly strained In,” *Applied Physics Letters*, vol. 57, no. 20, pp. 2110–2112, 1990.

[53] R. Fischer, N. Chand, W. Kopp, H. Morkoc, P. Erickson, and R. Youngman, “GaAs bipolar transistors grown on (100) Si substrates by molecular beam epitaxy,” *Applied Physics Letters*, vol. 47, no. 4, pp. 397–399, 1985.

[54] J. M. Baribeau, T. E. Jackman, D. C. Houghton, P. Maigné, and M. W. Denhoff, “Growth and characterization of Si$_{1-x}$Ge$_x$ and Ge epilayers on (100) Si,” *Journal of Applied Physics*, vol. 63, p. 5738, Nov. 1988.

[55] E. A. Fitzgerald, Y. Xie, M. L. Green, D. Brasen, A. R. Kortan, J. Michel, Y. J. Mii, and B. E. Weir, “Totally relaxed Ge$_x$Si$_{1-x}$ layers with low threading dislocation densities grown on Si substrates,” *Applied Physics Letters*, vol. 59, no. 7, pp. 811–813, 1991.

[56] S. B. Samavedam and E. A. Fitzgerald, “Novel dislocation structure and surface morphology effects in relaxed Ge/Si-Ge(graded)/Si structures,” *Journal of Applied Physics*, vol. 81, no. 7, p. 3108, 1997.

[57] G. Brammertz, Y. Mols, S. Degroote, V. Motsnyi, M. Leys, G. Borghs, and M. Caymax, “Low-temperature photoluminescence study of thin epitaxial GaAs films on Ge substrates,” *Journal of Applied Physics*, vol. 99, no. 9, p. 93514, 2006.

[58] M. K. Hudait, P. Modak, S. Hardikar, S. B. Krupanidhi, and I. Introduction, “Photoluminescence studies on Si-doped GaAs/Ge,” *Journal of Applied Physics*, vol. 83, no. 8, pp. 4454–4461, 1998.

[59] E. P. Visser, X. Tang, R. W. Wieleman, and L. J. Giling, “Deep-level photoluminescence studies on Si-doped, metalorganic chemical vapor deposition grown $\mathrm{Al}_x\mathrm{Ga}_{1-x}\mathrm{As}$,” *Journal of Applied Physics*, vol. 69, no. 5, p. 3266, 1991.

[60] R. M. Sieg, S. A. Ringel, S. M. Ting, S. B. Samavedam, M. Currie, T. Langdo, and E. A. Fitzgerald, “Toward device-quality GaAs growth by molecular beam epitaxy on offcut $\mathrm{Ge/Si}_{1-x}\mathrm{Ge}_x\mathrm{/Si}$ substrates,” *Journal of Vacuum Science & Technology B*, vol. 16, no. 3, pp. 1471–1474, 1998.

[61] Y. Horikoshi and M. Kawashima, “Growth mechanism of GaAs during Migration-Enhanced Epitaxy at low growth temperatures,” *Japanese Journal of Applied Physics*, vol. 28, no. 2, p. 200, 1989.

[62] C. Rosenblad, H. R. Deller, A. Dommann, T. Meyer, P. Schroeter, and H. von Känel, “Silicon epitaxy by low-energy plasma enhanced chemical vapor deposition,” *Journal of Vacuum Science & Technology A*, vol. 16, p. 2785, Sept. 1998.

[63] P. L. Novikov, A. Le Donne, S. Cereda, L. Miglio, S. Pizzini, S. Binetti, M. Rondanini, C. Cavallotti, D. Chrastina, T. Moiseev, H. von Känel, G. Isella, and F. Montalenti, “Crystallinity and microstructure in Si films grown by plasma-enhanced chemical vapor deposition: A simple atomic-scale model validated by experiments,” *Applied Physics Letters*, vol. 94, no. 5, p. 051904, 2009.

[64] S. G. Thomas, S. Bharatan, R. E. Jones, R. Thoma, T. Zirkle, N. V. Edwards, R. Liu, X. D. Wang, Q. Xie, C. Rosenblad, J. Ramm, G. Isella, and H. von Känel, “Structural characterization of thick, high-quality epitaxial Ge on Si substrates grown by low-energy plasma-enhanced chemical vapor deposition,” *Journal of Electronic Materials*, vol. 32, no. 9, p. 976, 2003.

[65] S. Marchionna, A. Virtuani, M. Acciarri, G. Isella, and H. von Känel, “Defect imaging of SiGe strain relaxed buffers grown by LEPECVD,” *Materials Science in Semiconductor Processing*, vol. 9, no. 4-5, pp. 802–805, 2006.

[66] G. Isella, D. Chrastina, B. Rossner, T. Hackbarth, H.-J. Herzog, U. Konig, and H. von Känel, “Low-energy plasma-enhanced chemical vapor deposition for strained Si and Ge heterostructures and devices,” *Solid-State Electronics*, vol. 48, no. 8, pp. 1317–1323, 2004.

[67] G. Isella, J. Osmond, M. Kummer, R. Kaufmann, and H. von Känel, “Heterojunction photodiodes fabricated from Ge/Si (100) layers grown by low-energy plasma-enhanced CVD,” *Semiconductor Science and Technology*, vol. 22, no. 1, pp. S26–S28, 2007.

[68] J. Osmond, G. Isella, D. Chrastina, R. Kaufmann, M. Acciarri, and H. von Känel, “Ultralow dark current Ge/Si(100) photodiodes with low thermal budget,” *Applied Physics Letters*, vol. 94, no. 20, p. 201106, 2009.

[69] H.-c. Luan, D. R. Lim, K. K. Lee, K. M. Chen, J. G. Sandland, K. Wada, and L. C. Kimerling, “High-quality Ge epilayers on Si with low threading-dislocation densities,” *Applied Physics Letters*, vol. 75, no. 19, pp. 2909–2911, 1999.

[70] L. Colace, G. Masini, S. Cozza, G. Assanto, F. DeNotaristefani, and V. Cencelli, “Near-infrared camera in polycrystalline germanium integrated on complementary-metal-oxide semiconductor electronics,” *Applied Physics Letters*, vol. 90, p. 011103, 2007.

[71] D. Colombo, E. Grilli, M. Guzzi, S. Sanguinetti, S. Marchionna, M. Bonfanti, A. Fedorov, H. von Känel, G. Isella, and E. Muller, “Analysis of strain relaxation by microcracks in epitaxial GaAs grown on Ge/Si substrates,” *Journal of Applied Physics*, vol. 101, no. 10, p. 103519, 2007.

[72] D. Colombo, E. Grilli, M. Guzzi, S. Sanguinetti, A. Fedorov, H. von Känel, and G. Isella, “Study of thermal strain relaxation in GaAs grown on Ge/Si substrates,” *Journal of Luminescence*, vol. 121, no. 2, pp. 375–378, 2006.

[73] S. Dongmo, M. Troyon, P. Vautrot, E. Delain, and N. Bonnet, “Blind restoration method of scanning tunneling and atomic force microscopy images,” *Journal of Vacuum Science & Technology B*, vol. 14, p. 1552, Mar. 1996.

[74] J. S. Villarrubia, “Algorithms for Scanned Probe Microscope Image Simulation, Surface Reconstruction, and Tip Estimation,” *Journal Of Research Of The National Institute Of Standards And Technology*, vol. 102, no. 4, p. 425, 1997.

[75] T. Mano, T. Kuroda, T. Noda, and K. Sakoda, “Ordering of GaAs quantum dots by droplet epitaxy,” *Physica Status Solidi B-Basic Research*, vol. 246, pp. 729–732, Apr. 2009.

[76] G. Oelgart, R. Schwabe, H. Fieseler, and B. Jacobs, “Photoluminescence of Ge-doped $\mathrm{Al}_x\mathrm{Ga}_{1-x}\mathrm{As}$,” *Journal of Applied Physics*, vol. 3, p. 943, 1988.

[77] C. K. Chia, J. R. Dong, D. Z. Chi, A. Sridhara, A. S. W. Wong, M. Suryana, G. K. Dalapati, S. J. Chua, and S. J. Lee, “Effects of AlAs interfacial layer on material and optical properties of GaAs/Ge(100) epitaxy,” *Applied Physics Letters*, vol. 92, p. 141905, Apr. 2008.

[78] R. M. Sieg, S. A. Ringel, S. M. Ting, E. A. Fitzgerald, and R. N. Sacks, “Anti-phase domain-free growth of GaAs on offcut (001) Ge wafers by molecular beam epitaxy with suppressed Ge outdiffusion,” *Journal of Electronic Materials*, vol. 27, pp. 900–907, July 1998.

[79] H. Tanoto, S. F. Yoon, W. K. Loke, E. A. Fitzgerald, C. Dohrman, B. Narayanan, M. T. Doan, and C. H. Tung, "Growth of GaAs on vicinal Ge surface using low-temperature migration-enhanced epitaxy," *Journal of Vacuum Science & Technology B: Microelectronics and Nanometer Structures*, vol. 24, no. 1, p. 152, 2006.

[80] Y. Horikoshi, M. Kawashima, and H. Yamaguchi, "Migration-Enhanced Epitaxy of GaAs and AlGaAs," *Japanese Journal of Applied Physics*, vol. 27, no. 2, pp. 169–179, 1988.

[81] C. Somaschini, S. Bietti, S. Sanguinetti, N. Koguchi, and A. Fedorov, "Self-assembled GaAs/AlGaAs coupled quantum ring-disk structures by droplet epitaxy," *Nanotechnology*, vol. 21, p. 125601, Mar. 2010.

[82] L. Lester, A. Stintz, H. Li, T. Newell, E. Pease, B. Fuchs, and K. Malloy, "Optical Characteristics of 1.24-$/mu$m InAs Quantum-Dot Laser Diodes," *IEEE Photonics Technology Letters*, vol. 11, no. 8, pp. 931–933, 1999.

[83] S. Raghavan, P. Rotella, A. Stintz, B. Fuchs, S. Krishna, C. Morath, D. A. Cardimona, and S. W. Kennerly, "High-responsivity, normal-incidence long-wave infrared InAs/In$_{0.15}$Ga$_{0.85}$As dots-in-a-well detector," *Applied Physics Letters*, vol. 81, no. 8, pp. 1369–1371, 2002.

[84] J. Wu, Z. Li, D. Shao, M. O. Manasreh, V. P. Kunets, Z. M. Wang, G. J. Salamo, and B. D. Weaver, "Multicolor photodetector based on GaAs quantum rings grown by droplet epitaxy," *Applied Physics Letters*, vol. 94, no. 17, p. 171102, 2009.

[85] S. Sanguinetti, T. Mano, A. Gerosa, C. Somaschini, S. Bietti, N. Koguchi, E. Grilli, M. Guzzi, M. Gurioli, and M. Abbarchi, "Rapid thermal annealing effects on self-assembled quantum dot and quantum ring structures," *Journal of Applied Physics*, vol. 104, no. 11, p. 113519, 2008.

[86] S. Sanguinetti, D. Colombo, M. Guzzi, E. Grilli, M. Gurioli, L. Seravalli, P. Frigeri, and S. Franchi, "Carrier thermodynamics in InAs/In$_x$Ga$_{1-x}$As quantum dots," *Physical Review B*, vol. 74, pp. 1–6, Nov. 2006.

[87] H. Takeuchi, A. Wung, X. Sun, R. T. Howe, and T.-j. King, "Thermal Budget Limits of Quarter-Micrometer Foundry CMOS for Post-Processing MEMS Devices," *IEEE Transactions on Electron Devices*, vol. 52, pp. 2081–2086, Sept. 2005.

[88] F. Briones, L. Gonzales, M. Recio, and M. Vazquez, "Low-Temperature Growth of AlAs/GaAs Heterostructures by Modulated Molecular Beam Epitaxy," *Japanese Journal of Applied Physics*, vol. 26, no. 7, pp. L1125–L1127, 1987.

[89] T. Suzuki and T. Nishinaga, "Modulation Molecular Beam Epitaxy under Constant Low As Pressure," *Japanese Journal of Applied Physics*, vol. 33, pp. 1759–1766, Apr. 1994.

[90] J. He, K. Yadavalli, Z. Zhao, N. Li, Z. Hao, K. L. Wang, and A. P. Jacob, "InAs/GaAs nanostructures grown on patterned Si(001) by molecular beam epitaxy," *Nanotechnology*, vol. 19, p. 455607, Nov. 2008.

[91] P.-S. Wong, G. Balakrishnan, N. Nuntawong, J. Tatebayashi, and D. L. Huffaker, "Controlled InAs quantum dot nucleation on faceted nanopatterned pyramids," *Applied Physics Letters*, vol. 90, no. 18, p. 183103, 2007.

[92] P. S. Wong, B. L. Liang, V. G. Dorogan, A. R. Albrecht, J. Tatebayashi, X. He, N. Nuntawong, Y. I. Mazur, G. J. Salamo, S. R. J. Brueck, and D. L. Huffaker, "Improved photoluminescence efficiency of patterned quantum dots incorporating a dots-in-the-well structure," *Nanotechnology*, vol. 19, p. 435710, Oct. 2008.

[93] Z. M. Zhao, O. Hulko, T. S. Yoon, and Y. H. Xie, "Initial stage of InAs growth on Si (001) studied by high-resolution transmission electron microscopy," *Journal of Applied Physics*, vol. 98, no. 12, p. 123526, 2005.

[94] Z. Zhong and G. Bauer, "Site-controlled and size-homogeneous Ge islands on prepatterned Si (001) substrates," *Applied Physics Letters*, vol. 84, no. 11, p. 1922, 2004.

[95] M. K. Kelly, O. Ambacher, B. Dahlheimer, G. Groos, R. Dimitrov, H. Angerer, and M. Stutzmann, "Optical patterning of GaN films," *Applied Physics Letters*, vol. 69, no. 12, p. 1749, 1996.

[96] J. Hong, S. J. Pearton, W. S. Hobson, and H. Han, "Selective and non-selective wet chemical etching of GaAsP," *Solid-State Electronics*, vol. 39, no. 11, pp. 1675–1677, 1996.

[97] A. Jenichen and C. Engler, "Etching of GaAs(100) surfaces by HCl: density functional calculations to the mechanisms," *Surface Science*, vol. 475, pp. 131–139, Mar. 2001.

[98] Y. Bogumilowicz, J. M. Hartmann, J. M. Fabri, and T. Billon, "Selective chemical vapour etching of $\mathrm{Si}_{1-x}\mathrm{Ge}_x$ versus Si with gaseous HCl," *Semiconductor Science and Technology*, vol. 21, pp. 1668–1674, Dec. 2006.

[99] J. Tersoff, D. E. Jesson, and W. X. Tang, "Running droplets of gallium from evaporation of gallium arsenide.," *Science*, vol. 324, pp. 236–8, 2009.

[100] S. C. Lee and S. R. J. Brueck, "Equilibrium crystal shape of GaAs in nanoscale patterned growth," *Journal of Applied Physics*, vol. 96, no. 2, p. 1214, 2004.

[101] P. Regoliosi, M. Guehl, G. Scarpa, P. Lugli, L. Persano, P. Del Carro, A. Camposeo, R. Cingolani, D. Pisignano, S. Bietti, E. Grilli, and M. Guzzi, "Thermal tunability of monolithic polymer microcavities," *Applied Physics Letters*, vol. 92, no. 25, p. 253310, 2008.

[102] S. Bietti, C. Somaschini, M. Abbarchi, N. Koguchi, S. Sanguinetti, E. Poliani, M. Bonfanti, M. Gurioli, A. Vinattieri, T. Kuroda, T. Mano, and S. Sakoda, "Quantum dots to double concentric quantum ring structures transition," *Physica Status Solidi (C)*, vol. 6, pp. 928–931, Apr. 2009.

[103] S. Bietti, S. Sanguinetti, C. Somaschini, N. Koguchi, G. Isella, D. Chrastina, and A. Fedorov, "Fabrication of GaAs quantum dots by droplet epitaxy on Si/Ge virtual substrate," *IOP Conference Series: Materials Science and Engineering*, vol. 6, p. 012009, Nov. 2009.

[104] S. Bietti, C. Somaschini, S. Sanguinetti, N. Koguchi, G. Isella, and D. Chrastina, “Fabrication of high efficiency III-V quantum nanostructures at low thermal budget on Si,” *Applied Physics Letters*, vol. 95, no. 24, p. 241102, 2009.

[105] C. Somaschini, S. Bietti, S. Sanguinetti, N. Koguchi, A. Fedorov, M. Abbarchi, and M. Gurioli, “Fabrication of GaAs concentric multiple quantum rings by droplet epitaxy,” *IOP Conference Series: Materials Science and Engineering*, vol. 6, p. 012008, Nov. 2009.

[106] S. Bietti, C. Somaschini, S. Sanguinetti, N. Koguchi, G. Isella, D. Chrastina, and A. Fedorov, “Low Thermal Budget Fabrication of III-V Quantum Nanostructures on Si Substrates,” *Journal of Physics: Conference Series*, vol. 245, p. 012078, Sept. 2010.

[107] C. Somaschini, S. Bietti, S. Sanguinetti, N. Koguchi, and A. Fedorov, “Control of the lateral growth morphology in GaAs Droplet Epitaxy,” *Journal of Physics: Conference Series*, vol. 245, p. 012082, Sept. 2010.

[108] S. Bietti, C. Somaschini, N. Koguchi, C. Frigeri, and S. Sanguinetti, “Self-Assembled Local Artificial Substrates of GaAs on Si Substrate,” *Nanoscale Research Letters*, pp. 9–11, 2010.

[109] S. Bietti, C. Somaschini, E. Sarti, N. Koguchi, S. Sanguinetti, G. Isella, D. Chrastina, and A. Fedorov, “Photoluminescence Study of Low Thermal Budget III-V Nanostructures on Silicon by Droplet Epitaxy,” *Nanoscale Research Letters*, vol. 5, pp. 1650–1653, 2010.

[110] C. Somaschini, S. Bietti, A. Fedorov, N. Koguchi, and S. Sanguinetti, “Growth Interruption Effect on the Fabrication of GaAs Concentric Multiple Rings by Droplet Epitaxy,” *Nanoscale Research Letters*, pp. 5–8, Aug. 2010.

[111] C. Somaschini, S. Bietti, A. Fedorov, N. Koguchi, and S. Sanguinetti, “Concentric Multiple Rings by Droplet Epitaxy: Fabrication and Study of the Morphological Anisotropy,” *Nanoscale Research Letters*, pp. 9–11, Aug. 2010.

[112] C. Somaschini, S. Bietti, N. Koguchi, F. Montalenti, C. Frigeri, and S. Sanguinetti, “Self-assembled GaAs islands on Si by droplet epitaxy,” *Applied Physics Letters*, vol. 97, no. 5, p. 053101, 2010.